Physics of surface vibrational resonances: Pillared phononic crystals, metamaterials, and metasurfaces

Yabin Jin, Yan Pennec, Bernard Bonello, Hossein Honarvar, L. Dobrzynski, Bahram Djafari-Rouhani, Mahmoud I Hussein

Physics of Surface Resonances: Pillared Phononic Crystals, Metamaterials, and Metasurfaces

Yabin Jin[1,*], Yan Pennec[2], Bernard Bonello[3], Hossein Honarvar[4,5], Leonard Dobrzynski[2], Bahram Djafari-Rouhani[2], Mahmoud I. Hussein[4,5,**],

[1]*School of Aerospace Engineering and Applied Mechanics, Tongji University, 200092 Shanghai, China*

[2]*Institut d'Electronique, de Microélectronique et de Nanotechnologie (IEMN), UMR CNRS 8520, Université de Lille, 59650 Villeneuve d'Ascq, France*

[3]*UPMC Univ Paris 06, UMR CNRS 7588, INSP, 75005, Paris, France*

[4]*Ann and H.J. Smead Department of Aerospace Engineering Sciences, University of Colorado Boulder, Colorado 80309, USA*

[5]*Department of Physics, University of Colorado Boulder, Colorado 80302, USA*

**Corresponding author: Y. Jin (083623jinyabin@tongji.edu.cn)*

***Corresponding author: M. I. Hussein (mih@colorado.edu)*

Abstract

The introduction of engineered resonance phenomena on surfaces has opened a new frontier in surface science and technology. Pillared phononic crystals, metamaterials, and metasurfaces are an emerging class of artificial structured materials, featuring surfaces, that consist of pillars–or branching substructures–standing on a substrate or a plate. A pillared phononic crystal exhibits Bragg band gaps while a pillared metamaterial may feature both Bragg gaps and local-resonance hybridization gaps. These two band-gap phenomena, along with other unique wave dispersion characteristics, have been exploited for a variety of applications spanning a range of length scales and covering multipe disciplines in applied physics and engineering. The placement of pillars on a semi-infinite surface has similarly provided new avenues for the control and manipulation of wave propagation, including Rayleigh and Love waves along the surface of substrates, as well as Lamb waves in plates–for frequencies ranging from Hz to several GHz. Even a finite placement of pillars along specific directions on a surface has been shown to offer unique functionality, such as steering a wavefront in the subwavelength regime. At the nanoscale, pillared membranes have been investigated and it was shown that atomic-scale resonances–stemming from the nanopillars–alter the fundamental nature of conductive thermal transport by reducing the group velocities and generating mode localization across the entire spectrum well into the THz regime. In this article, we first overview the history and development of pillared materials, then provide a detailed synopsis of a selection of key research topics that involve the utilization of pillars in different contexts. The following sections present a review of different configurations, properties, and

characteristics, namely: (i) fundamental vibrational and propagation properties of pillared plates; (ii) metamaterial phenomena in pillared plates including the opening of low and wide hybridization band gaps as well as super-resolution focusing; (iii) pillared metasurfaces and their wave steering functions; (iv) topologically protected phononic edge states in pillared plates; and (v) nanophononic metamaterials in the form of pillared membranes exhibiting exceptionally low in-plane thermal conductivity. Finally, we conclude by providing a short summary on the salient properties of pillared materials and structures and outlining some perspectives on the state of the field and its promise for further future development.

Keywords: surface resonance; pillared material; phononic crystal plate; acoustic/elastic metamaterial, acoustic/elastic metasurface; nanophononic metamaterial

Chapter 1 General introduction

Light and sound are two key information carriers that provide platforms for vast opportunities for technological advancement [1-6]. In recent decades, we witnessed a revolution in our ability to manipulate and control photons and phonons through the design of functional material systems with

properties that extend well beyond what is found in nature and in conventional materials. Inspired by an analogy with the quantum mechanical band theory of solids, in which electronic wave fields interact with a periodically arranged atomic lattice to form energy bands separated by band gaps [7], Yablonovitch [8] and Sajeev [9] proposed the concept of a *photonic crystal* in 1987. In a photonic crystal, the atoms are replaced by macroscopic media with differing dielectric constants and the periodic potential is replaced by a periodic dielectric function. The outcome was a new type of engineered material that exhibits photonic band gaps in which light is prevented from propagating in certain directions at certain frequencies. The notion of phononic crystals then followed by further analogy. In contrast to electromagnetic waves which only permit transverse polarization, elastic waves admit coupled longitudinal and transverse polarizations−a trait that makes the design for band gaps even more challenging. The search for material structures with elastic band gaps and the concept of *phononic crystals* were independently proposed by Sigalas and Economou [10, 11] and by Kushwaha et al. [12]. The material systems investigated exhibit partial and full band gaps for propagation of acoustic/elastic waves in periodic composites constituted by an array of inclusions placed in a background host medium. It is worth mentioning that the constituting media, either in the inclusions or in the background, may be a solid or a fluid (liquid or gas). While "fluid materials" support only longitudinal modes, solid materials admit both longitudinal and shear waves.

The field has experienced a burst of interest following these discoveries and increasingly acquired a multidisciplinary character involving both bulk and surface materials with features engineering at the nanoscale, microscale, and/or macroscale. Now generally referred to as phononics, this emerging field encompasses a wide range of interconnected disciplines including condensed matter physics, materials science, acoustics, mechanical engineering, electrical engineering, among others . In more general terms, a phononic crystal is an artificial material consisting of a periodic inhomogeneous elastic medium that can manipulate the propagation of acoustic waves in fluids (or fluid-like solids) and/or elastic waves in solids. The propagation of acoustic/elastic waves in a phononic crystal is governed by Bloch's (or Floquet's) theorem (simply expressed as having the eigenstates of the Hamiltonian satisfy $\psi(\vec{r}+\vec{R}) = e^{i\vec{k}\vec{R}}\psi(\vec{r})$, where $\vec{r}$, $\vec{R}$, and $\vec{k}$ denote the position vector, reciprocal lattice vector, and wave vector, respectively). This fundamental theorem provides the foundation to computing the band structure (dispersion relationship) over the Brillouin zone (the primitive cell in reciprocal space) of the periodic medium of interest [13]. Similar to photonic crystals, band gaps appearing in a phononic band structure represent frequency ranges where acoustic/elastic waves are prohibited from propagation. In periodic materials, the origin of a band gap is the well-known mechanism of *Bragg scattering*, which is based on destructive interferences of waves scattered by inclusions, holes, internal interfaces, etc., orderly arranged in a spatially repeated fashion. The underlying condition for this linear form of scattering is that the path difference between the interfering waves must be equal to an integer multiple of their wavelength [14]. As the path difference

depends on the lattice constant of a crystal, when the wavelength is comparable to the lattice constant, the Bragg scattering mechanism occurs.

In an alternate and fundamentally different mechanism, band gaps may form from the avoided crossing of two bands of the same symmetry, where at least one of the two bands originate from a localized resonance mode of an individual particle, inclusion, or substructure. The emerging band gap is termed a hybridization gap [15]. This concept sparked the field of *acoustic/elastic metamaterials*, and led to the proposition of "locally resonant sonic materials" by Sheng and his colleagues [16]. The first embodiment of an acoustic metamaterial took the form of a matrix of silicone-coated metallic spheres embedded in epoxy. Different from the Bragg scattering mechanism, the relevant wavelength corresponding to the local resonance may be orders of magnitude larger than the size of unit cell or the size the resonating element; this in turn has opened the door for *low-frequency band gaps*. This in particular opened up the opportunity of achieving sound isolation in the kHz range, while keeping the size of the unit cell reasonably small (on the order of a few centimeters). Indeed, with the acoustic velocities of common materials, the unit cell needs to be on the order of meters to pull a Bragg gap into the sonic regime. Some of the above concepts may easily be understood within the framework of very simple academic models in one dimension as briefly described in Chapter 2A. The reader is referred to a collection of recent books [2-4, 6] and review articles [17, 18] on this continuously emerging field of research.

The objective of this review paper is to present properties and functionalities of a unique type of phononic material proposed just over a decade ago consisting of an array of pillars on a plate or on a substrate [19, 20]. This configuration is characteristically a two-dimensional (2D) material, i.e., has a Brillouin zone that can be fully defined in two dimensions, with the branching pillars acting as the local resonators. Therefore, similar to Sheng's bulk metamaterial, the mechanism of local resonance and hybridization gaps exists in a pillared 2D medium or surface. Furthermore, Bragg band gaps may form as well due to the spatial periodicity of the placement of the pillars (see the simple models covered in Chapter 2A). Because of this dual aspect, material systems belonging to this class effectively behave both as phononic crystal and metamaterial. Furthermore, when the pillars lie on a surface, the outcome is effectively rendered an elastic metasurface. For example, a line of gradient pillars on a surface may be regarded as an elastic metasurface with the characteristic pillar diameter falling well within the subwavelength regime. Since their proposition, a sizable body of work has been devoted to the investigation of these materials/surfaces/structures and their functionalities as is described throughout this review. A general summary is first given in this introduction.

Pillared metamaterials with low-frequency band gaps were first studied by Pennec *et al.* [19] and Wu *et al.* [20] in 2008. In both studies, periodic plates with a single pillar in the unit cell were considered. It was reported that if one suitably chooses the geometric parameters of the pillar's

diameter and height, and the thickness of the plate on which it is supported, a low-frequency band gap may appear below the first Bragg band gap in the dispersion curves–this subwavelength band gap originates from an avoided crossing between a pillar's local resonance mode and a dispersion branch of the plate. Low-frequency band gaps in the kHz [20-23] and MHz [24] frequency ranges were subsequently experimentally validated. Since a low-frequency band gap depends on both the pillar's mode and the plate's mode involved in the coupling, a range of possibilities are available for modifying the geometric parameters or material composition to tune the properties of the band gap, especially its width. It is found that designing the connection between the pillars and the plate such that it consists of a relatively narrow neck [25, 26], or a conic angle [27, 28], or a soft material such as rubber [29-34], allows us to shift the low-frequency gap downwards. These changes are effectivity analogous to reducing the "stiffness" in a branching mass-spring system, which may be used as an idealized model for studying the mechanism of local resonance band-gap formation [35-37]. The shape of the deposited resonators (cylindrical pillar, square rod [7, 38-41], sphere [42], spiral [43] or Gaussian surface [44]) and the lattice symmetry of the periodic arrangement (triangular [45-47], square [45-49], hexagonal [48], honeycomb [45, 49], hybrid [50, 51], or random [52, 53]) have direct impact on the properties of the engineered local resonance band gap, such as its width and position in the frequency domain. Having pillars on both sides of a plate provide an additional avenue for enriching the design space [54-58]. Given that local resonance behavior does not depend on periodicity, a hybridization band gap may appear in aperiodic or disordered systems [23, 52, 53]. Localized modes corresponding to low-frequency band gaps may be further synthesized by introducing hollow parts in the pillars [59-61]. Moreover, the band-gap width may be enhanced with multi concentric hollow pillars [62, 63]. Filling the hollow pillars with a liquid enables the generation of solid-liquid coupling modes which can be actively tuned by controlling the filling height [60, 64] and utilized towards the realization of tunable phononic circuits [65]. In addition to altering the design of the pillar(s), removal of material from the plate portion also provides an opportunity for performance enhancement and further broadening of the band-gap width, giving rise to the notion of a *trampoline metamaterial* [66] where the base acts as springboard with reduced stiffness. The trampoline concept was pursued in a variety of settings and configurations [41, 43, 50, 61, 67-70]. Moreover, active tuning of band-gap properties is possible by an applied external magnetostatic field [40] or by shunted piezoelectric transducers [71-76]. Similar to pillars on a plate, pillars on a substrate were also theoretically and experimentally investigated with a view on their local resonance band gaps [24, 77-82]. It is further reported that the number of elements in a phononic crystal can be reduced by designing a pillar-in-hole instead of a pillar-on-surface as its band-gap attenuation is about one order-of-magnitude larger [83]. The coupling of photonics and phononics has added yet another avenue of applications. For example, a periodic array of pillars deposited on a thin plate may be designed to exhibit dual phononic and photonic band gaps holding promise for the simultaneous confinement and tailoring of sound and light waves [45, 84, 85].

In the characterization of acoustic/elastic metamaterials, generally a monopole resonance relates to negative effective compressibility and a dipole resonance relates to negative effective mass density when evaluated within the range of a hybridization band gap. However, a pillared metamaterial element tends to bring more difficulties in analyzing negative effective compressibility or mass density than conventional 1D, 2D, or 3D metamaterial elements. This is due to the lack of a precise effective medium theory describing the complex pillar's vibrations in free space associated with its base. Nevertheless, a pillared metamaterial may be considered as a homogeneous plate with anisotropy in the effective mass density matrix [86] or effective wave number [87], exhibiting negativity in the effective density [86-88], effective Young's modulus [87] ,or effective stiffness [89]. Indeed, the monopolar or dipolar resonant frequencies of a pillar may be easily tuned by a proper choice of the height and/or diameter [90], resulting in easily being able to probe the conditions for either the effective mass density negativity or the effective modulus negativity. The effect of pillar resonances in the context of scattering and transmission of a single or a line of resonant pillars subject to an incident surface wave is also a problem of interest. In such a configuration, the pillars emit waves that can interact with an incident wave, allowing for a phase/amplitude shift in the transmission. Fano resonance can be induced by introducing two dissimilar pillars in one unit cell along one row of pillars [91]. A new geometry proposed recently consists of replacing a homogeneous pillar by a multilayer material, a kind of one-dimensional phononic crystal [92], allowing confinement of modes inside a cavity or at the interface between the pillar and the substrate. In such a geometry, these highly confined modes of the pillars result in very sharp Fano resonaces–or the acoustic analog of electromagnetically induced transparency–when they interact with an incident surface Rayleigh or Love mode [93, 94]. More generally, owing to the recent growing interest in the topic of metasurfaces, where a very thin (sub-wavelength) structure containing phase array elements can manipulate the propagation of sound (or light) and give rise to various new effects such as anomalous refraction and reflection and focusing or imaging phenomena, a line of resonant pillars on a plate or a substrate provides a new tool for exhibiting similar features by manipulating the propagation of plate and surface waves.

The pillared medium architecture may also be realized for a 1D system consisting of a slender tube with stubs grafted on a single side or both sides. The first study on acoustic band gaps with such structures was published by Kushwaha *et al.* [95] in 1998. They found that a periodic pattern of large stop bands is obtained with the lowest gap extending possibly down to zero frequency. Large magnonic [96] and photonic [97] band gaps were subsequently found with the same structure. The grafted stubs can behave as resonators to induce Fano resonances when the resonance is situated between two zeros of transmission [98], and can even exhibit the acoustic analog of electromagnetically induced transparency [91, 99] and trapped mode phenomenon [100]. If the stubstructures are placed between two slender tubes, selected transfer of a single propagating state

from one tube to the other is possible, with all other neighboring states remaining unaffected. This result has been applied to filtering or multiplexing [101]. The characteristics of the band structure and wave transmission when the stubs are grafted to the tube in a single side [102-104], double symmetric sides [105-108], and asymmetric sides [109] were theoretically and experimentally investigated. Theoretical investigations on the connection between the transmission properties of continuous stubbed models and macroscale thermal transport have been proposed [110, 111].

In the realm of applications, pillared phononic crystals, metamaterials, and metasurfaces make it possible to control and manipulate acoustic and/or elastic waves with many potential benefits in modern information processing and communication, among other avenues. To follow is a synopsis of six possibilities: (I) *Negative refraction and superlens*. With a proper choice of the pillar's geometry in pillared periodic media, a negative refractive effect can be achieved (i) when a dispersion branch reveals opposite signs between the group velocity and the phase velocity yielding a negative effective refractive index [112, 113]; and (ii) when the group velocity is never in the opposite direction to the phase velocity but the convexity of the iso-frequency contours of a branch leads to negative refraction with positive effective index [114]. This latter scenario demonstrates sub-wavelength high resolution in superlensing applications. A far-field super-resolution experiment has been demonstrated for a metamaterial made out of long pillars attached to a plate with the One-Channel Inverse Filter [115]. (II) *Waveguides, defect states, and filtering applications*. If the travelling frequencies are located within a Bragg or a hybridization band gap of the background pillared structures, waveguides may be constructed consisting of different sizes of pillars or line- or curved-shape defects [59, 78, 81, 116-127]. Such design interventions can produce localized modes inside the Bragg or hybridization band gaps of the phononic crystal, hence allowing the propagation of confined modes in the waveguide. (III) *Vibration attenuation*. The existence of Bragg and local resonant band gaps in pillared phononic crystals and metamaterials play important roles in designing sonic [29, 88, 128-130] and elastic [20-24, 131] wave insulators. As mentioned earlier, an extra wide band gap combining both Bragg and local-resonant band gaps were proposed by tailoring the plate connection between neighboring pillars [50, 61, 66-70]; these systems serve as excellent candidates for vibration attenuation in solids. If the pillar resonators are in the meter scale, a pillared-metamaterial may in principle prevent Rayleigh modes in seismic wave propagation [132, 133] or even shape seismic wave flow [134]. (IV) *Graded Resonant Devices.* Combining a resonant pillar with gradient index lens [135-140], a focusing point can be achieved beyond the diffraction limit [141]. Gradually varying the height of the pillars, resonant gradient index metalenses for flexural waves [142] and metasurfaces for converting surface Rayleigh waves to bulk shear waves [143] were proposed. The guiding of elastic waves with a graded radius of pillars in a phononic crystal plate has also been investigated [144]. (V) *Phononic Graphene*. Pillars placed in a hexagonal lattice on a plate can be regarded as spring-loaded resonators, providing a promising platform for investigation of the elastic analogue of graphene [145], as well as the quantum

valley Hall effect [146] and the quantum spin Hall effect [147] (in analogy to corresponding systems in quantum mechanics and condensed matter physics) with novel phonon transport behavior such as pseudo diffusion [148], the Zitterbewegung effect [148], the zigzag edge state [145], and topologically protected edge modes [149-151]. (VI) *Pillared Metasurfaces*. A metasurface can be considered as a slice of a bulk metamaterial with a subwavelength thickness; such a surface is able to steer wavefronts at will by designing an abrupt phase profile on the surface [152-158]. A growing interest is devoted to these metasurfaces due to their broad functionalities such as anomalous reflectiion and refraction, or focusing and imaging phenomena. Following the generalized Snell's law [159], a line of pillars can be designed to manipulate various wavefront functionalities from the discrete phase response of an array of resonant pillars [90]. This is quite attractive in view of the potential practical applications to controlling the propagation of Lamb waves on a plate or surface acoustic waves on a substrate. Such pillared metasurfaces also demonstrate diverse resonant phenomena [91, 99]; for example, the acoustic analogue of a bound state in a continuum, electromagnetically induced transparency, Autler-Townes splitting, and others [160].

Finally, the pillared plate configuration has also found application in smaller scales. In the Gigahertz regime, pillared configurations have been investigated giving rise to "hypersonic phononic crystal and metamaterials" [161-165] where band gaps have been observed by Brillouin light scattering spectroscopy. At the far extreme of scales, reaching down to a few nanometers, the concept of a *nanophononic metamaterial* (NPM) was proposed for the reduction of the lattice thermal conductivity [166-171]. An NPM in the form of a suspended silicon membrane with a periodic array of nanopillars was proposed as a particularly advantageous configuration for not only thermal conductivity reduction, but also thermoelectric energy conversion. In this configuration, the nanopillars generate local resonances that, similar to macroscopic systems, couple and hybridize with the underlying dispersion curves. However, here the interest is in creating a very large number of local resonances (possibly on the order of millions or more) spanning the entire spectrum of thermal transport−which may reach up to tens of THz. A recent theoretical study using lattice dynamics calculations and molecular dynamics simulations predicted two orders of magnitude reduction in the in-plane thermal conductivity of a silicon membrane stemming from the introduction of nanopillars with a shape, size, and spacing carefully selected with respect to the base membrane thickness [170, 171]. In particular, it was shown that increasing the height and width of the nanopillars (up to a limit dictated by the phonon mean free path distribution) increases the level of thermal conductivity reduction [170, 171]. Other research examined diffuse phonon scattering at the interface between pillars and a substrate [172].

In this article, we provide a review of the authors' original contributions to the study and development of pillared materials−for both macroscale elastic waves and nanoscale thermal transport− as well as the progress that emerged afterwards by the phononics community at large. The paper is

organized into six sections. The current section provides a background and an overview of the state-of-the-art in pillared materials and structures. In the second section, we review vibrational properties of pillared phononic-crystal plates for wave transport and multiphysical interaction. In the third section, we cover pillared metamaterial plates with enhanced low-frequency band gaps and super-resolution focusing. In the fourth section, we review pillared acoustic metasurfaces with anomalous resonant and transmitted properties. The fifth section focuses on topological pillared phononic plates that exhibit topologically protected edge states with immunity to local perturbations. In the sixth and last section, we review the concept of a nanophononic metamaterial, which, as an example, is based on a silicon thin film or membrane with a periodic array of nanopillars erected on one or two of the free surfaces. Finally, we conclude with a summary and an outlook on the future promise of continued research on pillared systems at various length scales.

Chapter 2 Wave propagation properties of pillared plates

A. Basic model

Some of the concepts related to phononic crystals and in particular pillared structures can easily be understood in the frame of very simple and academic models in one dimension. For instance, assume a linear monoatomic chain composed of atoms of mass m connected to each other by a force constant β. By writing the equation of motion for atom n and inserting a propagating wave solution for the displacement, $u_n(t) = Ae^{i(kna-\omega t)}$, the phonon dispersion curve is straightforwardly derived as $m\omega^2 = 2\beta[(1-\cos(ka)]$, where k and ω are respectively the wavenumber and the frequency of the phonon (Fig. 2.1.a). The wavenumber takes a real value as far as the frequency does not exceed $\omega_{\max} = \sqrt{4\beta/m}$. Above this frequency, it becomes complex ($k = k' + ik''$), which means that the vibration will be attenuated and is not permitted to propagate along the chain. Now, if a defect in the form of a light mass $m' < m$ is inserted at the site $n = 0$ of the chain, the equations of motion will admit a solution associated with a localized mode at a frequency above $\omega_{\max}$, with an eigenfunction that decays on both sides far from the defect. This is a simple analogue of a cavity mode inside a phononic crystal. This approach can be extended to the case of a biatomic linear chain consisting of two different alternate masses m and M connected by the same spring of force constant β. The acoustic and optical phonon branches are now separated by a gap at the edge of the Brillouin zone (Fig. 2.1.b). Again, by inserting a defect of mass m' at site 0, the crystal will exhibit a localized mode associated with the defect inside the band gap and the corresponding frequency is presented in the figure as a function of the ratio m'/m.

A new situation is encountered when a side atom of mass m' is attached to the monoatomic linear chain at site $n = 0$, with a force constant β' (Fig. 2.1.c). By eliminating the degree of freedom associated with this additional mass, the equation of motion for atom 0 is written exactly as for as for the linear

chain containing a mass defect at site $n = 0$, but now the latter mass becomes a dynamical mass depending on the frequency such that $M(\omega) = m + \frac{\beta' m'}{\beta' - m'\omega^2}$. At very low frequency, this mass starts at $m + m'$, then increases until it diverges to $+\infty$ at a "resonance" frequency $\omega_0 = \sqrt{\beta'/m'}$, then jumps to $-\infty$ and remains negative until a frequency of $\omega'_0 = \sqrt{\beta'(m+m')/mm'}$ where it vanishes before becoming again positive and going to m at very high frequencies. The most interesting observation is that at the resonance frequency, the dynamical mass behaves like a very heavy mass which will prevent any transmission (assuming that the parameters are chosen in a such a way that ω_0 falls in the range of the propagating waves in the linear chain) and produces a zero in the transmission coefficient (Fig. 2.1.c). Also, the additional mass and the atom at site 0 vibrate in phase just below ω_0 and out of phase just above this frequency. Finally, if a periodical array of side atoms is attached to the linear chain, the zero of transmission widens into a local-resonance hybridization band gap, as sketched in Fig. 2.1.d. Of profound importance is the notion that that the resonance frequency may be chosen to be very low, which opens up the field of effective medium theory for metamaterials as will be discussed in-depth later. An equivalent model to the one discussed above is also presented in Fig. 2.1.d where each atom of the lattice has a resonating internal degree of freedom.

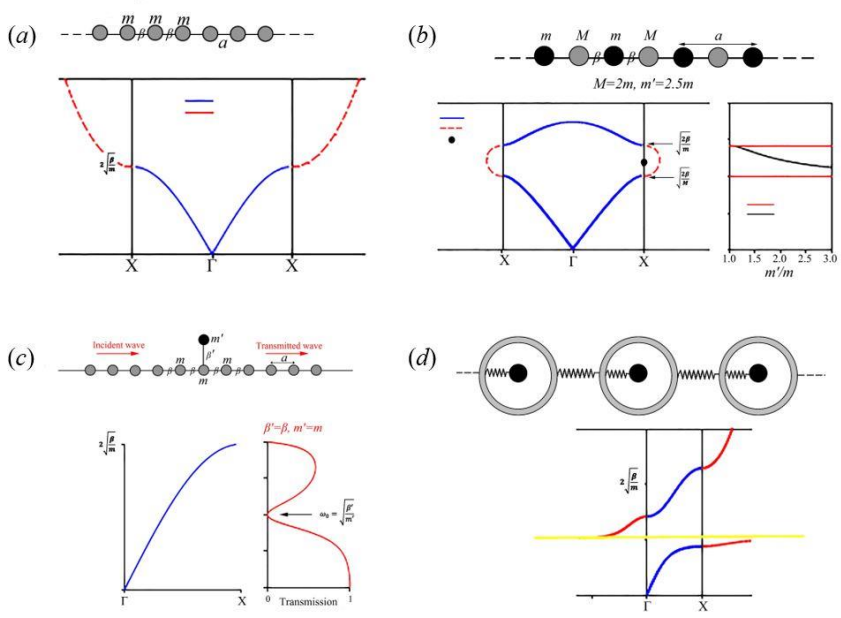

Figure 2.1. Mass-spring models and corresponding dispersions: (a) a linear monoatomic chain made of identical atoms; (b) a biatomic linear chain comprising two different atom types; (c) a side atom is attached to monoatomic linear chain; (d) a periodic array of side atoms is attached to the linear chain to form a locally resonant periodic chain.

B. Dual aspects of phononic crystals and metamaterials

Many efforts have been devoted to the study of absolute band gaps in phononic crystals, particularly for applications such as confinement, waveguiding, and filtering. In this subsection, we review the basic band structure properties of phononic crystal plates which comprise of a periodic arragment of pillars placed on top of a thin homogeneous plate as displayed in Fig. 2.2 forming a square array. Bragg and hybridization band gaps can be simultaneously observed in such phononic plates and as such they may be dually classified as phononic crystals and acoustic metamaterials. The illustrations are given for pillars made of steel on a silicon plate. The elastic constants and mass densities of these materials are found in Ref. [19]. Dispersion curves are calculated along the 2D irreducible Brillouin zone and presented in the form of reduced frequency $\Omega=\omega a/(2\pi v_t)$, where v_t is the transverse bulk velocity of silicon.

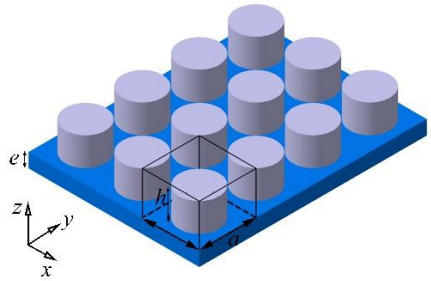

Figure 2.2. Geometry of a phononic crystal plate consisting of periodic pillars deposited on a thin plate. In the present section, the plate's thickness is denoted by *e*, and the height of the pilars by *h*.

The dispersion curves in Fig. 2.3 are calculated for the parameters: pillar's radius r/a=0.42, pillar's height h/a=0.6 and the plate's thickness e/a=0.1. At low frequencies, three lowest bands appear at Γ point (the center of the Brillouin zone)–these are the antisymmetric (A_0), shear-horizontal (SH_0), and symmetric (S_0) Lamb modes. As the frequency increases, the three branches bend in such a way as to give rise to the opening of a narrow hybridization gap (shaded in blue). At this frequency, the wavelength of the S_0 Lamb mode is about 15 times the lattice constant *a*. The simultaneous bending of the acoustic branches and the existence of this band gap are intimately related to the choice of the geometrical parameters as will be discussed below. Besides, with a choice of the parameters within the common range for actual materials and devices, one can also observe the existence of a broad Bragg band gap; see region shaded in red in Fig. 2.3.

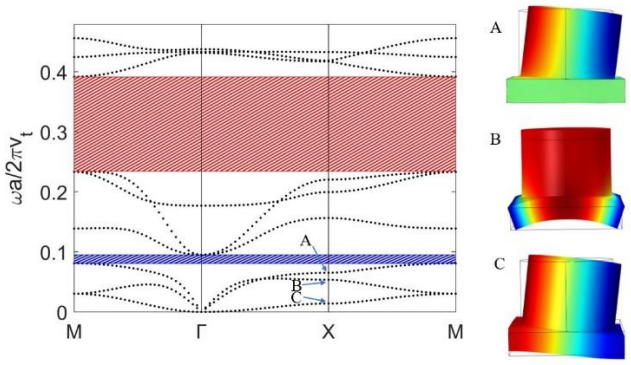

Figure 2.3. Dispersion curves for the following pillared plate: steel pillar's radius r/a=0.42, pillar's height h/a=0.6 and the silicon plate's thickness e/a=0.1. The red and blue dash zones indicate Bragg and local-resonance hybridization band gaps, respectively. Eigenmodes corresponding to the three points A, B and C at X are displayed at the right. This figure is based on results from Ref. [19].

To provide a deeper insight into the origin of the modes leading to the opening of the hybrydization gap, we have calculated the spatial distribution of the eigenmodes at the high symmetry point X of the Brillouin zone and plotted them in Figs. 2.3. The modes *A* and *C* are clearly associated with a bending of the pillar together with, respectively, a weak and a strong bending of the plate. The vibration of mode *B* corresponds to a compressional mode, in the *z* direction, correlated with a strong vertical displacement of the plate. More specifically, the motion of branches *A* and *B* are strongly correlated with the opening of the absolute low-frequency hybridization band gap.

In Fig. 2.4, we have fixed the values of the radius of the pillar r/a=0.42 and the thickness of the plate e/a = 0.2 while changing the height of the pillar as h/a = 0.6, 1.2 and 1.8. For h/a = 0.6, we note the existence of the low-frequency hybridization and the high-frequency Bragg band gaps discussed previously. The lowest one closes for h/a = 1.2 and the central frequency of the higher one decreases, although appears to change its type. This is observed in the middle panel of Fig. 2.4 which also shows that the band structure there exhibits a new band gap, occurring at the reduced frequency 0.42. When increasing h/a to 1.8, the central frequencies of the first two band gaps move downwards together with the dispersion curves, whereas a new additional absolute band gap appears again at higher frequencies. It is interesting to remark that, for some of these band gaps, their opening results from the crossing of the normal acoustic branches with almost flat bands, which is the key mechanism that characterizes locally resonant materials.

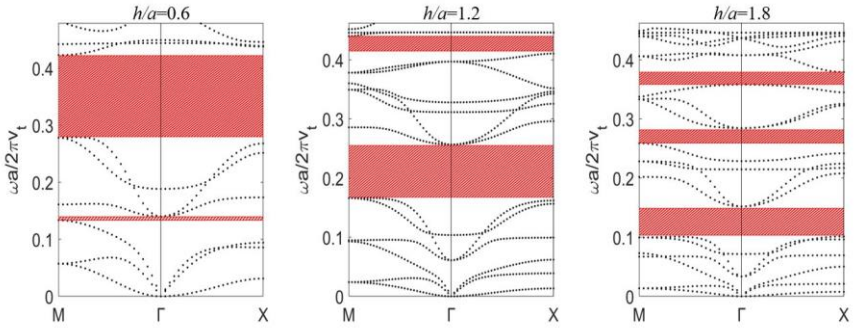

Fig. 2.4. Evolution of the band structure for different values of the height of the pillar: (left) h/a = 0.6, (middle) h/a = 1.2 and (right) h/a = 1.8. The other geometrical parameters are e/a = 0.2 and r/a=0.42. This figure is based on results from Ref. [19].

We have also studied the evolution of the band gaps with the thickness of the plate e, keeping constant h/a = 1.8 mm and r/a=0.42 (right panel of Fig.2.4). This is useful to demonstrating the evolution of the branches when transitioning from a thin plate to a thick plate mimicking a substrate. When increasing e/a from 0.1 to 1.0 (Fig. 2.5(a)), we observe a slow variation of the central frequency of the gaps. In addition, most of the gaps close at e/a = 1, because many dispersion branches move downwards, except for the hybridization one at low frequency which appears more robust and closes for e/a > 1. In parallel, when increasing the thickness of the plate from 0.3a to a and higher, the Lamb waves gradually tend to become confined at the two opposite surfaces of the thick plate, rendering them as surface acoustic waves (SAW) or Rayleigh waves on each of the two sides. In the illustration of the dispersion curves, the separation between SAW and bulk waves can be achieved by drawing a sound line which corresponds to the lower phase velocity in the bulk substrate, silicon in our example. Fig. 2.5(b) represents the dispersion curves obtained for a thickness e/a = 1 in which the sound cone of silicon is represented by the grey shaded area. It means that the modes below the sound cone can only propagate at the surface. In contrast, inside the cone, the modes can be radiative and coupled to the bulk silicon modes. From this analysis, we extend the notion of band gaps to surface acoustic waves by highlighting among the corresponding branches the frequency areas that are free of modes. Indeed, in Fig. 2.5(b), the blue shaded areas correspond to partial band gaps in one direction ΓX or ΓM of the Brillouin zone while the red area corresponds to an absolute band gap for surface acoustic waves.

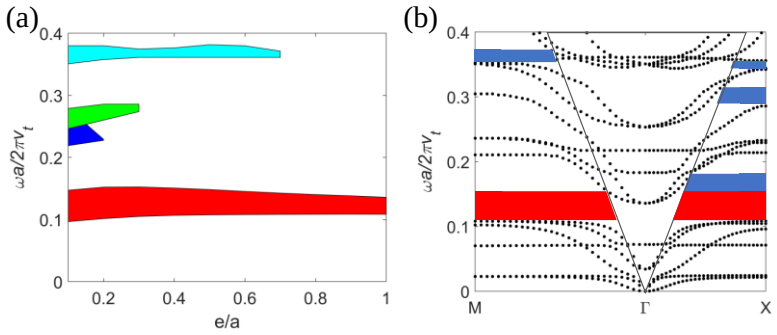

Figure 2.5. (a) Evolution of the band gaps in the right panel of Fig. 2.4 as a function of the thickness of the plate, keeping constant the other geometrical parameters (h/a = 1.8 and r/a=0.42). (b) Representation of the dispersion curves for a thick plate (e/a = 1). The triangle grey area corresponds to the sound cone of the silicon plate. The blue (red) area shows the existence of partial (absolute) band gap for surface acoustic waves. This figure is based on the results from Ref. [19].

Finally, we have also investigated the robustness and persistence of the low frequency hybridization gap upon different combinations of materials constituting the pillars and the plate among a set of five materials displaying very different acoustic properties: tungsten, steel, silicon, aluminum, and epoxy. In the left panel of Fig. 2.6, we show the limits of the low-frequency gap by changing the material of the plate when the pillars are made of steel. Similarly, the right panel of Fig.2.6 displays the gap limits

for various materials in the pillars for a plate made of silicon. One can notice the persistence of the hybridization gap even if the constituting materials are identical. This supports the understanding that the origin of the gap is related to the geometrical rather than the constituent material parameters of the extended structure. On the other hand, the central frequency of the gap is very dependent upon the choice of the materials and happens at lower frequencies when we combine a high-density material, steel, in the cylinders with a low-density material, epoxy, in the plate. It is worthwhile to notice that with this choice one can obtain a gap in the audible frequency range, around 2 kHz, for a period of a = 20 mm and the other parameters being scaled accordingly. Such solid systems could practically be used as a vibrationless environment for high-precision mechanical systems.

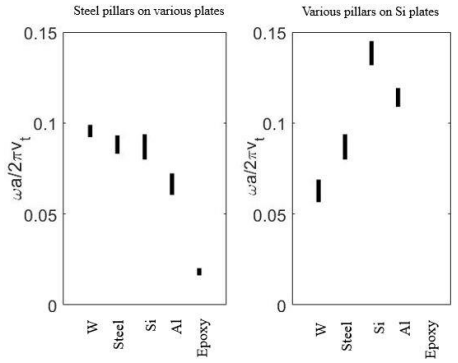

Figure 2.6. Evolution of the lowest-frequency gap limits for different combinations of constituting materials. (left) Steel pillars on a plate of different materials. (right) Various dots on a silicon plate. The geometrical parameters are e/a = 0.1, h/a = 0.6, and r/a= 0.42. For an epoxy pillar on a Si plate, the lowest frequency gap disappears. This figure is based on results from Ref. [19].

C. Phononic transmission and waveguiding

From the calculation of both transmission coefficients and dispersion relations of pillared phononic crystal plates, we illustrate here the phenomenon of wave guiding when removing one row of pillars in a perfect crystal. The flexibility of tuning the acoustic/elastic properties, especially for waveguides, makes it particularly suitable for diverse applications from transducer technology to filtering and guiding of acoustic/elastic waves.

Figure 2.7 shows the transmission coefficient for pillared phononic crystal plate made of a square array of steel pillars deposited on a thin silicon plate. The band structure is reported in the middle panel in the reduced frequency range (0, 0.45) along the high symmetry axes ΓX and ΓM of the first Brillouin zone. The choice of the geometrical parameters ensures the existence of two absolute band gaps, respectively at low and high frequencies (relative to the frequency range displayed). We also show the computed transmission spectra in the directions ΓX and ΓM of the Brillouin zone, displayed on each side of the central band diagram. The transmission spectra are given both for a S_0 or an A_0 incident Lamb wave.

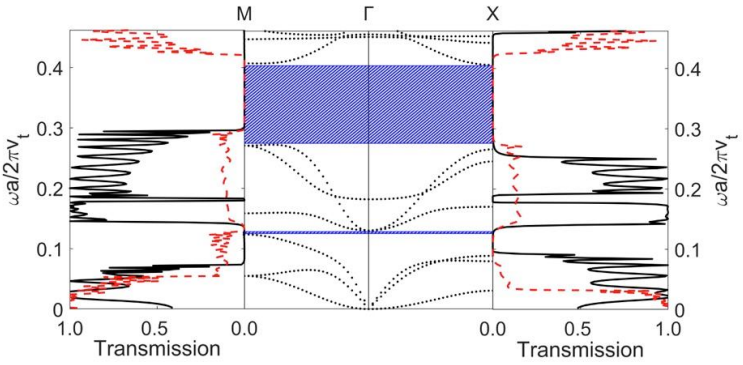

Figure 2.7. (left and right) Transmission calculation (black solid line for S_0 Lamb wave excitation and red dashed line for A_0 Lamb wave excitation) through a phononic crystal plate consisting of a square lattice of steel pillars deposited on a silicon plate. The geometrical parameters are h/a = 0.6 and e/a = 0.2. (Middle) dispersion curves calculated along the high symmetry axis ΓX and ΓM of the Brillouin zone. The blue areas correspond to the position of the low and high absolute band gaps. This figure is based on results from Ref. [116].

We now investigate the possibility of guiding wave modes in both the low and high frequency gaps inside an extended linear defect designed by removing one line of pillars as seen in Fig.2.8(a). The length of the waveguide is assumed to be 7 periods of the unit cell. In the super-cell calculations, the neighboring waveguides are separated from each other by 4 lines of full pillars in order to minimize their coupling and hence the leakage effect. Fig. 2.8(b) presents the transmission spectra where the incident wave is a S_0 (upper) or an A_0 Lamb wave (lower). For comparison, we also provide the transmission through the perfect (red dashed lines) phononic crystal. The shaded blue areas represent the positions of the two band gaps from the corresponding dispersion curves. One can see the occurrence of a transmitted signal in the higher band gap for both the S_0 and A_0 Lamb wave excitations. On the contrary, the transmission in the low frequency gap essentially occurs for S_0 Lamb wave excitation while it remains very low for A_0. To highlight the wave guiding properties through the gaps, we show in Fig. 2.8(c) the propagation of two monochromatic waves, corresponding respectively to a S_0 Lamb mode at the reduced frequency of 0.393 and to a A_0 mode at frequency 0.108.

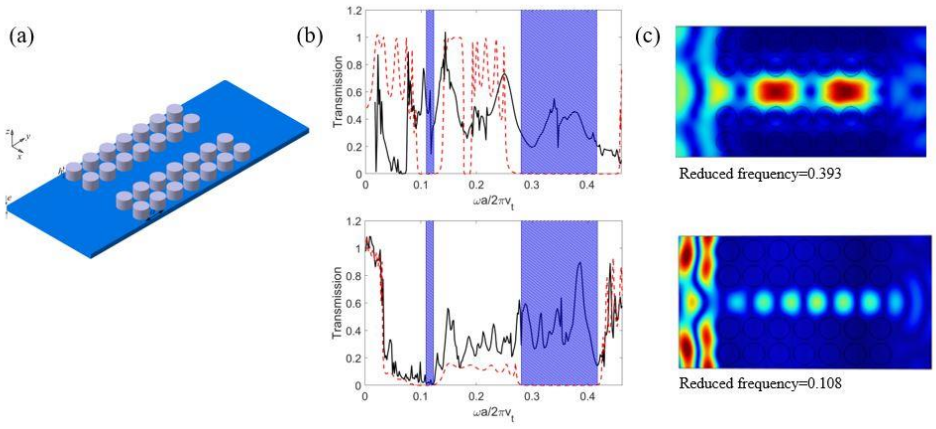

Figure 2.8. (a) Schematic view of a line-defect waveguide; (b) S_0 Lamb wave excitation (upper) and A_0 Lamb wave excitation (lower) transmission through the waveguide (black solid lines) and through the perfect (red dashed

lines) phononic crystal. (c) Example of guided mode for S_0 Lamb wave (top right) and A_0 Lamb wave (bottom right) at the reduced frequencies of 0.393 and 0.108, respectively. A portion of this figure is based on results from Ref. [116].

D. Example configuration: Hollow pillars and whispering-gallery modes

1. Whispering-gallery modes of hollow pillars

The study of whispering-gallery modes (WGMs) dates back to the work of Rayleigh in 1910 on the propagation of sound around a gallery in St. Paul's Cathedral [173]. High quality factor WGM resonators may be applied to sensing, filters, modulators, among other applictions in optics and photonics, area that have been receiving increasing attention in recent years. In this subsection, hollow pillars are employed instead of full-solid pillars in phononic crystal plates. Indeed, the hollow structure can introduce WGMs with a high quality factor owing to their confinement and this parameter can even be significantly enhanced by insertion of an additional full pillar at the bottom of the hollow pillar to isolate the WGM from the plate. We consider a hollow pillared phononic crystal plate with a square lattice array and the entire structure made of silicon. The example of a hollow pillar unit cell is displayed in Fig. 2.9d.

We first present the band structure of a full pillared phononic crystal plate along the direction ΓX of the reduced Brillouin zone as shown in Fig. 2.9a. The geometrical parameters are: height of pillar h/a=0.45, radius of pillar r/a=0.4, and plate's thickness e/a=0.1, where a is the lattice constant. The dispersion curves are plotted in the form of the reduced frequency $\Omega=\omega a/(2\pi v_t)$, where v_t is the transverse bulk velocity of silicon. As explained in the previous subsections, such pillar structure exhibits both a Bragg band gap and a low frequency hybridization band gap simultaneously and therefore behaves as a phononic crystal or as an elastic metamaterial depending on the context. Then, the full pillar is replaced by a hollow pillar, whose geometric parameters are the same except for the inner radius which is chosen as r_i/a=0.145. The dispersion curves of the hollow pillar unit cell is presented in Fig. 2.9b, where two new bands in red and pink appear in the Bragg band gap, meanwhile all the rest black bands remain almost unchanged. In Fig. 2.9c, the corresponding transmission curve is calculated with the fundamental antisymmetric (A_0) Lamb mode excitation and the propagation direction being along the x coordinate. One observes that only the red band can generate a transmission peak p, while the pink band behaves as a *deaf mode*. This is attributed to the symmetry of the eigenmodes of the two bands, as illustrated by the real part of the z-displacement component of the two bands at the Γ point in Fig. 2.9d. Both the red and pink bands are characterized by the quadrupolar whispering-gallery mode (WGM4). The displacement field of WGM4 (red band) is symmetric with respect to the x-z plane and is therefore compatible with the symmetry of the incident A_0 Lamb wave, so that WGM4 can be excited. However, it is asymmetric for WGM4-deaf (pink band), resulting in a mode that cannot be observed in transmission. It should be mentioned that the quality factor of WGM4 can be significantly enhanced by inserting an additional full pillar part between the hollow pillar and the plate.

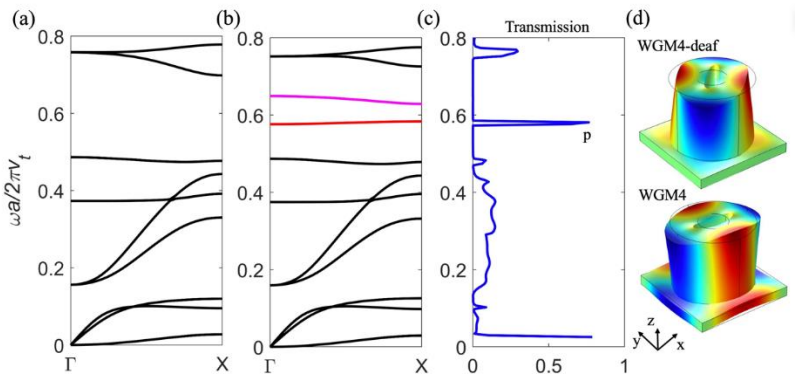

Figure 2.9. (a) Dispersion curves along ΓX direction for full pillar unit cell in a square lattice; (b) same as in (a) but for hollow pillar case ; (c) the corresponding transmission curve with respect to (b) ; (d) real part of z-displacement component of the eigenmode of the red and pink bands at the Γ point. The geometric parameters are: height of pillar h/a=0.45, radius of pillar r/a=0.4, inner radius of hollow pillar r_i/a=0.145, plate's thickness e/a=0.1, where a is the lattice constant. This figure is based on results from Ref. [59].

The acoustic path of WGM around the hollow pillar of WGM is a multiple integer of the wavelength, equal to 2 for the presented WGM4. Therefore, the wavelength qualitatively behaves in the form of $\lambda=\pi(r+r_i)/2$. By increasing the inner radius, the frequency of WGM4 will redshift even to a low-frequency band gap. It is has been shown that the WGMs can be efficiently tuned to cross a wide frequency band by varying the inner radius of the hollow pillars.

As the WGMs can be designed to cover the full Bragg band gap by varying the inner radii of the hollow pillars, several narrow passbands can be expected for a mixed system composed of different inner radii. Here, we demonstrate the design a mono- and multichannel wavelength division multiplexers by inserting appropriate waveguides in a (5 × 5) supercell phononic crystal plate.

For the multichannel wavelength multiplexer, the phononic plate contains two linear hollow pillar waveguides separated from each other by a line of full pillars, which prevents leakage between the two waveguides as shown in Fig.2.10a. We present the displacement fields of the transmitted wave through the two waveguides corresponding to two narrow pass bands in the Bragg band gap. Actually, the transmission of two narrow pass bands does not need two separate waveguides. In Fig. 2.10b, a monochannel wavelength multiplexer is considered, where the waveguide is constituted by alternating hollow pillars with two different inner radii. It is able to transport two different wavelengths through the same channel, as clearly observed in the displacement fields in Fig. 2.10b. The wave transmission originates from evanescent waves that allow for the overlapping of the elastic fields between two next nearest neighbor hollow pillars with the same inner radius. In Fig.2.10b, the displacement fields at two different passing frequencies are exhibited, where the enhancement of the fields inside the corresponding hollow pillars is obviously observed for each frequency.

Other ways to obtain a high quality factor pass band may also be realized based on WGMs, for instance by designing a cavity oriented perpendicularly to the direction of propagation [59]. It is worth noticing that such applications of WGMs can also be realized inside a low frequency hybridization band gap instead of a Bragg gap [59].

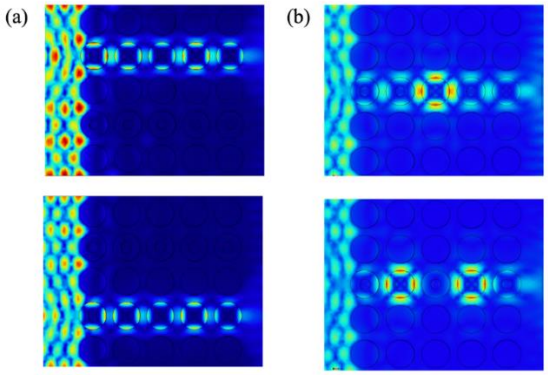

Figure 2.10. Application of WGM4 in a multichannel wavelength multiplexer (a) and a monochannel wavelength multiplexer (b). The upper and lower panels correspond to two different narrow pass bands for each column. This figure is adapted from Ref. [59].

2. Tunable property by liquid filling of the hollow pillars

The existence of hollow pillars provides the possibility of filling them with a liquid. As the liquid and solid parts are coupled, the frequency of th anomalies e WGMs are affected by the acoustic properties of the liquid (e.g., the type of the liquid and its temperature) as well as its height level inside the hollow pillar. In general, for a given inner radius, increasing the height level of the liquid will decrease the frequency of WGM; however there is room for anomolies. For example, for a given inner radius and height level of the liquid, the frequency of WGM is lower when the liquid is mercury than that when it is water–since the impedance of mercury is much higher than that of water [60].

The liquid-filled hollow pillars will also give rise to new localized modes inside the band gaps, such as compressional modes of the liquid. Fig. 2.11a shows the dispersion curves of a phononic crystal where the hollow pillars are fully filled with water. In this example, the height of each pillar is h/a=0.4, the outer and inner radii are respectively r/a=0.4 and r_i/a=0.1 and the plate's thickness is e/a=0.1. The parameters of water are taken at room temperature (25°C), namely density of 998 kg/m^3 and acoustic velocity of 1490 m/s. In Fig. 2.11a, the new blue and cyan bands appear in addition to the black bands associated with the solid. The pressure fields for these two bands reveal that they respectively correspond to the first compressional mode (blue band) and the second compressional mode (cyan band). This can be well explained by the simple physical model of a tube of height h_{liq} with rigid lateral and bottom boundaries and a free upper boundary. The expression of the (n+1)th compressional mode is $f_{n+1}=(2n+1)c/4\ h_{liq}$, where n is the resonant integer number as 0, 1, 2,…, and c is the acoustic velocity of

the liquid. One can easily notice that the frequency of the second mode is three times that of the first mode, $f_2 = 3f_1$, which is also verified by the blue and cyan bands in Fig. 2.11a.

The liquid compressional modes have high quality factors and owing to their sensitivity to acoustic velocity, they are good candidates for sensing applications. For instance, the acoustic velocity of water will increase when the temperature rises. In Fig. 2.11b, we show that the frequency of the second liquid compressional mode increases within the Bragg band gap when temperature rises from 0 to 70°C, demonstrating the application of this structure for temperature sensing in water [60]. In addition, this configuration may also be applied to other application fields involving a dependence with the acoustic velocity, such as the identification of molar ratio for a mixture of two different liquids. It is to be noted that a solid/liquid coupled mode can also be generated by liquid filling in the hollow pillars whose frequency is sensitive to both the height level of the liquid and the inner radius of the hollow part.

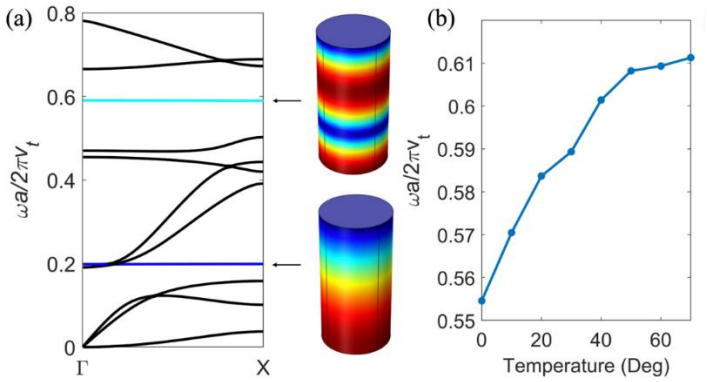

Figure 2.11. (a) Dispersion of a hollow pillar unit cell fully filled with water. The first and second liquid compressional modes are displayed in blue and cyan bands, respectively, along with the corresponding pressure fields. (b) The temperature sensing application of the second compressional mode. This figure is based on results from Ref. [60].

E. Vibration of multilayer pillars

We show here an illustration of a phononic crystal made of an array of multilayered pillars, for surface acoustic waves control. Here each pillar is comprised of a periodic stack of alternating layers as seen in Fig. 2.12(a). We refer to this as a *phononic pillar*. The yellow layers correspond to PMMA and the blue ones to silicon. The novelty of this structure is that the pillar in the unit cell behaves like a 1D phononic crystal, so it allows band gaps that prohibit wave propagation along the pillar's vertical axis. Therefore, it can support localized modes in a cavity or at its top surface that are very well confined and can intercat with the surface acoustic waves of the substrate to give rise to Fano resonances or other sharp features relevant for sensing applications.

Figure 2.12(b) represents the corresponding dispersion curves in the ΓX direction within the Brillouin zone. Below the silicon sound line, the modes are localized at the surface of the silicon substrate and/or inside the pillars. However, among these modes, three specific modes noted A1, A2, and B appear in the orange shaded regions which correspond to the band gap of the periodic multilayer

pillars. In contrast, the displacement fields of the other SAW branches are distributed throughout the pillars. The displacement field amplitude together with the vibration of these three modes plotted in Fig. 2.12 (c) show that their vibrations are mainly localizes at the bottom of the pillar, i.e., at the interface of the pillars with the substrate. Moreover, one can see that the motions of modes A1 and A2 resemble the bending vibrations of the pillar, while mode B looks like a compressional vibration.

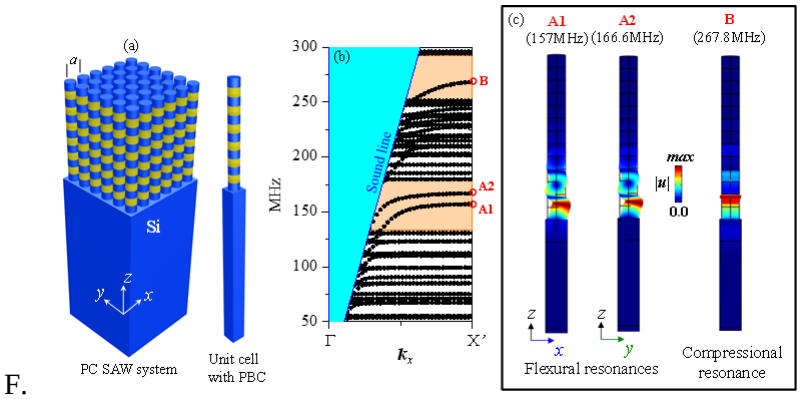

F.

Fig.2.12. (a) Phononic crystal structure consisting of a square array of a multilayer phononic pillars on a silicon substrate surface. The yellow and blue layers correspond to PMMA and silicon, respectively. The set of geometrical parameters are a = 1 µm, $h = h_{silicon} = h_{PMMA}$ = 3.5 µm and the pillar diameter is d = 5µm. (b) Band structure for SAW propagation along the Γ-X direction. (c) Total displacement field in the unit cell for modes denoted A1, A2 and B in (b). This is reproduced from Ref. [94].

Next, we consider one row of such pillars arranged on the surface and study the interaction of an incident Rayleigh wave with this line of pillars as shown in Figs. 2.13(a) and 2.13 (b). The transmission spectrum plotted in Fig. 2.13(c) shows SAW attenuation in the shaded region where the amplitude of the u_z component decreases to 0.4 at 161 MHz. The shaded area corresponds to the band gap of the phononic pillar. At this frequency, we plot in Fig.2.13(d) the total displacement field in the phononic pillar as well as the u_z component in the substrate. We deduce that the SAW attenuation is caused by the excitation of a localized mode as the confined mode denoted A1 in Fig. 2.12(b). This mode is localized at the bottom of the pillar.

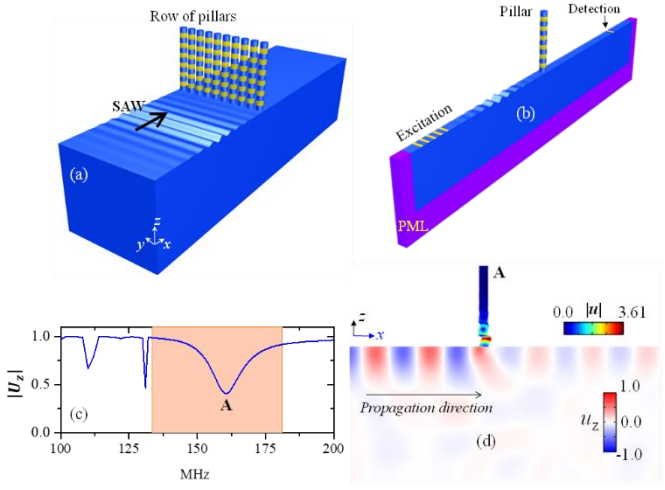

G.

H.

Figure. 2.13. (a) Schematic view for the transmission through one row of phononic pillars. (b) Unit-cell used in the simulation. (c) Transmission results: normalized amplitude of out-of-plane displacement U_z. The shaded region corresponds to the band gap of the PMMA/Si pillar. (d) Total displacement field in the pillar as well as the u_z component in the silicon substrate for SAW. This is reproduced from Ref. [94].

F. Pillared plate encompassing multiphysics

The simultaneous existence of photonic and phononic band gaps and the confined phonon-photon interaction has opened up the field of cavity optomechanics [174]. The section first provides a brief overview on the existence of *phoXonic* (dual phononic-photonic) band gaps in the type of structure comprise of a periodic array of pillars deposited on a plate of finite thickness. Then, we give an example of the interaction between elastic waves and localized surface plasmon modes in a system of gold nanocylinders separated from a thin gold film by a very thin dielectric spacer of few nanometers. This model is used to investigate the efficiency of the coupling between an elastic deformation and the plasmonic modes.

1. Dual phononic and photonic band gaps

Here we examine theoretically the simultaneous existence of phononic and photonic band gaps in a periodic array of silicon pillars deposited on a homogeneous thin silica plate. Square, triangular, and honeycomb lattices have been investigated. We discuss the most suitable cases for dual phononic-photonic band gaps, especially in comparison to the traditional structures made out of periodic holes in a plate. The calculations are focused on a structure where silicon pillars are deposited on a silica plate. Besides the technological interest on silicon structures, the selection of these materials is also important for the simultaneous existence of phononic-photonic band gaps. The existence of phononic gaps is not much affected by the choice of the materials as discussed earlier, although the frequency and width of the gaps are material-dependent.

In the closely related field of photonics, Johnson et al. [175] have studied the band structure of a periodic array of silicon rods in air and shown the existence of a band gap for odd symmetric modes only (inplane magnetic field). However, in this work, the height of the pillars was taken equal to two times the lattice parameter and the result displayed similarity with the case of an infinite 2D structure where only a TM gap can be created. It is observed thatdecreasing the height of the rods to values lower than the lattice parameter allows the opening of a complete photonic gap for the guided modes. Therefore, one can expect that the low refractive index of SiO_2 may enable us to keep such a property even in presence of the thin plate. In Ref. [45]. a detailed study of both the photonic and photonic band structures was conducted. A search for the situations displaying band gaps for both excitations was also reported [45]. In Fig. 2.14, we give an illustration of the dispersion curves for the three types of lattices investigated. It can be seen that it is more suitable to search for a photonic gap around or below the reduced frequency 0.4, since above this range the band gap will be restricted only to a small part of the Brillouin zone below the light cone.

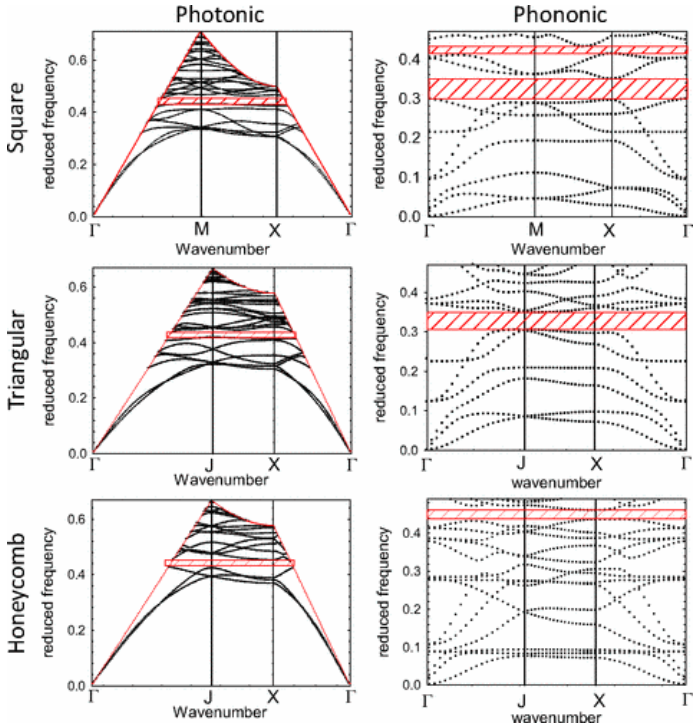

Figure 2.14. Photonic (left) and phononic (right) dispersions curves calculated for (a) a square array with the set of parameters e_{SiO2}/a = 0.2, h_{Si}/a = 0.8 and f = 0.4, (b) a triangular array with the set of parameters e_{SiO2}/a = 0.5, h_{Si}/a=0.8 and f = 0.5 and (c) a honeycomb array with the set of parameters e_{SiO2}/a = 0.4, h_{Si}/a = 0.7 and f = 0.3. This figure is reproduced from Ref. [45].

2. Elasto-plasmonic interaction

Here we provide an illustration of the theoretical and numerical investigation of the coupling between elastic and localized surface plasmon modes in a system of gold nanocylinders separated from a thin gold film by a dielectric spacer of few nanometers thick. This system supports plasmon modes confined between the bottom of the nanocylinder and the top of the gold film, which arise from the formation of interference patterns by short-wavelength metal-insulator-metal propagating plasmons.

The structure is displayed in Fig. 2.15a, which consists of a square array of gold nanopillars deposited on a multilayered membrane composed of gold and silica. The simultaneous consideration of the plasmonic, elastic, and coupled elasto-plasmonic aspects has been numerically studied using the finite-element method. In order to characterize the elasto-plasmonic interaction, we use a quasistatic approximation, which consists of a recalculation of the shape of the elastic modes at several selected instants of an elastic period (or several selected material phases) where the shape of the structure being fixed at these instants. This is justified by the fact that the plasmonic frequency is several orders of magnitude larger than the elastic frequency.

In Fig. 2.15b, it shows two elastic modes at F=4.2GHz and F=5.6 GHz (adopting the notation used in the Ref. [175]) which correspond to a quadrupolar mode and a vertical compressional mode, respectively. The evolution of the absorbance spectrum around the wavelength of the metal-insulator-metal localized-surface-plasmon (MIM-LSP) mode at 750 nm for these two modes is shown in Fig. 2.15c. The deformed geometry of each mode is calculated for different phases $\psi = \Omega t = 2\pi Ft$ during

half an acoustic period. At 4.2GHz, the mode has observable modifications in absorption spectrum for different phases. More obvious modifications are induced for 5.6 GHz in the range of wavelengths where the MIM-LSP modes are excited.

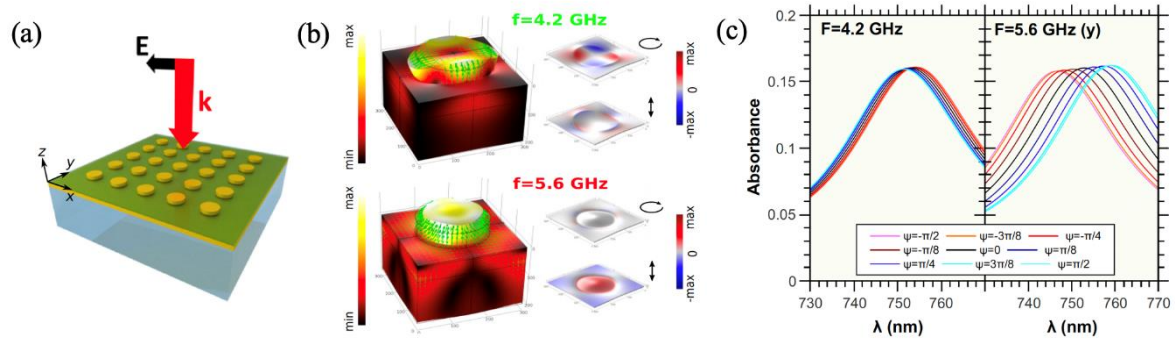

Figure 2.15. Geometry of the model. (b) Elastic modes at two frequencies where the left is the total displacement field and the right is the deformation under the pillar. (c) Evolution of the absorbance spectra for different values of the elastic phase for the elastic modes at 4.2 and 5.6 GHz, around the wavelength of the main (*n*,*p*) = (1,2) MIM-LSP mode. This figure is reproduced from Ref. [176].

This study may highlight the coupling mechanisms between localized plasmon modes and elastic modes, which is based primarily on the fact that the "elastic function" is mostly supported by the gold nanoparticle while the "plasmonic function" is essentially supported by the dielectric cavity under the nanoparticle. This aspect, which is in contrast to previously investigated systems, gives additional flexibility for the engineering of elasto-plasmonic devices with the possibility of loading or changing the volume of the nanoparticle in order to tune the frequencies of elastic modes without significantly affecting the plasmonic aspects. Furthermore, the interaction between the elastic and plasmonic modes may be influenced by using spacers with different mechanical properties but similar refractive index.

Chapter 3 Pillared metaplates: Advanced geometric configurations

A. Engineering of large low-frequency band gaps

1. Trampoline metamaterials

In most applications in phononics, including metamaterials and metasurfaces, large band-gap size is generally desirable. Maximization of band-gap size by unit-cell optimization has been actively pursued for phononic crystals[177-179]; in contrast, less attention has been focused on band-gap widening in locally resonant acoustic/elastic metamaterials. In this subsection, we review the dispersion characteristics of locally resonant elastic metamaterials formed by the erection of pillars on the solid regions in a plate patterned by a periodic array of holes [65]. The solid regions effectively act as springboards that enhance the resonance behavior by the pillars when compared to the nominal case of pillars on a plate with no holes. This local resonance amplification phenomenon, which has been defined as the *trampoline effect*, was shown to cause subwavelength bandgaps to increase in size by up to a factor of 4.

To demonstrate the trampoline effect, we will examine a plate configuration formed by the merger of a periodically pillared plate foundation [Fig. 3.1(b)] with a standard phononic crystal plate created by removal of a periodic array of holes [Fig. 3.1(a)] [65]. The outcome is a locally resonant elastic metamaterial consisting of pillars standing on the solid regions of a phononic crystal plate [Fig. 3.1(c)]. This architecture allows each pillar to be rooted in a more compliant base due to the presence of the holes, thus rendering the base to behave effectively as a springboard that allows the pillars' resonant motion to be enhanced. This enhancement is reflected in the relative size of the locally resonant subwavelength band gap, which is seen to experience an enlargement in size by a factor of approximately 2.5 compared to the pillared plated with no holes.

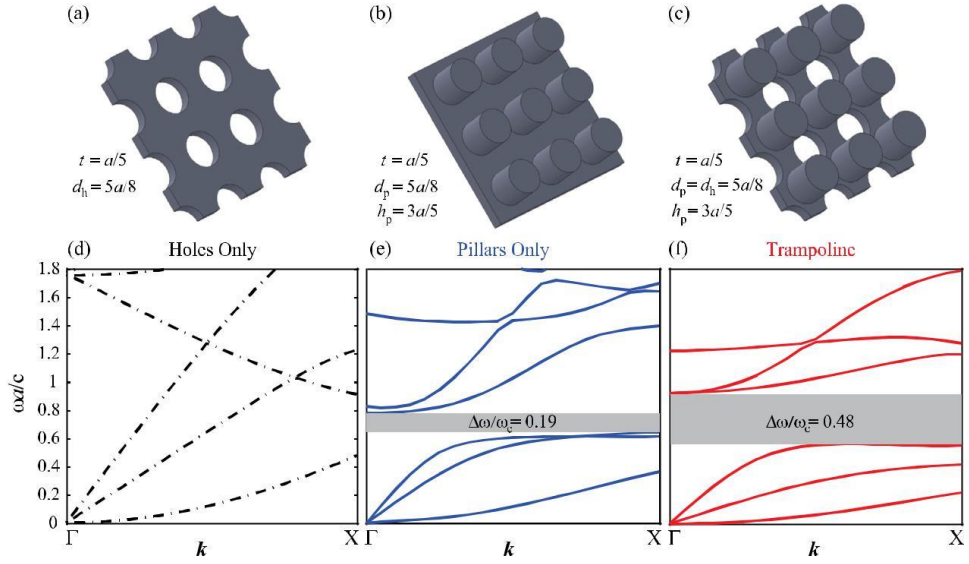

Figure 3.1. Demonstration of a trampoline metamaterial. The top panel shows schematics of (a) a standard phononic crystal plate (consisting of a periodic array of holes), (b) as elastic metamaterial in the form of a periodic array of pillars on a plate, and (c) a trampoline metamaterial consisting of a periodic array of pillars on a plate intertwined with a periodic array of holes. The solid material is silicon with properties: density ρ = 2330 Kg/m3, and Lamé constants λ = 85.502 GPa, μ = 72.835 GPa. The dispersion diagram of the three configurations for wave propagation in the ΓX direction is shown in the bottom panel. In the frequency range displayed, the phononic crystal has no bandgaps. (d), the standard pillared plate exhibits a subwavelength bandgap with a relative size of 0.19 (e), and the proposed trampoline plate features an enhanced subwavelength band gap with a relative size of 0.48. This figure is obtained from Ref. [66].

To further examine the trampoline effect, the problems shown in Figs. 3.1(b) and 3.1(c) were extended for a range of values of pillar height and hole diameter. A map of the size and location of the lowest band gap (also along the ΓX direction) as a function of pillar height for a hole diameter of d_h = 5a/8 is given in Figure 3.2(a). The same results are also presented in Fig. 3.2(b) but in the form of a plot of the relative band-gap size, $\Delta\omega/\omega_c$, versus pillar height, where ω_c is the band-gap central frequency. The blue solid line in Fig. 3.2(b) is for the standard, unholed pillared plate and is provided for comparison. The dotted, dashed, and solid red lines represent the relative band-gap size for the trampoline metamaterial configuration for different values of d_h. In addition to d_h = 5a/8, two other hole

diameters are considered, $d_h = 3a/8$ and $d_h = 4a/8$ (noting a constant increment of $a/8$ between the three diameters). It is observed that for the two additional trampoline plate cases, the relative band-gap size is larger than the case of the standard unholed pillared plate. This shows that the trampoline effect is present also in the lower hole diameter cases. However, the incremental enlargement of relative bandgap size is more significant at higher values of hole diameter, which is due to the quadratic decrease in the springboard area as d_h is increased.

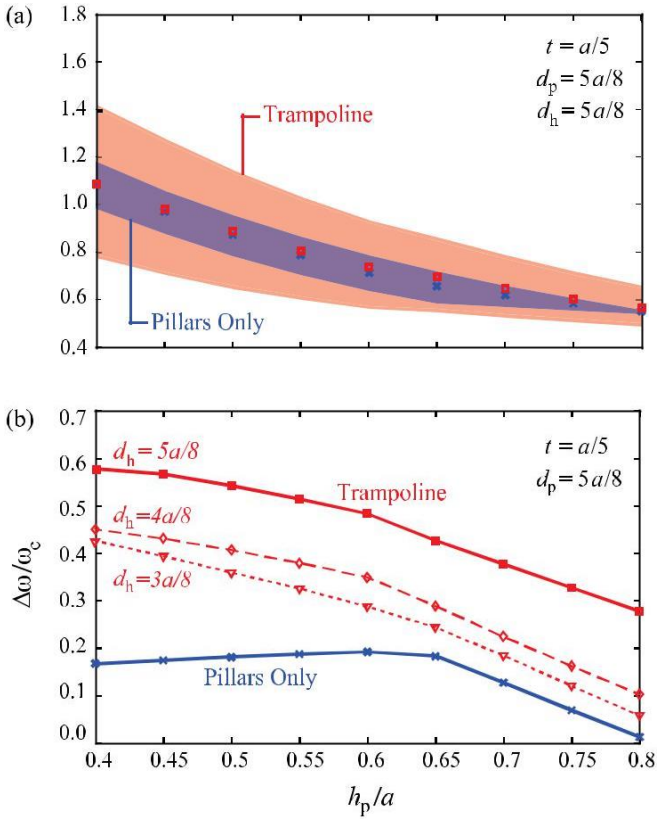

Figure 3.2. Map of absolute (a) and relative (b) band gap as a function of normalized pillar height for a trampoline plate (consisting of pillars and holes) compared to a standard pillared plate (consisting of only pillars). The trampoline effect results in an increase of the subwavelength locally resonant band gap by a factor ranging from roughly 2 to 4 for geometries, where the original Δω/ωc is greater or equal to 0.1. This figure is obtained from Ref. [66].

The relative band-gap size attainable by the trampoline effect is remarkable. For the parameter set of $d_h = 5a/8$ and $h_p/a = 0.4$, the size of the relative band gap is close to 0.6 (i.e., 60%). This is a significant improvement over reported relative band gap sizes in the literature for acoustic/elastic metamaterials in general and specifically for pillared metamaterials, which usually fall within the range of 20% – 30% for a partial bandgap.

These results demonstrate that the trampoline effect in a plate facilitates the utilization of subwavelength metamaterial properties over relatively broader frequency ranges than the case when only pillars are employed.

2. Tailored metamaterials

In the previous section, trampoline metamaterial plates were reviewed as a concept for widening and lowering a local reasonace hybridization band-gap. In this section, we discuss a mechanism to significantly widen the Bragg band gap and extend it to the low frequency domain, meanwhile the relative width of the low-frequency hybridization band gap is also enlarged. The physical model is based on the pillared unit cell configuration of Chapter 2.D.1. As seen in the inserts of three geometries in Fig. 3.3, the pillars are connected to each other by cross bars with tunable widths instead of the use of a homogeneous plate as a common base medium. The widths of the bars are b/a=1, 0.5, 0.1 at the left, middle and right panels, respectively. The lattice constant is a. The entire unit cell in this example is made of silicon.

To explain the mechanism behind the trend observed in Fig. 3.3, let us first start with the case b/a=1. A Bragg (blue) and a hybridization (red) band gap appear in the dispersion curves along the ΓX direction with relative size 0.45 and 0.26, respectively. The relative size of a band gap is defined as $\Delta\omega/\omega_c$, where $\Delta\omega$ is the width and ω_c the central frequency of the gap. The Bragg band gap is divided into two parts by a narrow band denoted A, whose eigen mode at the Γ point is also displayed in Fig. 3.3. One can clearly notice that this branch A exhibits a high localization in the plate at the four corners of the unit cell. In addition, a relatively flat band B falling in the frequency domain of the bulk bands below the Bragg gap is associated to the torsional resonance of the pillars, as can be seen from its eigenmode. The presence of band A and the interaction between band B and other bulk bands affect the property of the Bragg gap. To eliminate these two effects, we propose the concept of a tailored metamaterial that consists of a pillar connected by two tunable crossing bars.

Indeed, when the width of the bar reduces to 0.5, the four corners of the unit cell turn into eight new corners of the two crossed bars. Since the distance of the two corners at one edge of the bar is equal to the bar's width and decreases, the frequency of the mode A moves to a higher frequency, about 0.85 for b/a=0.5. Meanwhile, the torsional mode B downshifts to lower frequency. These two changes result in a wider Bragg band gap with lower gap edge whose relative size increases to 0.76, as seen in the model panel of Fig. 3.3. Meanwhile, the hybridization band gap is also enlarged a bit and moves to lower frequencies with a relative size as 0.41. When the width of the bar further decreases to 0.1, the Bragg band gap extends to the low frequency domain and its relative size greatly increases to 1.22 while the relative size for the hybridization gap increases to 0.52. The unit cell with narrow bars makes the pillar easier to rotate and bend, so that the band B and the hybridization band gap red shifts. Such dispersion properties bring have potential for utilization in subwavelength studies of acoustic/elastic metamaterials.

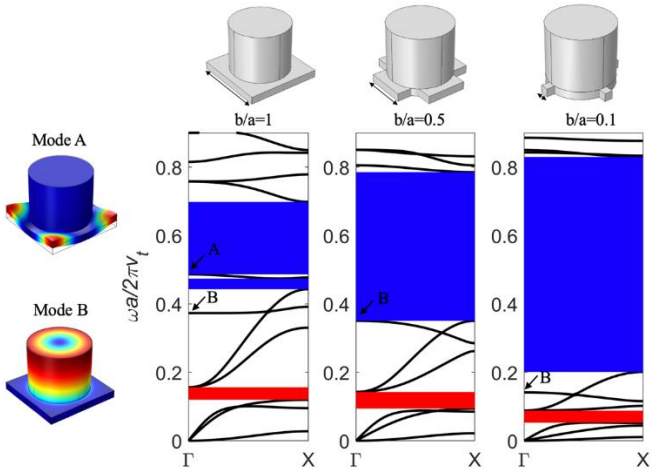

Figure 3.3. Dispersion for pillared phononic crystals connected by thin bars with the bar's width as *b*/*a*=1 (left), 0.5 (middle) and 0.1(right). The Bragg and hybridization band gaps are respectively marked in blue and red. The geometries of the unit cells are displayed on top of each dispersion curve, respectively. The eigen modes of band A and B at the Γ point are also represented at the left. This figure is adapted from Ref. [61].

The evolutions *of* the Bragg and hybridization band gaps in the ΓX direction as a function of the bar's width are summarized in the left panel of Fig. 3.4, where the torsional band is shown in cyan color. As the bar's width reduces, the frequency of the torsional mode blue region shifts towards outside of the Bragg band gap. The Bragg band gap becomes much wider and remarkably extends to the low frequency domain, hence becoming an extra wide band gap. The hybridization gap gradually moves to lower frequencies. The evolutions of the relative sizes of the two gaps are presented in the right panel of Fig. 3.4. Since the width of the Bragg gap obviously enlarges when the width *b*/*a* is smaller than 0.7, its relative size almost linearly increases, nearly three times for *b*/a=0.1 to 1. On the other hand, the relative size of the hybridization gap gradually increases and becomes two times higher. As a result, engineering dispersion bands by tuning the width of the cross-connecting bars is proven to be an effective approach for widening and lowering band gaps.

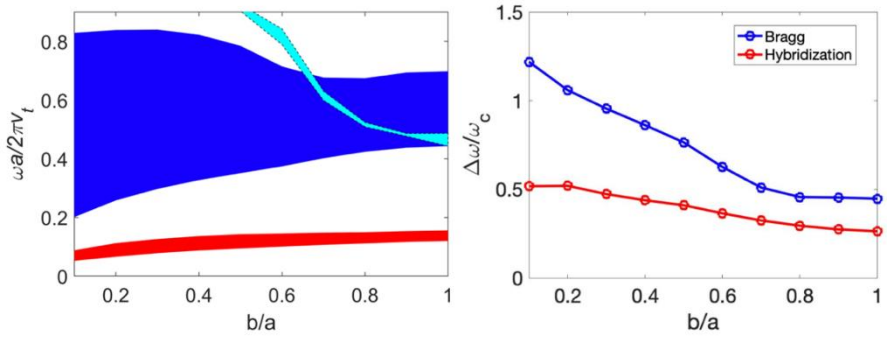

Figure 3.4. (Left) Evolution of the Bragg (blue) and hybridization (red) band gaps as a function of bar's width *b*/*a*. The cyan color represents band A, a torsion mode. (Right) Relative size of band gaps as a function of bar's width *b*/*a*. This figure partially includes results from Ref. [61].

B. Pillared GRIN phononic plate

1. Introduction

Focusing of acoustic or elastic waves via flat phononic lenses is definitely one of the most striking phenomena that arise from the artificial periodicity of phononic crystals (PCs). After the first experimental demonstration of the phenomenon was achieved in 2008 [180], an intense activity has developed to optimize the geometrical and physical parameters of acoustical lenses in order to realize the exceeding high spatial resolution [181-186]. These promising perspectives for acoustic imagery relate to the fact that PCs are systems in which one can control the wave propagation at the wavelength –a major disadvantage stems from the fact that evanescent waves emerging from the object at cannot reach the image plane because of the exponential decay of their amplitude. In contrast, in lenses with negative index, the evanescent waves have their amplitude that increases during the transmission through the medium. While the waves decay again down to their initial level after emerging from the lens, they can still contribute to the resolution of the image.

From the perspective of super-resolved imaging–which has emerged as one of the 'hottest' topics in the field–PCs suffer from some drawbacks that may prevent them from large dissemination. First, as a consequence of the exponentially decaying amplitude of the evanescent waves, the super-resolution attribute applies only to near-field imaging. Actually, if the source is located at a distance from the lens that is greater than one wavelength, the decay turns out to be prohibitive for the evanescent component to reach the lens and the super-focusing effect cannot be achieved. Then, in PCs the negative refraction of elastic waves, which is the starting point of the super-focusing effect, can be controlled through the band structure. In fact, this phenomenon is the direct consequence of the bands folding and relates therefore to the negative slope of some acoustical branches [187]: only elastic waves with frequencies above the first band gap can contribute to the superlensing effect. Their wavelengths are thus comparable or even smaller than the period of the PC, and the propagation therein comes with large and even prohibitive scattering of the waves.

Using PCs to focalize elastic waves with frequencies in the first branch of the Brillouin zone where negative refraction effects are not involved is however possible if considering *gradient-index phononic crystals* (GRIN PCs) [135, 188-198]. These 2D systems are engineered with a gradual variation of their constitutive parameters (e.g., filling factors [189, 195, 199], geometry of the inclusions [135], or material properties [188]) along one direction. As a result, they feature a sound velocity gradient along that direction, making it possible for collimation, the convergence or the focalization of an incident wave. When an acoustic beam propagates through a 2D GRIN PC, it encounters redirection at every virtual interface between layers, resulting in successive reorientations of the acoustic beam inside the structure. Thus, by gradually modulating the parameters of a GRIN PC, one may create a curved path for the acoustic waves [135, 188-195]. Inspired by optical devices that already exist, different designs for

acoustic waves have been proposed, including Maxwell's fish eyes [200] and circular Luneburg lenses optimized for focalizing simultaneously the three elastic modes that may propagate in a plate, namely shear horizontal, symmetric, and antisymmetric Lamb modes [137]. However, whether it is for optical waves [201-203] or for elastic waves [135, 188, 189, 195, 199, 204] none of the proposed designs has allowed for overcoming the diffraction limit to date; this is because of the total internal reflection of the waves with high **k** wavecectors which hinders the transmission to the background for external focusing. On the optics side, it was further proposed to use metamaterials featuring extraordinary refractive properties instead of photonic crystals [193, 194, 198, 205, 206], and the resolution beyond the diffraction limit for visible light was actually demonstrated analytically [205]. However, such success has not been obtained with elastic waves in solids so far [193, 194, 198, 206], nor has it been investigated how large should the acoustical refractive index (i.e., ratio of the **k** vector in the lens to the **k** vector in the background) be to attain this objective. Metamaterials with local resonances generally fulfill this latter requirement since they may display very slow sound velocity, at least near resonances [16, 19, 23, 66, 77, 86, 116, 117, 131, 186, 207-212]. Besides, depending on the shape and dimensions of the resonant inclusions, the resonances may arise at a very low frequency as compared to the Bragg gap, in a region of the reduced Brillouin zone where effective theories apply. This has been demonstrated both theoretically and experimentally, with 2D PCs made out of an array of cylindrical pillars regularly erected on a homogeneous thin slab [19, 77, 86, 116, 117, 131, 212]. This structure, in particular, deserves special attention. Indeed, a single pillar on a plate has compressional and bending resonances that may lead to the dynamic effective modulus and mass density both being negative when a number of them are gathered to form a metamaterial. Moreover, since the compressional resonant frequency and the bending resonant frequency are mainly sensitive to the height and to the diameter of the pillar respectively, they can be tuned almost independently from each other [90]. When associated with a GRIN phononic lens on a plate, it is expected that the bending resonances and the Lamb waves propagating in the plate exhibit polarization coherency, thus allowing for the enhancement of the evanescent waves and, in turn for the forming at the focus of a spot containing finer information.

2. Trampoline GRIN structure

Based on GRIN phononic plate concept, Zhao et al. [141] esigned acoustic lenses built on a silicon plate by drilling a square lattice of air holes with a period of *a* and with radii gradually tailored along the transverse direction, as shown by the SEM image in Fig. 3.5(a). An array of identical silicon pillars was erected on one face of the plate, on each junction between each set of four air holes. This represents a combination of the trampoline metamaterial concept [66] and the GRIN concept. The basic unit is shown in Fig. 3.5(b). They have shown in Ref. [141] that such a structure, which we may describe as a *trampoline GRIN structure*, allows for the focalization of an A_0 Lamb mode within the homogeneous substrate behind the metalens, over a spot having a transverse size beyond the diffraction limit.

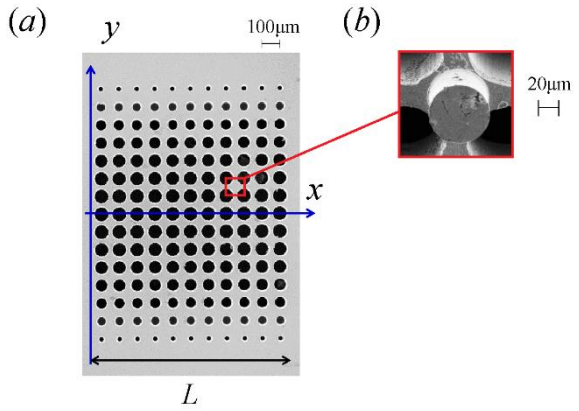

Figure. 3.5. (a) Scanning electron microscope (SEM) image of the back side of a sample of a trampoline GRIN structure, (b) SEM image of a silicon pillar centered between four air holes on the front side of the sample. This figure is reproduced from Ref. [141].

In the low frequency region, where the wavelength is much larger than the lattice parameter, the refractive index along each line of inclusions (i.e., the ratio of the wave number along ΓX to the wave number in the background) was designed to feature a hyperbolic secant profile. This profile, which can be formally written as $n^2(y) = 1 + (n_0^2 - 1)\,\mathrm{sech}^2(\alpha y)$ where α is the gradient coefficient, and n_0 is the refractive index along the central line of inclusions at the working frequency, allows for an exact determination of the acoustical rays. Moreover, a lens whose index features a hyperbolic secant profile is free of aberration, i.e., any ray normally incident on the lens converges to a single point on the axis [48, 209].

The band diagram of the trampoline GRIN structure shown in Fig. 3.6 explains the forming of a subwavelength spot at the focus of the lens. In this figure, the antisymmetric Lamb mode A_0 is drawn for a structure with (red solid line) and without (black solid line) pillars. In the inset are shown the normalized modal displacements associated with the A_0 mode for propagation along ΓX at the frequency of the red flat branch. Unambiguously, the hybridization between the A_0 mode in the air/silicon PC, polarized on the *x*-*z* plane, and the lowest-order flexural resonance of the pillar governs the displacement field–which is totally dominated by a vibration localized on the pillars.

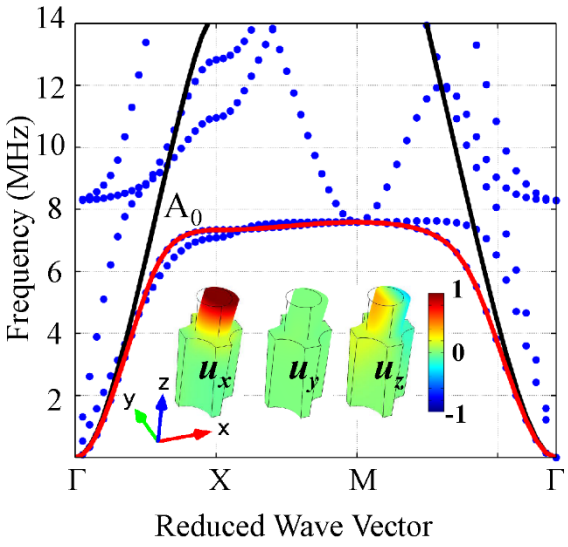

Figure. 3.6. Band structure (dotted curves) of the trampoline GRIN structure along the central layer of the acoustic lens. The A_0 band is highlighted by the overlapping red line while the black line indicates the A_0 band along the central layer without pillars. Inset shows the normalized modal displacements of the A_0 mode at the X point in the Brillouin zone. This figure is reproduced from Ref. [141].

It can be deduced from these dispersion curves that, at resonance, the pillars act as elastic sources emitting in the plate Lamb waves at the frequency of the bending eigenmode [90], which in turn allows for enhancement of the evanescent waves emerging from the lens.

3. Beam path in GRIN plates

Any ray normally incident on a GRIN lens featuring a refractive index with a secant hyperbolic profile converges to a single point on the axis, at the focal length f_1. This length only depends on the gradient coefficient α through $f_1 = \pi/2\alpha$. However, deviation between the focal distance predicted by this formula and that derived from numerical simulations, or even experimental measurement, may sometimes be significant, even in the homogenization frequency range [135, 188, 189]. There are several reasons for this possible deviation. First, the actual 2D acoustic lenses feature discretized indices, which may be imperfectly represented by a continuous gradient. However, this is probably not the most relevant reason since small deviations of a few percent were observed for a wavelength only five times larger than the period [135, 188, 189]. The observed disagreement between the theory and numerical simulations can be explained to a larger extent by the overall shape of the equi-frequency contours (EFCs). Actually, in PCs with large filling factors, the EFCs may depart from a circle, even at low frequency [135, 188, 189], therefore analyzing the trajectories in terms of an effective index may not be relevant. Instead, the effects of anisotropy are better described by considering both the group velocity and the **k** vector as the local parameters [213]. Based on the same idea, a Hamiltonian optics approach

has been proposed to study light propagation in graded PCs in the short-wavelength regime [214]. However, there have only been a few theoretical works able to perform a quantitative analysis of the ray trajectory in the homogenization range [215]. This was done, for instance, in Ref. [216] where an empirical approach allowed to accurately interpret both the position and the size of the spot experimentally measured in GRIN PC lenses with either a square lattice (the holes have different diameters and are regularly spaced along the *y*-axis) or the rectangular lattice (the holes have identical diameter but their separating distance varies along the *y*-axis).

Experimental evidence of the subdiffraction focusing with the trampoline structure is shown in Figs. 3.7(a). In this figure, the maximum of the out-of-plane displacement is measured on the free surface of the lens using an interferometric method. The displacement field is symmetric on both sides of the central layer at y=0, with the overall maximum just behind the lens, at the distance x=0.6a from the outlet interface. The agreement with the numerical simulations shown in Fig. 3.7(b), including both the focal position and the pattern of the displacements field, is excellent.

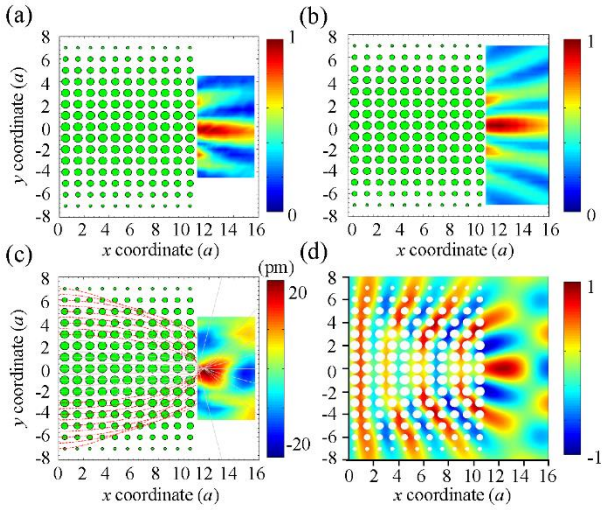

Figure. 3.7. (a) Experimental and (b) numerical distribution of the normalized maximum u_z behind the acoustic lens at the X point in the Brillouin zone (7.2 MHz), together with (c) experimental and (d) numerical snapshots of the near field focusing at 7.2 MHz. (c) The gray solid lines and the red dashed lines are for the ray trajectories with $|k_y| < k_B$ and $|k_y| > k_B$, respectively. This figure is reproduced from Ref. [141].

Figures. 3.7(c) and 3.7(d) display experimental and numerical snapshots respectively recorded at a moment when the amplitude is maximum at the focus. The phase patterns in the two snapshots are in good agreement each other. To further analyze the respective role of the propagative and evanescent waves, the calculated ray trajectories are drawn in Fig. 3.7(c): the gray solid lines are for the wave with $|k_y| < k_B$ along the exit interface (k_y is the component along the *y*-axis of the wave vector in the lens, k_B is the wavenumber in the background), leading to propagative waves behind the lens; whereas the red dashed lines represent waves with $|k_y| > k_B$, resulting in evanescent waves in the background. The rays corresponding to the propagative waves are converging to a small zone just at the focal position as

shown by the experimental results in Figs. 3.7(a) and 3.7(c) and by the numerical results in Figs. 3.7(b) and 3.7(d), giving rise to an overall maximum displacement just behind the lens. Figure 3.8 depicts the transverse profile of the normalized maximum u_z, measured experimentally (circular markers), computed using a finite-elements method (solid line), or analytically derived (dashed black line) [217].

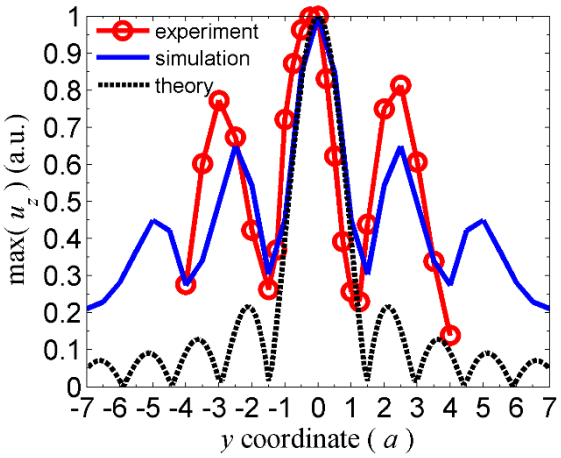

Figure. 3.8. Experimental (circle markers), numerical (blue solid line), and theoretical (black dashed line) transverse profiles of the normalized maximum uz at the focus. This figure is reproduced from Ref. [141].

The experimental data and the simulation and analytical results are in good agreement with each other. Actually, the full width at half maximum (FWHM) of the central peak equates to $0.42\lambda_B$, $0.43\lambda_B$, and $0.40\lambda_B$, respectively, i.e., less than half a wavelength and the subdiffraction focusing is achieved. However, the analytical results differ from the other two through the lateral peaks which are predicted to be smaller and sharper than it was experimentally and numerically found. Actually, it is assumed in Ref. [53] that there is identical contribution of each component k_y at the focus. However, in practice, the elastic waves undergo damping because of internal reflections and impedance losses at the interface. As a consequence, the normal displacements are smaller in the central portion of the lens $|y| < 2.5a$ than they are in the edges $|y| > 2.5a$ [Fig. 3.7(d)]. In other words, the losses are larger when $|k_y| < k_B$ than they are when $|k_y| > k_B$ along the outlet interface. Accordingly, both in simulations and in experiments the focus gathers a rate of propagative (evanescent) waves smaller (larger) than that predicted by the theory; this leads to a focus along the *y*-axis featuring large side peaks.

4. Conclusion

In conclusion, a GRIN acoustic metalens comprising a locally resonant uniaxial metamaterial allows for the nearfield subdiffraction focusing of an A_0 Lamb mode. This has been demonstrated both experimentally and numerically. Analyzing the profile of the transverse component of the **k** vector along the exit interface between the lens and the homogeneous background puts into evidence the contributions of both the propagative and the evanescent waves at the focus. The size of the spot behind the acoustic

metalens was both numerically and experimentally quantified: both showed that a focusing beyond the diffraction limit with the resolution close to 0.43 times the wavelength is achieved. These uniaxial metamaterial-based lenses can be implemented at very low frequencies, and they can be used to handle the propagation of other types of waves such as Rayleigh waves. The mechanism by which the evanescent waves get localized on the interface and gathered to the focus was investigated. The polarization coherence between the flexural resonance of the pillars and the A_0 Lamb mode in the plate enhances the evanescent wave along the interface through the elastic energy re-emitted by the resonators. This enhancement of the evanescent waves through the polarization coherence between the vibration of the resonators and the background medium can be seen as an advantageous strategy to designing metalens for other types of waves or to restoring the evanescent waves encountered in negative-index lenses.

Chapter 4 Metaline of pillars

A. Properties of a single pillar on a plate

1. Basic model

A pillar may exhibit bending (dipolar) and compressional (monopolar) resonances, which relates to negative effective mass density and elastic modulus for a pillared metamaterial [218]. The vibrational property of a single pillar deserves to be studied as it is the fundamental element of a pillared metastructure.

Let's consider a pillar deposited on a plate, as shown in Fig. 4.1a. The whole structure is made of silicon. Four points are marked on top of the pillar where displacements are detected. We define two orthogonal states $|a\rangle$ and $|b\rangle$ standing for a compressional and a bending modes, respectively. We assume that they can be composited into two other states $|y_1\rangle = \cos q|a\rangle + \sin q|b\rangle$ and $|y_2\rangle = -\sin q|a\rangle + \cos q|b\rangle$ with a coupling factor q. Then, the vibration on top of the pillar can be defined as $|y\rangle = Ae^{iy_1}|y_1\rangle + Be^{iy_2}|y_2\rangle$. For a compressional mode, all points on top of the pillar have the same vibration, so that we can write the vibration of point 1 as

$$|y_{p1}\rangle = |y\rangle = [Ae^{iy_1}\cos q - Be^{iy_2}\sin q]|a\rangle + [Ae^{iy_1}\sin q + Be^{iy_2}\cos q]|b\rangle. \quad (4.1)$$

For a bending mode, if the bending direction is along the Point 1-Point 3 line, the vibration of Point 3 can consequently be written as

$$|y_{p3}\rangle = [Ae^{iy_1}\cos q - Be^{iy_2}\sin q]|a\rangle - [Ae^{iy_1}\sin q + Be^{iy_2}\cos q]|b\rangle. \quad (4.2)$$

Therefore, we can further acquire

$$\frac{|y_{p1}\rangle+|y_{p3}\rangle}{2}=[Ae^{iy_1}\cos q- Be^{iy_2}\sin q]|a\rangle, \quad (4.3)$$

$$\frac{|y_{p1}\rangle-|y_{p3}\rangle}{2}=[Ae^{iy_1}\sin q+ Be^{iy_2}\cos q]|b\rangle. \quad (4.4)$$

From the above two expressions of Eqs. (4.3) and (4.4), we can recover the compressional and bending modes by considering the vibrations at Points 1 and 3 with addition and subtraction computations. [219]

As an example, we choose the geometric parameters : plate's thickness is 145μm, pillar's diameter is 50 μm, pillar's height is 245 μm. The fundamental antisymmetric Lamb wave is excited with the wavefront perpendicular to the Point 1-Point 3 line. The out-of-plane displacement is detected at Points 1 and 3, and operated on with Eq. (4.3) and (4.4) by normalizing to that of a point on a pure plate without the pillar. The first/second bending and compressional modes are clearly characterized by black and red solid lines in Fig. 1b with the associated vibrating motions, which provides a validation of the above method.

The resonant frequency of the pillar depends on the geometric parameters. From Fig. 4.1c, the bending modes significantly depend on the pillar's diameter, especially the second bending mode which will upshift to much higher frequency, even overlaps the compressional mode, when the diameter increases. In addition, one it is seen that the resonant frequency decreases for increasing pillar's height, decreasing plate's thickness, and increasing conical angle. The most salient feature is that the frequencies of the second bending and the compressional modes will superpose when the diameter of the pillar is around 100 μm, which may provide some useful properties as discussed in the next section.

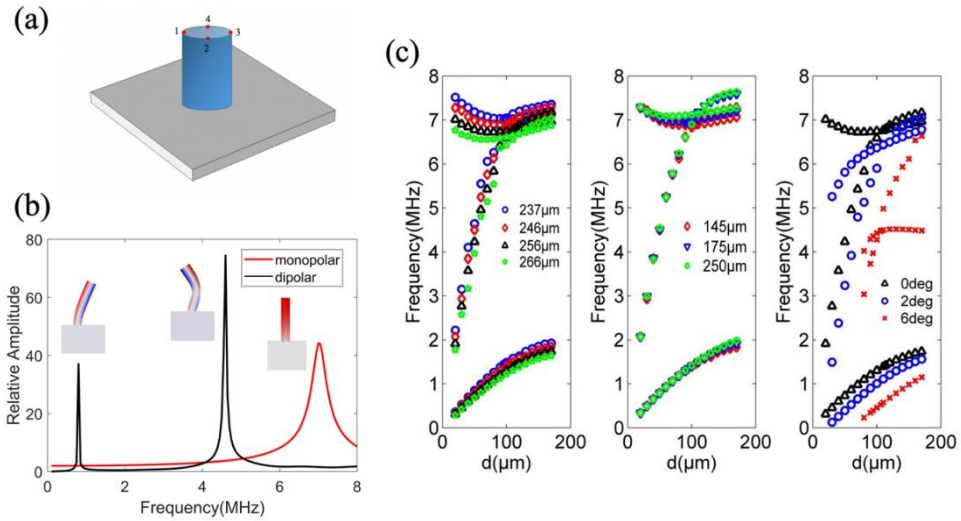

Figure 4.1. (a) A model for a single pillar on top of a plate, (b) resonant modes characterization and (c) variations of three resonant modes against diameter and height of the pillar (left), thickness of the plate (middle), and conical angle of the plate (right). This figure is based on results from Ref. [90].

2. Resonant and scattering property

When a pillar is in a resonant state, it scatters a wave radially. A scattered wave field can be acquired by subtracting incident the wave field from the total wave field. For the pillar in Fig. 4.1b, the three resonant states are separate in the frequency domain. Their scattered wave field are derived and presented in Fig. 4.2, from where the dipolar and monopolar fields properties are observed for bending and compressional modes, respectively. Therefore, the resonant pillar behaves as a point source.

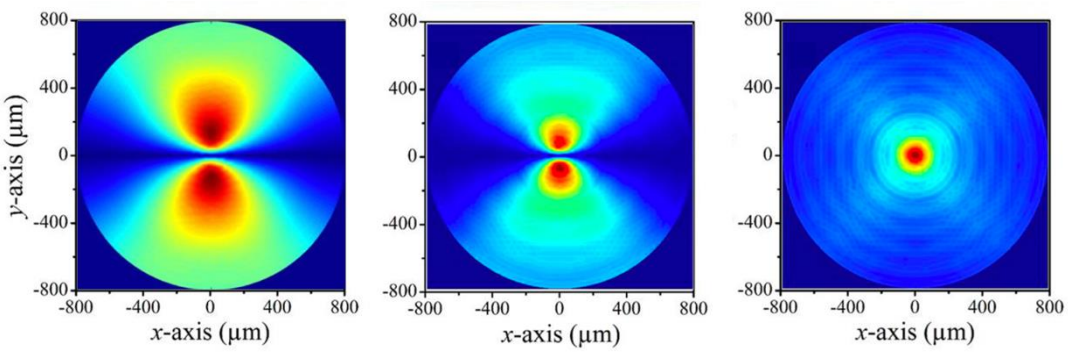

Figure 4.2. Amplitude distribution of the scattered Lamb wave by the pillar at the first (left) and second (middle) bending and compressional (right) resonant modes. This figure is based on results from Ref. [90].

3. Huygens-Fresnel principle

Huygens-Fresnel principle is a well-known concept in the theory of diffraction which says that each point on a wavefront can be regarded as a secondary-point wave source. Inversely, the interference of a set of point sources will generate a wavefront whose function can be designed. As a simplest example, in Fig. 4.3 we demonstrate that a line of identical point sources will generate a plane wavefront.

The phase and amplitude of a scattered wave by a compressional pillar are exhibited in column (a) upper and lower panels, respectively. Mathematically, five identical point sources are arranged in a line. The resulting field after interference is exhibited in column (b). The same operation but for nine identical point sources is done for column (c). The scattering field by a real line of nine resonant pillars is displayed in column (d). Comparing columns (c) and (d), one can observe that their scattering patterns are almost the same, which generates a plane wavefront as explained by Huygens-Fresnel principle. Any other functional wavefront can be designed by manipulating the phase distribution along the line, being a pillared metasurface.

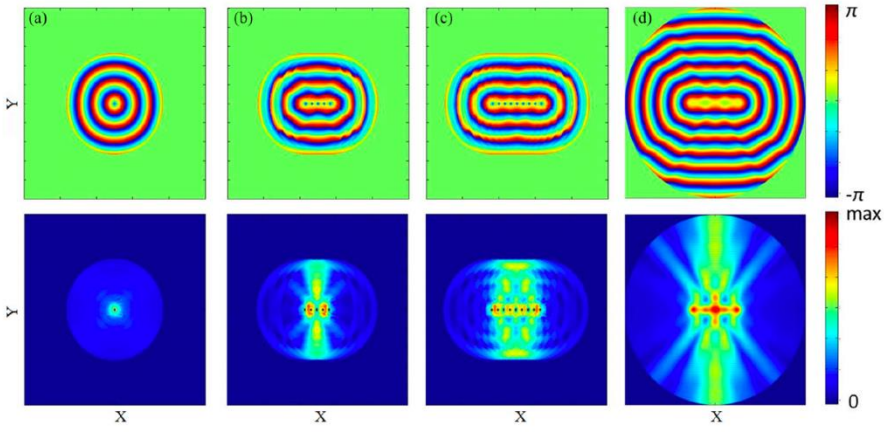

Figure 4.3. Phase (upper panel) and amplitude (lower panel) of the scattered wave for (a) a single pillar at a compressional mode; (b) adding five single sources with a inter distance of 200 μm numerically; (c) similar as (b) but for nine single sources; (d) one real line of nine pillars inter distance as 200 μm. This figure is reprodcued from Ref. [90].

B. Properties of a metaline of pillars

1. Metasurface by phase engineering

Thanks to the Huygens-Fresnel principle as demonstrated in the previous section, the properties of a line of pillars is discussed in this subsection. We first consider the pillar as in Fig. 4.1b, with an internal distance of 200 μm. The transmission curve and complex phase diagram of a scattered wave normalized to an incident wave are calculated in Fig. 4.4a. One can see that three transmission dips occur corresponding to the first and second bending modes and the compressional mode, as marked in blue, black, and red, respectively. The three intrinsic modes will produce ellipses in the complex phase diagram. In this complex plot, a point locates at the +*x*, +*y*, -*x* and -*y* axes–meaning that the phase of the scattered wave is 0, π/2, π/- π, and - π /2, respectively, with respect to the incident wave. The three ellipses are symmetric with respect to -*x* axis, but cut the -*x* axis at different positions as *x*=-0.92, *x*=-0.59 and *x*=-0.96, respectively. As the full wave field is a sum of incident and scattered waves, the transmission amplitudes are consequently 0.08, 0.41 and 0.04, respectively, after destructive interference between the incident and the scattered waves.

The second bending mode and the compressional mode can be easily tuned to be superposed by diameter as already shown in Fig.4.1c. The overlapped mode characterization is displayed in Fig.4.4b as black and red solid lines. Although the transmission curve still shows a dip for this superposed mode, the amplitude is much higher than their individual ones, being 0.57. From the complex phase diagram, the two ellipses merge into a bigger new ellipse that cuts the -*x* axis at x=-1.57, explaining the amplitude of transmission dip after destructive interference. It should be noted that the phase of the transmitted wave at the superposed frequency is out-of-phase with respect to the incident wave, which is different from separated modes. The out-of-phase property indicates that a line of pillars is possible to any possible

phase within the range [-π, π], thus the generalized Snell's law can be applied to efficiently design metasurface wavefront functions.

According to the generalized Snell's law, the phase response can be locally designed nonlinearly along an interface between the two media, as any possible distribution profile according to the wavefront function's requirement. In practice, the thickness of the "interface" is much smaller than the working wavelength, thus a "metasurface" is named. As an example, Fig.4c shows a line of pillars whose local phase responses are designed according to a focusing function. The pillared metasurface will transfer the incident plane wave into focusing at the other side, being a promising direction to manipulate Lamb waves for compact applications, as the same function for bulk phononic crystals and metamaterials requires the thickness size to be much larger than the working wavelength.

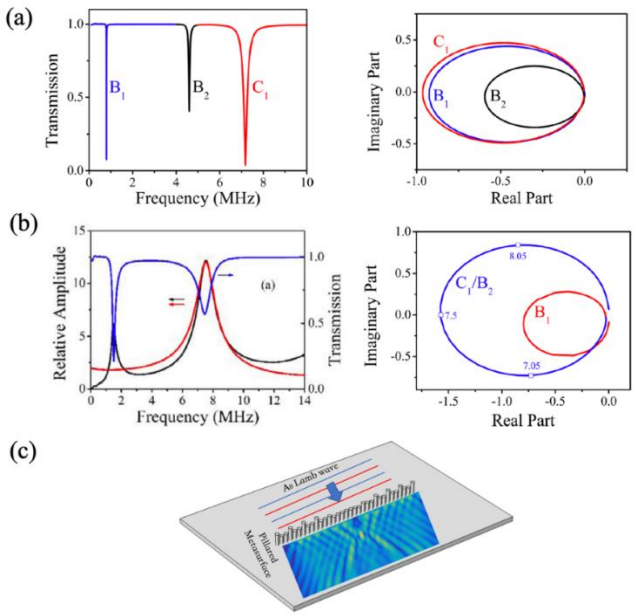

Figure 4.4. (a) The left panel displays a transmission curve for a line of pillars whose three intrinsic modes are separate. The right panel shows a complex phase diagram of the transmission exhibiting three ellipses corresponding to the three modes. (b) The left panel shows the transmission and mode characterization curves for a line of pillars whose second bending and compressional modes are superposed; the right panel provides the complex phase diagram of the transmission exhibiting the superposed ellipse being a bigger size. (c) Illustration of the focusing effect by a line of different pillars whose phase is designed based on generalized Snell's law. This figure partially includes results from Ref. [90].

2. Fano resonance and EIT/ATS

In the previous section, the periodic spacing of the considered metasurface unit is 200 μm with a pillar diameter of 50 μm. Here, we first consider two pillars in the unit cell, which means the interval between two neighboring pillars is 100 μm. Fano resonance appears in this system, originating from the coupling between the neighboring pillars which results in an asymmetric profile in the transmission curve. If we fix one pillar's height as h=245 μm and change the other pillar's height h_j/h, the evolution of the two dips and the peak in transmission curve is exhibited in Fig.4.5a, where the red solid line

presents the resonant frequency of the fixed pillar and the green solid line presents the resonant frequency of the varying pillar. The corresponding quality factors are shown in the right panel of Fig.4.5a. When h_j approaches h, the two transmission dips avoid crossing each other, and the first dip and the peak get closer to each other with significantly increasing quality factors, about 3 orders of magnitude higher. In the vicinity of $h_j=h$, the quality factor of the Fano resonance tends to be infinity, rendering a "trapped mode".

Then, we consider two lines of pillars to study the interaction of two metasurfaces. When the distance between the two identical lines is 230 μm, Fabry-Pérot resonance appears whose frequency equals to that of pillars, as the wavelength in the plate is the double of the distance. The transmission of such three resonators is displayed as a blue solid line in Fig. 4.5b, showing only one dip that reveals the role of Fabry-Pérot resonance as a bound state in the continuum (BIC). If we asymmetrically adjust the heights of two pillars, the Fabry-Pérot resonance becomes visible and results in a sharp transmission peak from the original dip, as shown in other solid lines in Fig.4.5b. The frequencies of the two dips follow the resonant frequencies of the two pillars and the peak is induced by Fano interference from Fabry-Pérot resonance, being an acoustic analogue of electromagnetically induced transparency (EIT). When the distance between the two identical lines is 100 μm, Fabry-Pérot resonance is outside of the studied frequency domain, so that no Fano interference will be involved. When the two pillars are identical, $h_1=h_2=245$μm, two transmission dips (black solid line in Fig.4.5c) are observed whose frequencies are different from the individual resonant frequencies (red or blue circle-dotted line). This is a splitting effect by strong coupling between the two resonant pillars, resulting in an acoustic analogue of Autler-Townes splitting (ATS). If h_2 deviates from 245 μm, the coupling effect between the two pillars weakens and finally disappears. As it is seen, the two dips exactly meet the individual resonances for $h_2=220$ μm or $h_2=270$ μm in Fig.4.5c, not as ATS any more.

The transparent windows in the transmission curves for EIT and ATS are usually similar and difficult in discernment. Many efforts are paid to realize differences between them using proposed numerical methods in classic systems such as optomechanics, micro-resonators, photonic crystals, plasmonics, among others. In our studies, we proposed a fundamental discerning method by utilizing their physical mechanisms. The principle of the method is also extended to an acoustic system with Helmholtz resonators grafted to a tube which is supported by analytical, numerical, and experimental validations as well as the common Akaike Information Criterion (AIC) method[160].

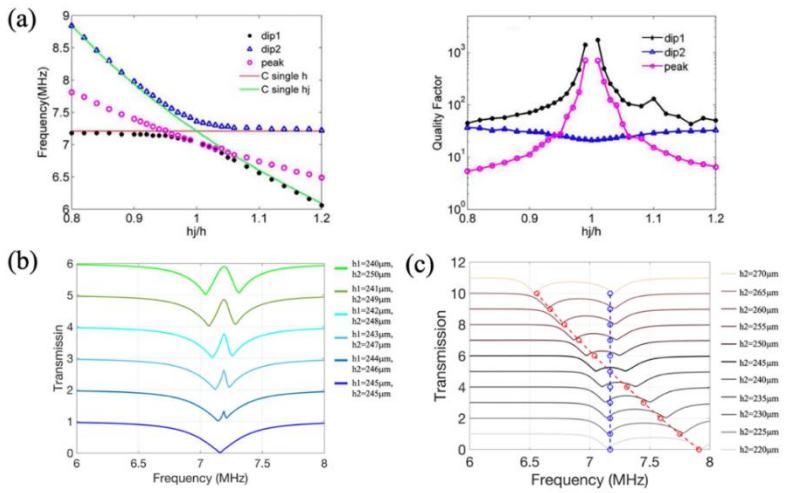

Figure 4.5. Pillared metasurface with two pillars in one unit whose lattice constant is 200 μm (interval is 100 μm): (a) Evolution of dips and peak of Fano transmission profile by changing the height of pillar *j* while fixing the height of the other pillar as 245 μm; (b) the corresponding quality factors in (a). Pillared metasurface with two lines of pillars: (c) acoustic analogue of EIT with Fano interference by asymmetrically adjusting the two pillar heights while keeping the two-line distance as 230 μm; (d) acoustic analogue of ATS without Fano interference where only one height is changed while keeping the two-line distance as 100 μm. This figure is reproduced from Ref. [91] and Ref. [99].

3. Metagrating by diffraction engineering

A metasurface requires a gradient profile (e.g., phase response) along the surface to achieve wavefront functions. Another way is to design a grating which can channel a wave at a desired diffraction order while eliminating other orders. The idea was firstly realized by Torrent [220] with inverse design for an acoustic wave and applied to an acoustic carpet cloak by Jin et al. [157]. Afterwards, it was extended to a flexural wave in a thin plate with a pillar-like resonator [221].

Despite the complex vibrations of a actualpillar configuration, it can be simplified as a mass resonator connected to a plate with a spring. Implementing the Kirchhoff plate equation with Newton's second law and Hook's law, the equation of motion can be solved for the multiple scattering problem with a given incident wave for periodically arranged pillar scatterers. In other words, if the positions and physical parameters are known, the reflective and refractive properties can be consequently acquired. For the wave function considered, reflection and transmition coefficients can be first controlled through grating design, then the physical properties of pillar scatterers may then be inversely derived.

In Fig.4.6a, a cluster is shown that consists of three different scatterers with a given position pattern that is periodically arranged as a line on a thin plate. For a given frequency and incident angle, the object of wave function is to keep the n=-1 refractive diffraction order while eliminating all other diffraction orders. In order to obtain a unique solution, the position pattern of the cluster is linear as shown in Fig.4.6b. The impedance of the scatterers can be finally solved. The field of the diffraction of a plane wave by infinite grating is computed and displayed in Fig.4.6b, showing the exact n=-1 refractive

diffraction effect. In Fig.4.6c, the full wave distribution for a finite grating of 30 clusters is presented with the same diffraction effect. It should be noted that clusters of different diffraction effects can also be composed to a grating to design focusing lenses, cloaks, and so on.

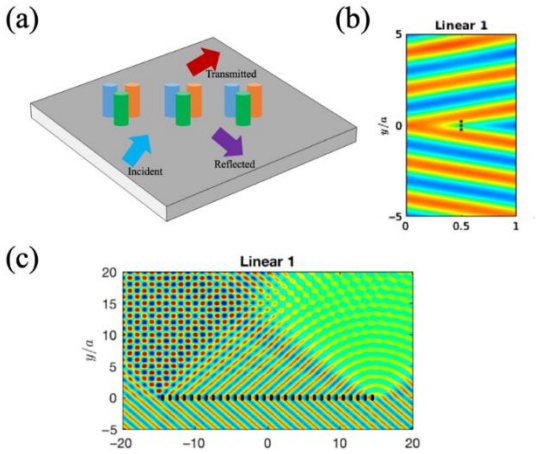

Figure 4.6. Pillared metagrating. (a) Each unit of grating consists of 3 pillars. For an incident flexural wave, the grating will reflect and refract with different diffraction modes. (b) Full wave distribution of grating unit with an incident angle and only the *n*=-1 refracted diffracted mode. (c) Full wave field function as in (b) but for a finite number of 30 units. This figure is reproduced from Ref. [221].

Chapter 5 Topological pillared phononic plate

A. Introduction

Phononic crystal plates consisting of periodic pillars deposited on a thin plate are able to exhibit topologically protected edge states, a conept that originates from electronic systems. An analytical theory was developed for a pillared phononic plate in terms of flexural waves, by considering the pillar as a point-like resonator connected to the plate by a spring for out-of-plane vibrations [222]. For a honeycomb lattice of such resonators, Torrent et al. [145] demonstrated Dirac cones due to the lattice symmetry as an elastic analog of graphene and found analytical expressions for both Dirac frequency and velocity. The Dirac cone is protected by the inversion symmetry and the time-reversal symmetry. By breaking either the inversion symmetry within the honeycomb unit cell or the time-reversal symmetry, the degeneracy at the Dirac point is lifted giving rise to the opening of a gap. The upper and lower bands surrounding the gap have non-zero Chern number (topological invariant), which reveals non-trivial property for the gap and allows the existence of topologically protected edge states at the interface between two topologically different crystals. The mechanical analogs of topologically protected edge states have been widely studied, including analogues with the quantum Hall, quantum spin Hall, and quantum valley Hall effects. Detailed information on the topological principles in acoustic systems is found in recent reviews [223, 224]. To be noted, topological Fano resonance can be generated by combining both topological bright and dark modes in a pillared beam[225].

B. Topologically protected states

Based on analytical model of a pillar-like point resonators on a plate, Pal et al. [146] introduced topologically protected edge states by breaking inversion symmetry, which was further experimentally demonstrated will actual pillar configuration [149], with the geometry shown in Fig.5.1a. The double-sided hexagon was shown to possess a Dirac cone at the K/K' point in the Brillouin zone when the mass of the pillars are identical. If the mirror symmetry of the unit cell is broken by introducing different masses (through changing the height of the pillars, for example), the Dirac cone degeneracy is lifted and a non-trivial band gap is formed with valley Chern number of an upper or lower band equal to 1/2 or -1/2 at the K or K' points, which shows opposite polarizations of their eigenmodes ; this illustrates an analogy with the quantum valley Hall effect. The symmetry-broken unit can be further taken to build a finite stripe with an interface separating two lattices. The dispersion of the stripe supports an interface band in the bulk non-trivial band gap, whose eigenmodes are localized at the interface units, as a topologically protected edge state.

Chaunsali et al. [147, 226] demonstrated the pseudospin Hall effect for flexural waves with local resonators as shown in Fig.5.1b. The arrangement of six bolt-like pillars in a hexagon lattice has different sizes, shrunken or expanded. Since the bigger unit cell with six resonators are chosen instead of the unit cell with two resonators, a double Dirac cone at the Γ point is possible to be constructed by adjusting the proper radius and zone-folding of bands. It should be noted that the double Dirac cone is also possible to occur at the K/K' point for a patterned plate with proper parameters [227, 228]. A Bragg band gap is formed from the degeneracy of the double Dirac cone when the six resonators expand due to the change in translational periodicity. However, a nontrivial band gap is formed when they shrink and the degenerated bands have a nonzero spin Chern number. Therefore, the emergence of topological edge modes appears at the interface which separates trivial and non-trivial lattices. This bolt-resonator configuration was recently taken to construct a Kekule distorted mechanical graphene and a topologically bound state was demonstrated [229]. A mechanical analogue of Majorana bound states is also demonstrated by creating a Kekule distortion vortex onn a bolt-resonator honeycomb superlattice[230]. Very recently, double-side pillared phononic plate whose plate is drilled with patterned holes was shown to emulate the quantum spin Hall and the quantum valley Hall effects with different Lamb modes [231, 232].

Similar to the geometry in Fig.1a, the dispersion of a large unit cell containing six resonators (marked in green hexagon in Fig.5.1c) can exhibit a double Dirac cone at the Γ point due to band folding. The lattice can be expanded or shrunken by tuning the red and blue connecting bars, which degenerates the double Dirac cone and forms a band gap. A hexagon-shaped sample with shrunken unit cells as shown in Fig.5.1c displays gapped edge modes, topological corner modes, and trivial corner modes in

the degenerated band gap. When defects are applied to the red-dotted boxes, trivial corner modes will shift frequencies while the edge and topological corner modes are robust [233].

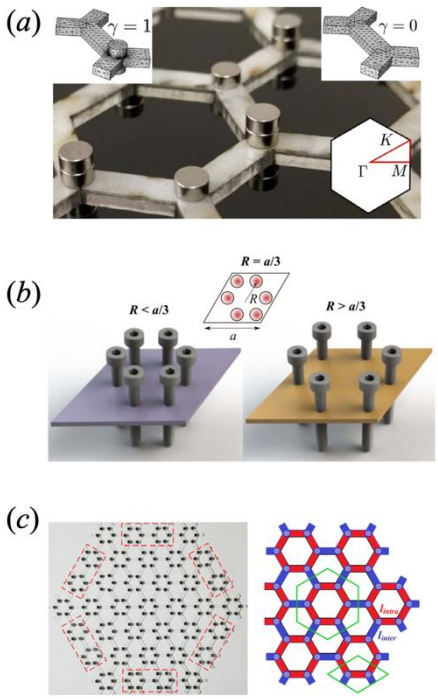

Figure 5.1. A structure exhibiting the acoustic analogue of the quantum valley Hall effect for flexural waves by breaking inversion symmetry in the unit cell. This figure is reproduced from Ref. [149] (b) A structure exhibiting the acoustic analogue of the pseudospin Hall effect for flexural waves by shrinking the six-resonator unit size. This figure is reproduced from Ref. [226] (c) Elastic higher-order topological insulator with topologically protected corner states by a shrunken unit cell with six resonators. This figure is reproduced from Ref. [233].

C. Robustness of topologically protected edge states

Topology is an effective tool to describe properties of wavefunctions over a band and it may be utilized to produce waveguides that are robust against certain perturbations [224]. It is widely demonstrated that a topologically protected edge state is immune to the back-scattering effect thus enabling it to propagate through a sharp corner without energy loss. With respect to the existence of defects, the topologically protected edge state is robust to such local perturbation without any influence on wave transport. This is illustrated in Fig. 5.2a where a point defect is added along a zig-zag topologically protected edge state.

If local perturbations are strong enough so that the non-trivial band gap is closed or the edge band is disturbed, the robustness of topologically protected edge states will consequently fail to preserve edge propagations. In Fig.5.2b, we minimize the size of the bulk structures surrounding the zigzag interface. When there is only one hexagon surrounding the interface, more leaky waves are observed especially at the sharp corners. The wave amplitude decreases significantly after two sharp corners, meanwhile the zigzag interface propagating is still preserved. It is further found that once the surrounding bulk media

for the sharp corner continues to be minimized, the edge wave cannot even pass the first corner and the zigzag interface propagation disappears. It is suggested that two or more hexagons should be considered for the size of the bulk structures in order to preserve the non-trivial band gap [233].

In Fig. 5.2c, we discuss the transmission along a linear edge when all the pillars along the interface are subject to height disorder. A disorder degree of *x*% means that the heights of all the pillars at the interface can randomly be increased or decreased within the range of *x*%. From the left panel of Fig. 5.2c, it is noticed that the transmission through the topologically protected interface state is not affected for a wide range of height disorder and the transmission remains close to unity up to a disorder degree of about 40%. However, an abrupt drop occurs in transmission when the height disorder increases from 40% to 50%, then the transmission oscillates around 0.4 for a higher degree of disorder. The sudden drop behaves like a transition threshold in the propagating states that can be seen from the wave fields at the right panel of Fig. 5.2c. The transmission is close to unity for values of height disorder of 8.3% and 25%. For higher disorders of 42% and 66%, it is seen that the incident wave hardly enters the interface as the interface mode disappears. As such, the low transmission value is from the wave reflecting effect at the entrance [233].

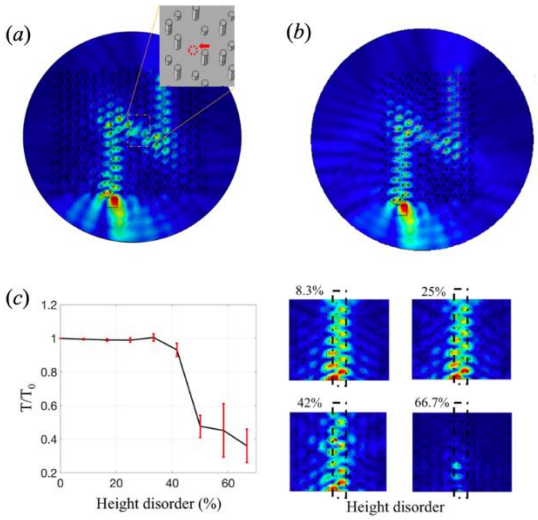

Figure 5.2. (a) Topologically protected zigzag interface state against a defect. (b) The same zigzag state against a minimized bulk size with only one hexagon unit beside the interface. (c) In the left panel, transmission property versus height disorder level of the pillars of the interface; in the right panel, the flexural wave propagation field for four selected height disorders.This figure is adapted from Ref. [151].

6 Nanophononic metamaterials: Nanopillared membranes for thermal conductivity reduction

A. Introduction

The previous sections provide a thorough review of pillared phononic crystals, metamaterials, and metasurfaces at the “macroscale” where the phenomena of interest pertain either to acoustic or elastic waves. The length scales relevant to this class of problems are typically on the order of micrometers and

larger, reaching meters, and the frequencies range from Hertz to Megahertz, and possibly Gigahertz. The common and effective modeling framework of macrophononics lies within the continuum hypothesis.

In this section, we transition to a fundamentally different class of problems where we enter into the domain of *nanophononics*. Here, the interest is primarily in heat transfer by conduction; the length scales are in the nanometer range, and the relevant frequencies are in Terahertz–often spanning tens of Terahertz. Because of the very high frequencies and the size dependence of the underlying physics (among other factors), the modeling paradigm for nanoscale thermal transport is necessarily atomistic. This regime has been investigated within the nanoscale heat transfer community for the past few decades, primarily focusing on low-dimensional materials [234] until recently when a merge with concepts and themes from phononic crystals and metamaterials began taking shape attracting a growth in cross-disciplinary research.

1. Nanophononic crystals (NPC)

The notion of a phononic crystal at the nanoscale, i.e., nanophononic crystal (NPC), was first explored in the context of 1D layered crystals [235, 236] and shortly afterwards was advanced to two [237-240] and three dimensions [241-243]; see, for example, the Fig. 6.1a and Fig. 6.1b schematics of a uniform membrane and a membrane in the form of a nanophononic crystal, respectively. While the interest in macroscopic phononic crystals is usually dominated by the presence of band gaps, at the nanoscale (when a 3D crystal is modeled atomistically) a complete band gap is unlikely to emerge [242]. The interest, instead, is primarily in the flattening of the dispersion curves that arise due to Bragg scattering. Flatter dispersion curves have lower group velocities and this, in turn, leads to a reduction in the thermal conductivity, *k*. This mapping between the group velocities and the total lattice thermal conductivity (i.e., not considering thermal transport by electrons) is best understood by examining the integrand in the Boltzmann transport equation (BTE) following the single-mode-relaxation time (SMRT) approximation [244, 245], For a membrane-like material, this equation is

$$k = \frac{1}{V}\frac{A_c}{4\pi}\sum_m \int_\kappa C(\kappa, m) v_g^2(\kappa, m)\tau(\kappa, m)\kappa d\kappa, \tag{6.1}$$

where A_c is the unit-cell base, V is total volume of the system, C is the specific heat, and v_g, and τ denote the group velocity and the scattering time constant (lifetime), respectively. The integration is over all phonon wave numbers for branch number m and the summation is over all the phonon branches. The division by V stems from the fact that k is an intrinsic property [170]. From Eq. (6.1), it is seen that that a prediction of k is constructed by summing over all phonon modes in the spectrum and integrating along the direction of interest over the Brillouin zone. The thermal conductivity is therefore dependent on the phonon band structure, which in turn is affected by the unit-cell structure and lattice symmetry. The integrand consists of a product of the specific heat, the group velocity squared, and the lifetime–all

quantities defined for each mode of phonon motion as determined by the dispersion diagram. An NPC membrane consisting of a host semiconducting material, silicon for example, and a periodic array of holes or inclusions may exhibit a lower in-plane thermal conductivity compared to a corresponding uniform membrane due to the dispersion curves flattening. A practical disadvantage, however, is that the surfaces of the periodic features, e.g., the holes or inclusions, must be considerably smooth to preserve the phase information required for the Bragg effects to take place−especially when the features are of relatively large sizes compared to the phonon wavelengths [240, 246, 247]. At a more fundamental level, the degree and intensity of group-velocity reductions are limited to what the available Bragg interference patterns can provide, which is somewhat modest leading usually to an order of magnitude reduction at most [240]. One possibility is to allow the boundaries or interfaces of the holes or inclusions to be rough, which would induce mostly boundary scattering, possibly in combination with some level of Bragg scattering. In this scenario, one may increase the size and concentration of the holes or inclusions to the point where the phonon motion gets inhibited excessively by the scattering component. Here, the effective thermal conductivity in the overall medium may be reduced significantly, however at the expense of having extremely small/thin segments of the host material, e.g., see Ref. [243]. This approach would therefore not be favorable if the interest is to reduce the thermal conductivity without negatively impacting the electrical conductivity–as needed in thermoelectrics [248-250].

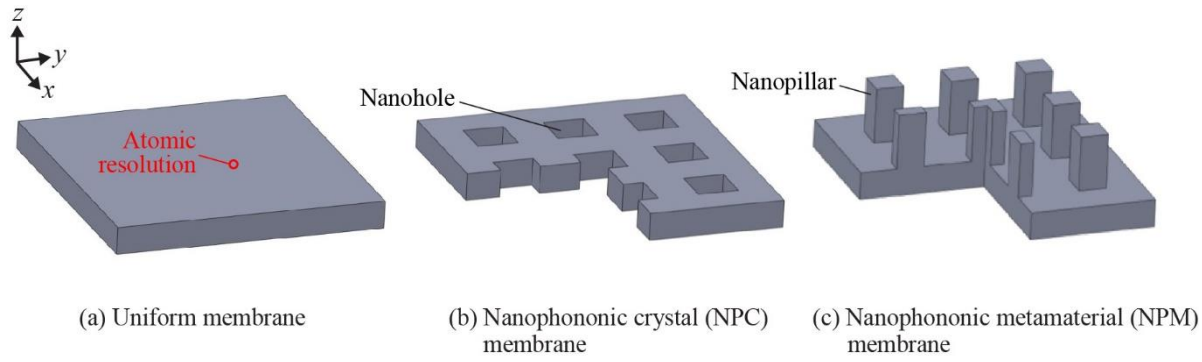

Figure 6.1: Three silicon membrane configurations: (a) Uniform, (b) nanophononic crystal, and (c) nanophononic metamaterial.

2. Nanophononic metamaterials (NPM)

The notion of a metamaterial for the reduction of the thermal conductivity by local resonances has been introduced by Hussein and co-workers, first in 2014 [166, 167] and followed by a series of systematic investigations [168, 169, 171, 251]. The underlying concept in this new class of metamaterials, termed *nanophononic metamaterial* (NPM), is to intrinsically introduce nanoresonating substructures to a host crystalline material, typically a semiconductor, such that a very large number of local resonances emerge and contribute through several mechanisms to the reduction of the overall lattice thermal conductivity. The local resonances couple with heat-carrying phonon modes of the host medium. This atomic-scale coupling mechanism gives rise to a resonance hybridization between pairs of the wavenumber-independent vibration modes of the local substructure (vibrons) and wavenumber-

dependent wave modes of the host medium (phonons). Vibron-phonon coupling creates curve flattening and, consequently, reductions in the group velocities and hence the overall thermal conductivity. Stronger couplings produce sharper curve flattenings and larger reductions in the group velocities. The local resonances also confine the atomic modal motion within the nanoresonators, which in turn causes further reduction in the thermal conductivity. In addition, the phonon lifetimes drop due to changes in the scattering environment, including both phonon-phonon scattering and boundary scattering. The power of this approach stems from the fact that the local resonances may be tuned by design to be numerous and span the entire phonon spectrum of the host material, and, moreover, conform in their density-of-states (DOS) distribution to the host material phonons DOS (see Sections 6.2.1 and 6.4), thus maximizing the three effects mentioned above and increasing the thermal conductivity reduction. In the limit, the number of local resonances is three times the number of atoms in a unit nanoresonator.

It is worth noting the fundamental contrast with conventional metamaterials where the aim is to generate subwavelength band gaps or create negative long-wave effective properties as is the case for locally resonant electromagnetic [252, 253], acoustic [16], and elastic [19, 20, 254] metamaterials (Sections 2-5 focus on conventional metamaterials). The target in NPM design is to optimally enable the thermal conductivity reduction mechanisms: group velocities reduction, energy localization, and lifetimes reduction. Another practical goal is to do so without affecting the electrical properties in order to effectively increase the thermoelectric energy conversion figure of merit ZT [170, 171].

The NPM configuration proposed in Refs. [166-171] consists of an array of silicon nanopillars distributed on the surface(s) of a freestanding silicon membrane with no interior scatterers; see illustration in Fig. 6.1c. Here the nanopillars act as the resonating substructures. Since the nanopillars are located outside the main body of the membrane, which serves as the transport zone, the electronic band structure is only mildly affected and electron scattering occurs only near the membrane surfaces and not in the interior. Compared to all common phonon scattering-based approaches (where the scatterers are in the main body of the transport medium), this NPM configuration therefore provides the unique advantage of practically decoupling the lattice thermal conductivity from the Seebeck coefficient and the electrical conductivity−which is essential to creating significant increases in ZT. In addition, an NPM in the form of a nanopillared membrane naturally exhibits dimensionality reduction (compared to the bulk form). Therefore, the powerful rewards of resonance-induced thermal conductivity reduction are gained over and above the benefits of phonon confinement [255] and surface roughness[256] (as well as the benefits to the electrical properties [257]). Equation (6.1) applies to an NPM as it does for a NPC, keeping in consideration that for an nanopillared NPM the volume V includes both the base membrane and nanopillar portions.

Since the publication of Ref. [166] in 2014, several investigations of NPMs by other groups followed. Several papers examined computationally a variety of NPM configurations for thermal conductivity reduction. Using atomic-level modeling, Wei et al. explored the effects of varying the nanopillars spacing and dimensions in silicon nanopillared membranes and analyzed mode localization [258]. Xiong

et al. studied silicon NPMs in the form of rods/wires with branching structures and explored the effects of alloying and temperature [259]. Another investigation of rod/wire-based NPMs was conducted by Ma et al.[260]. Ma et al. studied local resonant effects in 3D silicon nanowire cages [261], and Zhu et al. [262] considered bulk silicon with internal amorphous regions acting as the nanoresonators (see Ref. [263] for a survey of potential configurations using atomically-disordered inclusions). Thermal conductivity reduction in branched nanoribbon materials composed of molybdenum disulfide (MoS_2) was reported by Liu et al. [264]. Giri and Hopkins [265] and Yang and coworkers [266] extended the NPM theme to carbon nanotubes and graphene sheets, respectively. Another intriguing NPM architecture is based on a graphene sheet decorated with branching fullerene nanoresonators[267]. Examination of the impact of nanopillars on the heat capacity was investigated by Iskander et al. using both theory and experiments [268]. The NPM concept has also been employed for thermal rectification, in Indium Arsenic (InAs) nanowires [269, 270], nanopillared graphene structures [271], and graphene nanoribbons [272]. A range of possible NPM geometric configurations, including 1D, 2D, and 3D systems is given in Ref. [167], noting that one of the unique features of NPMs is that they may be realized using a wide range of materials for both the host medium and the nanoresonator medium. Other studies examined NPMs using finite-element (FE) analysis as often done for macroscale acoustic or elastic metamaterials [111, 172, 273-275]. While linear continuous modeling may provide some insights, atomistic modeling is necessary for accurate qualitative and quantitative capturing of the effects of the three key NPM mechanisms responsible for the thermal conductivity reduction. This can be seen in the inherent dependence of the thermal conductivity on (1) the number, range, and detailed characteristics of the dispersion branches in the phonon band structure, as evidenced in Eq. (6.1) and the intricate band structure of Figs. 6.3b and 6.4 (noting that these figures only show a small portion of the spectrum), and (2) the anharmonic interatomic interactions. A study of the convergence of the FE-based thermal conductivity reduction predictions to those obtained by atomic modeling is given in the Supplementary Material accompanying Ref. [166]. The importance of atomic resolution and nonlinear effects is further reinforced by observation of the profound size and geometry dependence of the underlying physics of nanoscale thermal transport in NPMs [170].

3. NPM versus NPC

Compared to NPCs, NPMs are not dependent on periodicity and phased travelling wave interferences, and are therefore more robust to disorder in the arrangement of the nanoresonators and to surface roughness. Furthermore, the intensity of group-velocity reductions, mode localization, and controlled lifetime reductions may be continuously enhanced by simply increasing the size and packing efficiency of the nanoresonators[169, 258]. Future research may consider a hybrid between an NPC with holes and an NPM with nanopillars, that is, a nanoscale version of the trampoline configuration of Section 3.A.1. This way, additional Bragg scattering from the holes and relatively lower resonance frequencies from the “more compliant” nanopillars may be realized. As long as there is enough spacing between the holes not to impede the electron transport, it is conceivable that this mixed hole-nanopillar

configuration would harness more thermoelectric energy conversion compared to having only nanopillars.

B. Lattice dynamics and vibron-phonon couplings

In an NPM, the substructure resonances–denoted as vibrons–are distinct from phonons by virtue of their wavenumber-independent standing-wave character. The frequency spectrum of vibrons may be designed to couple with heat-carrying wavenumber-dependent phonon modes belonging to all or most of the dispersion branches across the full spectrum of the host medium. As described in Section 6.1, this atomic-scale coupling mechanism gives rise to a resonance hybridization between pairs of vibrons and phonons. This phenomenon may be demonstrated theoretically using lattice dynamics (LD) calculations on a unit cell of the NPM.

Here we review the wave propagation characteristics of two freestanding NPM configurations: membrane with nanopillars (i) on one surface (single nanopillared) and (ii) on each of the surfaces (double nanopillared). In all cases, both base membrane and nanopillar(s) are made of defect-free single-crystal silicon. Figure 6.2 displays the unit cells of these two configurations as well as the structure of a conventional cell (CC) and a unit cell of a corresponding uniform (unpillared) membrane. The geometry of a membrane with nanopillars on each surface is represented as $b\times b\times d+c\times c\times h_T+c\times c\times h_B$ nm (which may be converted to CC by dividing each dimension by the atomic spacing a). The last two terms represent the size of the top and bottom nanopillars, respectively, and these are dropped when representing an unpillared membrane. If only a single nanopillar is included in the unit cell, the nanopillar height is denoted simply by h. All geometric parameters are pictorially defined in Fig. 6.2. Unless explicitly specified, all the analyses presented in this section are at a room temperature of T = 300 K, and the Stillinger-Weber empirical potential is used in all models to represent the interatomic interactions[276]. Also, to keep our focus on the core effects of local resonances, we only consider defect-free crystals.

Figure 6.3 shows a portion of the dispersion curves for an NPM in the form of a nanopillared membrane and, for comparison, the corresponding dispersion curves for an NPC in the form of a membrane with holes. The NPC has the same membrane thickness as the NPM and the cross-sectional size of the holes is chosen to be equal to that of the nanopillar. Also, for comparison, dispersion curves for a uniform membrane with the same thickness are shown. Compared to the uniform membrane, the NPC curves appear to be flatter especially at the righthand-side edge of the Brillouin zone–this is a manifestation of Bragg scattering. In contrast to the NPC, the NPM features the vibron local resonances, appearing as horizontal lines that veer off with the underlying phonon dispersion curves of the membrane. Because the nanopillars are laid out periodically, curve flattening at the edge of the Brillouin zone due to Bragg scattering is also observed. The reader is referred to Refs. [2-4, 6, 17, 18] for more discussion on the difference between a phononic crystal and a locally resonant metamaterial in general, regardless of scale.

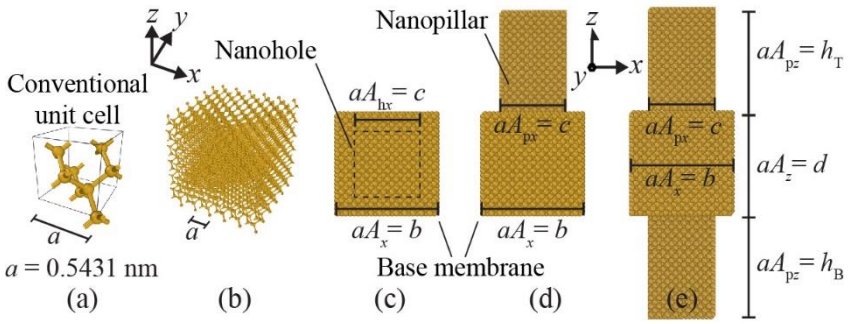

Figure 6.2: (a) Conventional 8-atom unit cell for silicon and unit cells for a (b) uniform membrane, (c) single-pillared NPM, and (d) double-pillared NPM. In (b), (c) and (d), the unit cell is repeated in the x and y directions, and the top and bottom surfaces are free. Heat transfer takes place in the in-plane directions along a uniform membrane and, correspondingly, along the membrane portion of an NPM. Figure adapted from Ref.[170].

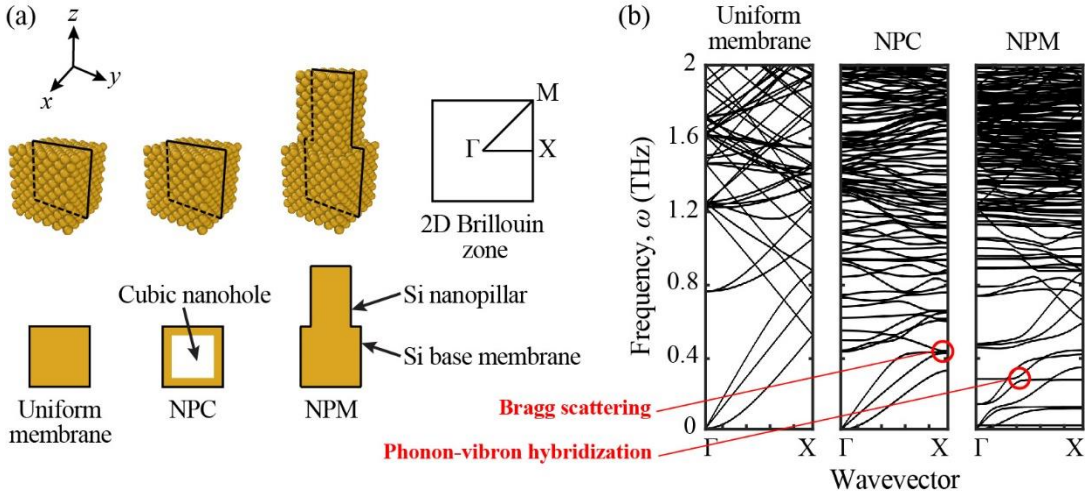

Figure 6.3: (a) Schematics and (b) phonon band structure for a uniform membrane, a nanophononic crystal membrane, and a nanophononic metamaterial membrane. For the NPC, the size of the unit cell is 3.26×3.26×3.26 and the size of the centrally located hole is 2.17×2.17×2.17 nm. For the NPM, the size of the base membrane is 3.26×3.26×3.26 and the size of the centrally located nanopillar is 2.17×2.17×3.26 nm. The dimensions of the uniform membrane unit cell are 3.26×3.26×3.26 nm.

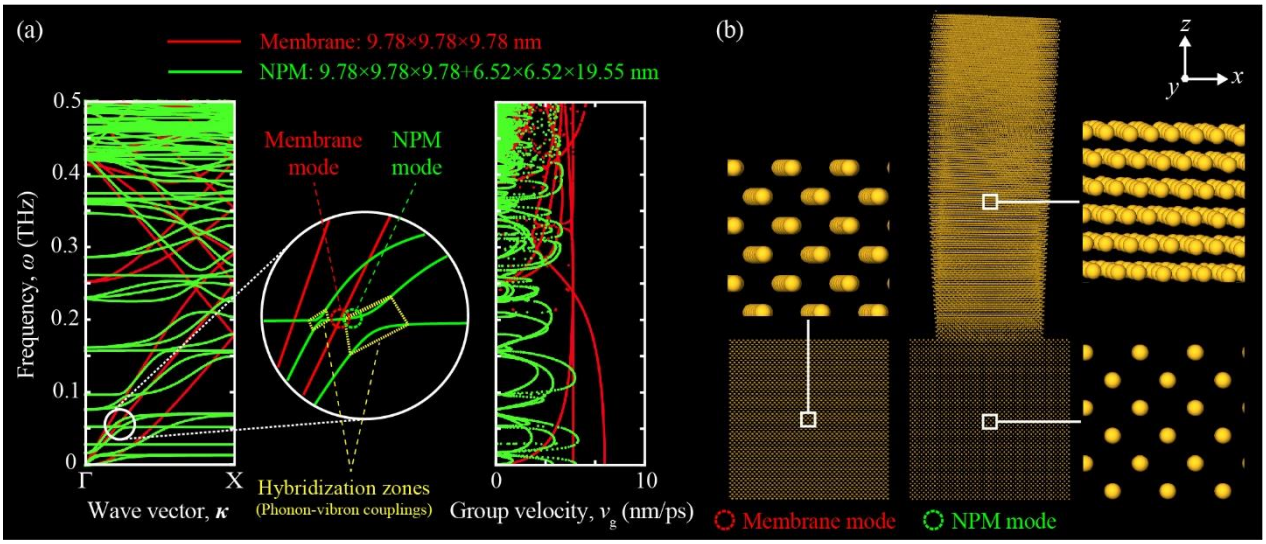

Figure 6.4: Illustration of local resonances and the resonance hybridization phenomenon from a lattice dynamics perspective. (a) Phonon band structure and group velocity distribution of a silicon membrane with (green) or without (red) silicon nanopillars erected on one surface. (b) Uniform membrane atomic displacements for a heat carrying phonon mode in the acoustic regime contrasted to NPM atomic displacements of the same mode upon resonance hybridization. Significant motion within the uniform membrane is seen. In contrast, the atomic displacements of the NPM hybridized mode reveals localized nanopillar motion and almost no motion in the base membrane portion. In (a), a zoom-in is provided for two hybridization zones including the one illustrated in (b). A magnification factor of 2000 is applied to the atomic displacements in the mode-shape images. Figure adapted from Ref. [170].

Figure 6.4 provides a more in-depth demonstration of the resonance hybridization phenomenon, as manifested in the phonon band structure, group-velocity distributions, and associated mode shapes. For this purpose, we consider an 9.78×9.78×9.78+6.52×6.52×19.55 nm NPM unit cell (consisting of 88128 atoms). To economically obtain the phonon band structure for such a large unit cell, we used the reduced Bloch mode expansion (RBME) technique [277] to solve the corresponding eigenvalue problem over the 0-0.5 THz range. The effects of the phonon-vibron mode couplings phenomenon are clearly displayed in both the dispersion diagram and the corresponding group velocities diagram, as shown in Fig. 6.4a. The profound reduction in the group velocities is evident across the entire frequency range plotted (and the same effect extends throughout the entire spectrum). As noted earlier, reduction in phonon group velocities directly implies reduction in the thermal conductivity. Figure 6.4b focuses on a particular mode in the band structure and displays the unit cell mode shape without and with resonance hybridization. The confinement of the atomic motion solely in the nanopillar region represents a case of extreme localization of energy. This localization phenomenon in itself also contributes to the reduction in the thermal conductivity.

Impact of mode localizaiton on the thermal conductivity As noted earlier, while the nanopillar adds modes (vibrons) to the total unit-cell system, most of these modes are severely localized (i.e., exhibiting zero group velocity in the band structure). Therefore, even though these modes add to the number of terms summed in Eq. (1), the actual additional quantities that are summed are not significant. Given that

the entire integration is finally divided by the total unit-cell volume, the net effect on the thermal conductivity is that it decreases. This summarizes the cause of thermal conductivity reduction by atomic-scale mode localization.

1. Comformity of phonon and vibron density of states

As described earlier, the coupling between phonons and vibrons is the key enabling factor for the thermal conductivity reduction mechanisms in an NPM. The phonon motion is confined to the in-plane directions within the base membrane and the vibron motion is limited primarily to the domain of each nanopillar. At each phonon-vibron coupling, the phonon group velocities decrease, a pathway opens up for localization, and the phonon-phonon scattering increases. The more we have of these couplings across the full spectrum, the stronger the net reduction in the thermal conductivity. In Fig. 6.5, we examine how the overall size of the nanopillar affects the phonon and vibron density of states (DOS) distributions, collectively (i.e., when considering the integrated nanopillared membrane unit cell), and separately (i.e., when considering isolated membrane and nanopillar components). For the collective DOS picture, one can observe a subtle change in the DOS distribution due to the addition of a nanopillar. A more refined picture is seen from the separate DOS distributions. A key factor is the degree of phonon DOS and vibron DOS conformity, which may be quantified. For this purpose, we have introduced a metric to represent the inverse of conformity, namely, the *nonconformity factor* $\hat{R}_{\mathrm{pv}}$ [170]. This factor is defined as

$$\hat{R}_{pv} = \left\| R_{pv} - R_{pp} \right\|, \tag{6.2}$$

where R_{pv} is the cross-correlation between the separate phonon and vibron DOS, R_{pp} is the autocorrelation of the phonon DOS, and $\|.\|$ denotes the double norm. The reader may refer to Rabiner and Gold (1975)[278] for the definitions of correlation functions. The nonconformity factor varies between 0 (perfect conformity) and ∞ (no conformity). We see in Fig. 6.5 that for the same base membrane size within the unit cell, the value of the nonconformity factor is significantly lower (i.e., the level of conformity is significantly higher) when the size (width and height) of the nanopillars is increased for a given base-membrane thickness. This characteristic of the phonon-vibron conformity provides an opportunity for an up-scaling design pathway that creates *vibrons compensation* (Honarvar and Hussein 2018) [170]. Vibrons compensation is achieved by having the size of the nanopillar increased at a higher rate than that of the base membrane when an NPM is scaled up in size. The outcome is that not only (1) the phonon band structure gets enriched with a higher vibrons-to-phonons ratio, but also (2) the level of conformity between the phonon and vibron DOS distributions across the full spectrum, gets significantly increased. Both these factors lead to increased reduction of the thermal conductivity upon up-scaling.

2. Size limitation of NPMs

While the design process of upscaling with vibrons compensation yields improved NPM performance with size, there is a limit to the sizes that may be reached. Improvement in performance will be realized as long as the characteristic length scales of the indovidual components of an NPM, the base membrane and the nanopillars, are considerably within the span of the phonon mean free path (MFP) distribution at the temperature of interest. As the NPM feature sizes start approaching the far end of the MFP distribution, phonon–phonon scattering mechanisms will dominate and the impact of the three resonance-based effects that reduce the thermal conductivity will gradually diminish. This underscores the design necessity of preserving the NPM system within the realm of the nanoscale.

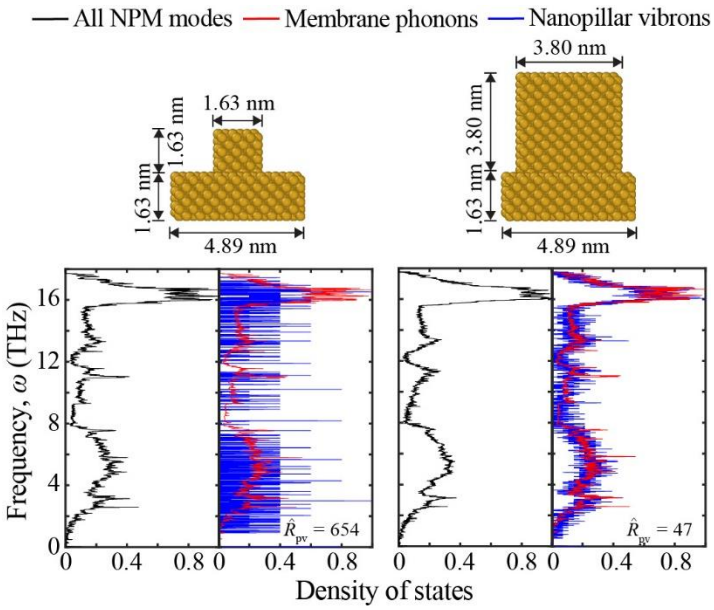

Figure 6.5: (a) Relative distributions of all modes (black), phonons in base membrnae (red) and vibrons in nanopillar (blue) DOS for an NPM configuration with a small nanopillar, i.e., small Vr (left) and a large nanopillar, i.e., large Vr (right). The quantity Vr represents the ration of the volume of the nanopillar to the volume of the base membrane. The vibron DOS are obtained by considering the nanopillar as an independent nanostructure with free boundary conditions. All quantities are normalized with respect to their maximum values. A large nanopillar with a large packing concentation leads to higher phonon-vibron conformity, which corresponds to lower values of $\hat{R}_{\mathrm{pv}}$ and a more intense resonance hybridizations effect. Figure adapted from Ref. [170].

C. Molecular dynamics and spectral energy density analysis: Evidence of localized resonances and resonance hybridizations

The NPM phonon band structures shown in Figs. 6.3(b) and 6.4 display the occurrence of local resonances, which feature as horizontal lines, and also the resonance hybridization phenomenon, which manifests as avoided crossings between these horizontal lines and the original dispersion curves of the base membrane. These phonon band structure diagrams, however, are obtained by solving an eigenvalue problem for the quasiharmonic (i.e., linear) version of the problem. In reality, the atomic interactions are anharmonic (i.e., nonlinear) at finite temperatures. The anharmonicities give rise to phonon-phonon scattering, which is noncoherent. Furthermore, the top and bottom surfaces of the unit cell are not

necessarily ideal surfaces, which implies the possibility of boundary scattering at the surfaces, including the surfaces of the nanopillars. This too is a noncoherent effect.

In order to examine whether the vibrons and the resonance-hybridization mechanism do indeed exist and unfold in the presence of these nonlinearities (and other scattering mechanisms), we resort to equilibrium MD simulations and seek to obtain the dispersion behavior (if it exists) straight from the simulations. This is done by computing the spectral energy density (SED) [279-283], which is a quantity representing effectively the space-time Fourier transform of the simulated nonlinear response. There are two SED formulations reported in the literature for phonon transport problems. In one SED formulation, referred to as Φ, the MD atom velocities are projected onto the phonon normal modes of the constituent unit cell, which are obtained separately from quasiharmonic lattice dynamics calculations. In an alternative formulation, referred to as Φ′, the SED expression requires knowledge of only the crystal unit-cell structure and does not require any *a priori* knowledge of the phonon mode eigenvectors. Both the as Φ and Φ′ formulations allow for an accurate prediction of both phonon frequencies and lifetimes [283]. In Ref. [168], we intentionally sought the Φ′ version of the technique since it enables us to establish whether or not wave behavior (including local resonances and resonance hybridization) is present in the simulations without any enforcement of wave characteristics in the calculations.

As provided in Ref. [279], the SED expression for Φ′ is a function of wave vector κ and frequency ω, and is given by

$$\Phi'(\boldsymbol{\kappa},\omega)=\frac{1}{4\pi\tau_0}\sum_{\alpha}^{3}\sum_{s}^{n}\frac{m_s}{N}\left|\sum_{l}^{N}e^{i\boldsymbol{\kappa}.\boldsymbol{r_0}\binom{l}{0}}\int_0^{\tau_0}\dot{u}_\alpha\binom{l}{s};t\,e^{-i\omega t}\,dt\right|^2, \tag{6.3}$$

where m_s is the atomic mass (which is the mass of a silicon atom for the cases considered in this section), τ_0 is the total simulation time, $\boldsymbol{r_0}$ is the equilibrium position vector of the lth unit cell, and $\dot{u}_\alpha$ is the α component of the velocity of the sth atom in the lth unit cell at time t. There is a total of $N = N_x \times N_y \times N_z$ unit cells in the simulated computational domain with n atoms per unit cell. We note that in Eq. (6.3), the phonon frequencies can only be obtained at the set of allowed wave vectors as dictated by the crystal structure. For our model, the Γ–X-path wave vectors are $\kappa_x = 2\pi j/(N_x A_x)$, j = 0 to $N_x/2$. We consider a single-nanopillared unit cell of dimensions 3.26×3.26×3.26+1.09×1.09×3.26 nm, i.e., b = 3.26 nm, c = 1.09, d = 3.26 nm, and h = 3.26 nm. For the computational domain, we set N_x = 50 and $N_y = N_z$ = 1, which gives a Γ–X wave-vector resolution of $\Delta\kappa_x$ = 0.04. Room-temperature MD simulations under NVE (constant mass, volume, and energy) ensembles were executed for this system for 2^{22} time steps and based on a time-step increment Δt = 0.5 fs. Equation (6.3) is evaluated by computing the SED field corresponding to the velocity trajectories extracted every 2^5 steps. The results from these calculations are shown in Fig. 6.6. As a reference, the phonon band structure as obtained from standard quasiharmonic LD calculations is shown in dashed red lines in Fig. 6.6(a) for a uniform membrane with the same d and in Figs. 6.6(b) and 6.6(c) for the NPM. The full SED spectrum is shown in Fig. 6.6(a) for the uniform membrane and in Fig. 6.6(b) for the NPM. Only the frequency range $0 \leq \omega \leq 1.5$ THz is shown because higher frequencies are relatively difficult to distinguish in the SED field. This

frequency range is responsible for a significant portion of the total lattice thermal conductivity [166]. We observe that the phonon dispersion emerging from the MD simulations matches very well with that obtained by the independent LD calculations, thus providing direct evidence for the existence of vibrons and phonon-vibron coupling. In particular, the first two nanopillar local resonances (present at nearly 0.2 THz) are clearly observed in the NPM SED spectrum, appearing as horizontal lines. Moreover, the interaction of these resonances with the acoustic branches of the underlying membrane are distinctly observed and follow closely the hybridization profiles featured in the LD dispersion curves. Resonance hybridizations are also clearly observed at higher frequencies in the figure where local resonance modes interact with optical dispersion branches.

Given our interest in the effects of the nanopillar resonances on the heat-carrying phonons within the base membrane, we also calculated the SED spectrum for the NPM considering only the contributions of the atoms housed in the base membrane (i.e., discounting the SED contributions of the nanopillar atoms). The outcome of this calculation is shown in Fig. 6.6(c), where we see clearly that the nanopillar resonances alter the fundamental nature of the phonon traveling waves within the membrane. These alterations in the phonon band structure result in a significant reduction in the phonon group velocities at each location in the band structure where an interaction takes place, and in mode localization around and away from the coupling regions. Both these effects contribute significantly to a reduction in the in-plane lattice thermal conductivity as analyzed in the next subsection. While phonon-phonon and phonon-boundary scatterings are still important mechanisms in the membrane-based systems we have considered, the results are consistent with the understanding that the mean free path (MFP) distribution for silicon comfortably spans, at a minimum, the length scale of the membrane thickness. Such a MFP distribution is sufficiently broad to allow at least a portion of the nanopillar standing waves to impact the phonons traveling in-plane across the entire cross section of the membrane.

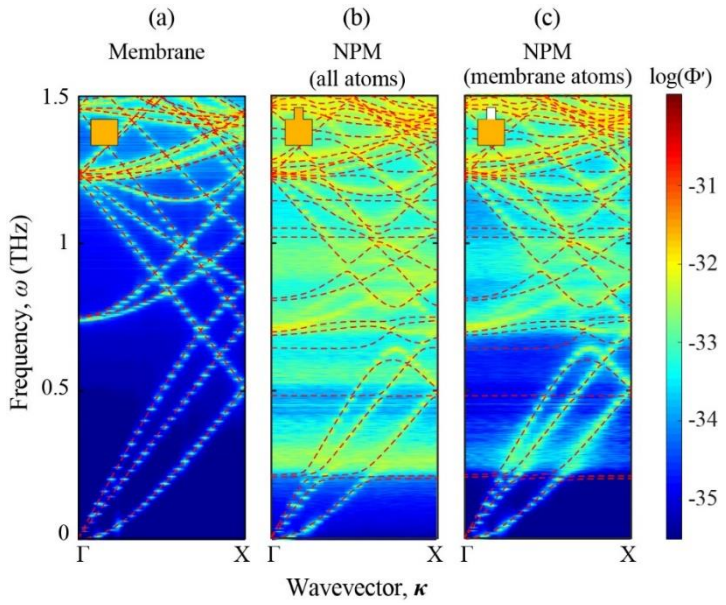

Figure 6.6: Phonon dispersion of a NPM and a corresponding uniform membrane with the same thickness. (a) and (b) show the SED spectrum for the uniform membrane and NPM, respectively. The SED spectrum of the NPM

considering only the membrane atoms is displayed in (c). Dispersion curves obtained by quasi-static LD calculations are overlaid in dashed red lines. The NPM unit-cell dimensions are 3.26×3.26×3.26+1.09×1.09×1.63 nm; the uniform membrane unit-cell dimensions are 3.26×3.26×3.26 nm. Each inset presents a schematic of the unit cell analyzed, with the orange color representing the portion accounted for in the SED calculation. Figure adapted from Ref. [168].

D. Thermal conductivity predictions: Size effects and the compensatory effect

In this sections, we review some recent predictions we obtained for the reduction in the thermal conductivity for NPMs at room temperature, and consider (1) the effect of the size of the nanopillar (for example, by varying its height) while keeping the base membrane thickness and the nanopillar lattice spacing constant, and (2) the effect of the membrane thickness while keeping the nanopillar-height-to-membrane-thickness aspect ratio constant. For this purpose, we used equilibrium MD simulations followed by post-processing the results using the Green-Kubo [284-286] method. In the GK method, the lattice thermal conductivity tensor is calculated from the heat current auto-correlation function (HCACF) by

$$k = \frac{1}{k_B V T^2} \int \langle \boldsymbol{J}(0) \otimes \boldsymbol{J}(t) \rangle, \tag{6.4}$$

where k_B is the Boltzmann constant, V is the total volume of the system including both base membrane and nanopillar portions (as defined earlier), $\boldsymbol{J}$ is the heat current vector (in the unit of energy times length per unit time) computed over all atoms in the system, and $\otimes$ denotes the tensor product operation. Following common notation, T is the temperature and t is the time. The integrand represents the time average of the HCACF. The evaluation of the heat current vector is done using the stress-based formula

$$\boldsymbol{J} = -\sum \boldsymbol{S}_i \boldsymbol{v}_i, \tag{6.5}$$

where $\boldsymbol{S}_i$ and $\boldsymbol{v}_i$, respectively, denote the virial stress tensor and the velocity vector for atom i.

The equilibrium MD simulations were conducted on a set of NPM models and corresponding uniform membrane models (similar to the configurations shown in Fig. 6.2). The computational domain for the NPM and uniform membrane models consists in each case of one unit cell with standard periodic boundary conditions applied at the in-plane boundaries and free boundary conditions applied at the top and bottom surfaces in the z direction [168-170]. The results we present are for systems that were initially equilibrated for 1 ns, with a time step Δt = 0.8 fs, under the NPT ensemble (zero-pressure cell size based on constant number of atoms, pressure, and temperature). The simulations were subsequently allowed to run under the NVE ensemble for an additional 6 ns to collect heat fluxes that were recorded every 4 fs. The 6-ns time span is sufficiently long compared to the longest phonon lifetime to reliably predict the thermal conductivity. With these parameters, the HCACFs generally converged within the first 1 ns, with the rate of convergence depending on the type of the material system (e.g., uniform membrane or NPM). The smaller the value of the predicted thermal conductivity, the shorter the convergence time. The LAMMPS software [287] was used for the implementation of the simulations. To minimize modeling error, we focus our attention on the reduction of the thermal conductivity when a nanopillar (or more) is added to an otherwise uniform membrane. This reduction is expressed as the

ratio $k_r = k_{NPM}/k_{Uniform}$, where k_{NPM} and $k_{Uniform}$ denote the in-plane lattice thermal conductivity of the NPM and corresponding uniform membrane, respectively.

First, we examined an NPM unit cell with the following dimensions: 9.78×9.78×9.78 nm for the base membrane and 8.69×8.69×9.78 nm for a single nanopillar. The predicted k_r for this configuration is 0.27; this corresponds to a reduction of the thermal conductivity by 73% (a factor of 3.7) compared to a uniform membrane with the same thickness. A valid question concerning this result is whether the nanopillars caused this reduction primarily due to the introduction of local resonances, or if it is simply due to the changes incurred to the scattering environment. To address this question, we considered a few more NPM configurations with the same dimensions except for the nanopillar height, which is varied. The k_r predictions for these systems are plotted in Fig. 6.7, where we see a significant dependence on the nanopillar height. The drop in k_r extends from the already significant value of 73% reduction (with a 9.78-nm tall single nanopillar, which is the same height as the membrane thickness) to a remarkable value of 98.7% reduction (with a 586.5-nm tall nanopillar, which is sixty times taller than the membrane thickness). The latter value corresponds to a factor of 75.1 reduction compared to a uniform membrane with the same thickness. Display of such strong dependence on the nanopillar height is consistent with what we expect from the local resonance mechanism because, as described earlier, the number of the local resonances (vibrons) is proportional to the nanoresonator size, and therefore a tall nanopillar produces more sizable mode localizations as well as more group-velocity reductions for the heat-carrying phonons compared to a short nanopillar. These results are obtained by comparing, and replotting in a different format, several data points reported in Ref. [170]. The observed dependency in nanopillar height is in contrast to the conclusions drawn in Ref. [274] where the authors select for their analysis data points from Ref. [170] that correspond to an NPM with a smaller membrane thickness and smaller nanopillar-to-base membrane volume fraction–where the effect of increating the nanopillar height is less profound.

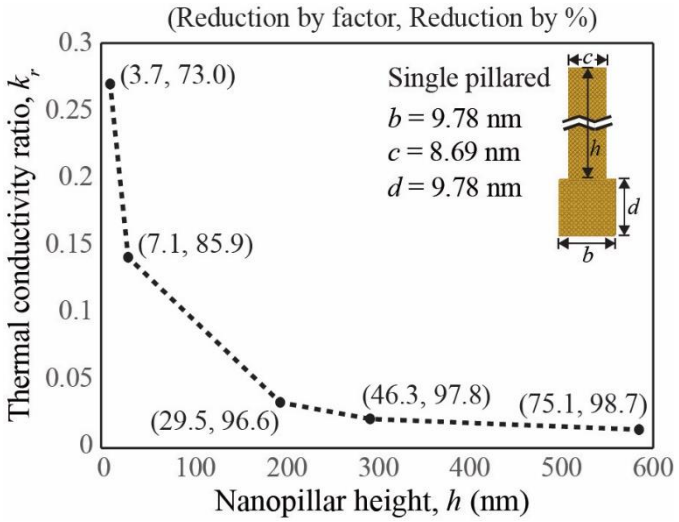

Figure 6.7: Thermal conductivity ratio kr versus nanopillar height for a membrane with a thickness of 9.78 nm. Numbers in parenthesis indicate the thermal conductivity reduction due to addition of the nanopillar, given as a

factor (first number) and as a percentage (second number). Due to the elevated Vr values, the curve demonstrates very strong dependence of the thermal conductivity reduction on the nanopillar height. Results are obtained from Ref. [170].

The overall size of the NPM determines the strength of the dependency of k_r on the nanopillar height [170]. To examine this aspect of the problem, we refer to a broader set of results from Ref. [170], where we consider three sets of NPMs of different membrane thicknesses and nanopillar spacings and widths, for both cases with a single nanopillar (top) and cases with double nanopillars (top and bottom). Using compact notation, the cases we consider are NPMs with the following dimensions: $6\alpha\times6\alpha\times6\alpha+(6\alpha-2)\times(6\alpha-2)\times6\alpha$ CC, $6\alpha\times6\alpha\times6\alpha+(6\alpha-2)\times(6\alpha-2)\times6\alpha2$ CC, and $6\alpha\times6\alpha\times6\alpha+(6\alpha-2)\times(6\alpha-2)\times6\alpha\beta$ CC (for single nanopillars) or $6\alpha\times6\alpha\times6\alpha+(6\alpha-2)\times(6\alpha-2)\times6\alpha\beta+(6\alpha-2)\times(6\alpha-2)\times6\alpha\beta$ CC (for double nanopillars), where CC denotes units of conventional cells, α is a scaling size factor, and $\beta = h/d$. Figure 6.8 provides a summary of the results for a selection of NPM configurations corresponding to α = 1, 2, and 3 and β = 20, 30, and 60. To guide the eye, schematics of the considered unit cells are shown in Figs. 6.8(a) and 6.8(b). As explained in Ref. [170], the higher the value of α in these cases, the more reduction in the thermal conductivity is obtained with increase in nanopillar height. In other words, the larger the value of α, the more delayed is the saturation of k_r with nanopillar height. This is because the larger the width of the base membrane, the more width is available for a nanopillar with a given height–this attribute is encoded in selecting the nanopillar width to be $(6\alpha-2)\times(6\alpha-2)$, instead of, for example, $5\alpha\times5\alpha$. Larger nanopillar width corresponds a larger volume and number of atoms, which in turn means more vibrons are available for contribution to the thermal conductivity reduction. The ratio of nanopillar volume to base-membrane volume V_r is ultimately the key quantity that determines the performance of a nanopillared NPM.

Figure 6.8(c) collects the results for the largest h in each of the three α sets. For the double nanopillar case with a membrane thickness of d = 9.78 nm and a nanopillar height of 586.55 nm, an exceptionally strong value of thermal conductivity reduction is recorded: a factor of 130.0 reduction compared to a corresponding uniform membrane. Not only this is a very promising result for thermoelectric energy conversion, it is also advantageous from a practical point of view because it demonstrates the ability to maintain high performance with upscaling of the size of the NPM unit cell–via the vibron compensation scheme described earlier. This later advantage is vital for enabling industrial-scale deployment for waste heat conversion to electricity and for cooling and refrigeration.

As discussed in Section 6.B.1, the degree of conformity between the phonons and vibrons DOS directly influences the strength of the thermal conductivity reduction. High conformity means more matching between the nanopillar local resonance frequencies and the base-membrane phonon dispersion curves. This, in turn, means more decrease in k_r due to higher occurrence of the three resonance-related effects mentioned earlier, namely, the phonon group velocity reductions, the mode localizations, and the reduction in lifetimes. MD simulations with the same run-time parameters mentioned above were

conducted on the two NPM unit cells featured in Fig. 6.5. The unit cell with the smaller nanopillar [shown in Fig. 6.5(a)] has a nonconformity factor of $\hat{R}_{\mathrm{pv}} = 654$ and a value of k_r = 0.41. In contrast, the unit cell with the large nanopillar [shown in Fig. 6.5(b)] has a nonconformity factor of $\hat{R}_{\mathrm{pv}} = 47$ and a value of k_r = 0.19. This confirms the direct correlation between phonon-vibron DOS conformity and reduction in the thermal conductivity.

A recent study of NPMs produced results that are perfectly explained by the phonon-vibron DOS conformity measure and its relation to the strength of the thermal conductivity reduction. Ma et al. [266] investigated a graphene nanoribbon with a periodic arrangement of branched substructures acting as nanoresonators. The substructures, also referred to as pillars in their work, branched out perpendicularly from the sides along the main axis of the nanoribbon. Several MD simulations where conducted where in each simulation a different isotope of carbon was used for the atoms forming the pillars, while all atoms in the central region of the graphene sheet (i.e., the backbone region where the pillars are branching from) was formed from C^{12}. The thermal conductivity along the axis of the nanoribbon was calculated for each case. The results have shown that the lowest thermal conductivity is for the case where the isotope used in the pillars was C^{12}, i.e., the same isotope as the one used in the central region. As the isotope mass in the pillars was decreased or increased from C^{12}, the level of thermal conductivity reduction decreased (i.e., the absolute thermal conductivity increased compared to the optimal case). This result provides compelling evidence that the prime cause of the thermal conductivity reduction is the presence of the pillar local resonances. When the pillars and the central regions are made out of the same carbon isotope, the degree of conformity between the phonon and vibron DOS is maximized, similar to the case shown in Fig. 6.5(b). As the isotope of the pillars deviates from that of the central region, the pillar vibrons DOS distribution alters due to shifts in the local resonances, and therefore deviates from the DOS of the phonons propagating in the central region. The degree of the conformity gets weaker as the value of the difference in atomic mass between the pillar and central region isotopes increases. The lower the conformity, the less intense the mode localization, resonance hybridizations, and resonance-related lifetime drops, and therefore the less the reduction in the thermal conductivity. The resutls by Ma et al. [266] also confirm that the reduction cannot be primarily due to boundary scattering. This is becasue their pillar sizes and shapes are kept constant, thus if boundary scattering was the prime effect then the thermal conductivity reduction verses pillar isotope value curve would have been mostly constant rather than exhibit a strong minimum value at the point where the isotopes of the pillars and the central region are equal. For the analysis of this system to be complete, the effects of interface scattering across materials with dissimilar isotopes should also be taken into account.

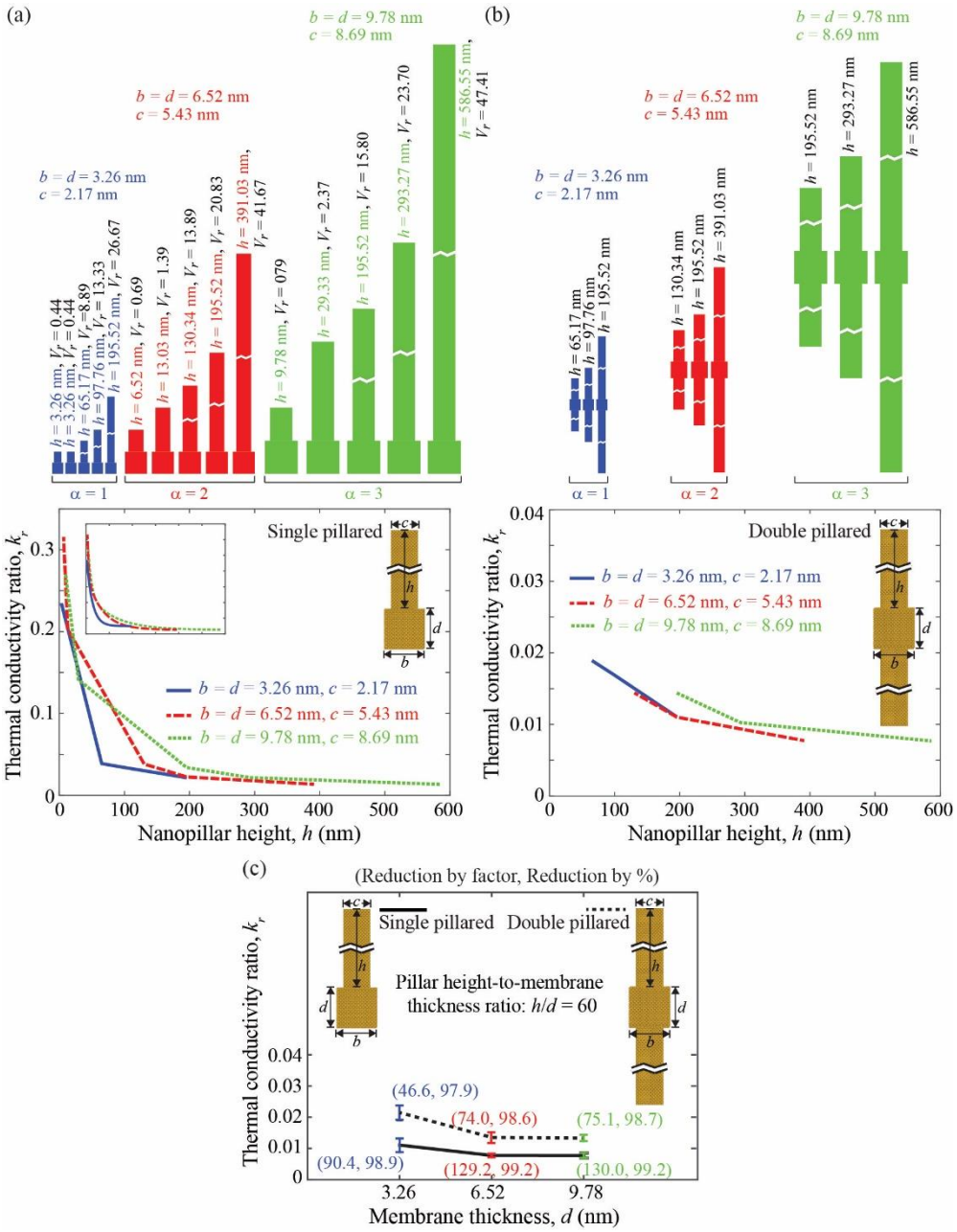

Figure 6.8: Thermal conductivity ratio kr versus nanopillar height for a variety of (a) single-pillared and (b) double-pillared membranes with progressively increasing membrane thickness, nanopillar spacing, nanopillar width, and nanopillar height. The relative geometries are based on the α-formulae provided in the text; Vr values are noted. (c) Thermal conductivity ratio kr versus membrane thickness for configuration 6α×6α×6α+(6α-2)×(6α-2)×6αβ+(6α-2)×(6α-2)×6αβ CC (single) and 6α×6α×6α+(6α-2)×(6α-2)×6αβ+(6α-2)×(6α-2)×6αβ CC (double) and a nanopillar height selected such that the aspect ratio is β = h/d = 60. Numbers in parenthesis indicate the thermal conductivity reduction due to addition of the nanopillar, given as a factor (first number) and as a percentage (second number). It is shown the onset of saturation with nanopillar height is delayed as we advance the α value in theses formulae. Results are obtained from Ref. [170].

E. Summary

In this section, the concept of a nanophononic metamaterial has been reviewed and discussed with a focus on the particular configuration of a nanopillared membrane. Similar to the pillared elastic

metamaterials discussed in the previous sections, at the nanoscale we also benefit from the phenomenon of local resonance and its coupling with the underlying dispersion curves of the base membrane (or plate). The differences, however, are both fundamental and numerous. First, NPMs are engineered to manipulate nanoscale thermal transport properties ; therefore, they are necessarily formed at very small scales corresponding to frequencies reaching a few Terahertz. This is in significant contrast to the at least an order-of-magnitude lower frequencies at the larger size scales. Second, the interest here is not in subwavelength band gaps and/or effective properties. Instead the target resonance-induced effects are (1) the flattenings of the dispersion curves, (2) the mode localizations (within the nanopillars), and (3) the moderate reductions in the phonon lifetimes. The notion of phonon lifetimes in itself underscores yet another key contrast with most macroscale metamaterials, that is because it is a manifestation of the highly nonlinear nature of nanoscale thermal transport. Third, and of critical importance, is that all these effects take place due to the presence of an extremely large number of local resonances, referred to as vibrons in this context, that span the entire frequency spectrum covered by the phonon dispersion curves characterizing wave motion in the host medium. Unlike macroscopic metamaterials, an NPM benefits from local resonances in both the subwavelength and superwavelength regimes. When the unit cell of the nanopillared membrane is designed such (1) that number of vibrons is maximized and (2) the overall conformity between the vibrons and phonons DOS across the spectrum is maximized, the total impact of these three effects in turn gets maximized, and so does the reduction in the in-plane lattice thermal conductivity of the NPM.

Maximizing these NPM design factors requires the ratio V_r of nanopillar volume to base-membrane volume to be as large as possible. A large nanoresonator increases both the number of vibrons and the DOS conformity factor; the latter is illustrated in Fig. 6.5. Increasing V_r requires the membrane width in the unit cell to be as large as possible, as this enables ample increase in nanopillar width. The rewards of increasing the nanopillar height become more significant for wider sized NPM unit cells, as illustrated in Fig. 6.8. Increasing the base-membrane size, however, should not reach the point where the ratio of noncoherent-to-coherent phonon transport becomes excessively large [170]. Key to this limitation is the range and distribution of the phonon mean free path at the temperature of interest. As the dimensions of the NPM components increase, less of the phonon MFP distribution becomes available for the resonance-induced wave effects to take place. An immense advantage of silicon is that it exhibits a wide MFP that ranges from a few nanometers to a few micrometers at room temperature [288]. It is also noteworthy that as the size of the nanopillar increases, width and/or height, eventually the spectrum starts getting saturated with vibrons, which also contributes to the slowing rate of the thermal conductivity rediction observed in Fig. 6.7. The reader is referred to Ref. [170] for a comprehensive investigation on the impact of base-membrane and nanopillar size on the reduction of the thermal conductivity in NPMs.

7 Summary and perspective

Since the seminal works published in 2008, pillared materials and structures have been witnessing continuous growth as a new form of phononic crystals and metamaterials by researchers from broad disciplines. In these systems, numerous avenues are available for manipulating wave dispersion along the base plate or substrate by tailoring the local resonance properties of the branching pillar(s). This platform continues to inspire new fundamental and applied research. In this review, we first gave an overview of the historical developments as well as the current state-of-the-art of pillared phononic crystals and metamaterials. Then we reviewed the mechanism for opening a low-frequency, hybridization band gap and discussed its tunability and applications such as waveguiding. The interaction with electromagnetic waves was covered especially considering the simultaneous existence of phononic and photonic band gaps, a concept which has been termed phoXonic band gaps. The support of elasto-plasmonic interaction was also presented with an elaboration on the fundamental coupling mechanisms between localized plasmon modes and elastic modes. In addition, the tunability and application of whispering-gallery modes and liquid compressional modes were discussed for phononic crystal plates with hollow pillars. In the third section, we reviewed the metamaterial aspect of pillared plates. Trampoline and tailored metamaterial plates were analyzed for widening and lowering band gaps. We reviewed acoustic metalens with locally resonant pillars and discussed how it allows for nearfield subdiffraction focusing. It was explained that the polarization coherence between flexural resonances of the pillars and the anti-symmetric Lamb mode in the base plate enhances the evanescent wave along the interface through the elastic energy re-emitted by the resonators. In the fourth section, we discussed how the intrinsic resonances of a single pillar or a line of pillars can provide a second source to emit Lamb waves that interfere with incident Lamb waves, a mechanism that results in a dip in amplitude or/and phase changing of the transmitted wave. Wavefront manipulation by phase and diffraction engineering of pillared metasurfaces was reviewed. The existence and behavior of Fano resonance, EIT, and ATS were also discussed. In the fifth section, the basic concept of a topological mechanism for a pillared phononic plate was described. We reviewed the robustness of topologically protected edge sates against back scattering, defect, and random perturbations. In the sixth section, the concept of a nanophononic metamaterial for thermal conductivity reduction was reviewed. Unlike macroscopic metamaterials, including pillared metamaterials, an NPM is a highly nonlinear medium that utilizes resonances across the entire spectrum and not only in the subwavelength regime. The NPM resonances may be in the millions. We provided an overview of the three resonance-induced effects that cause thermal conductivity reduction in a nanopillared membrane, namely, group-velocity reduction of the heat-carrying phonons in the base membrane, mode localizations in the nanopillars, and controlled reductions in the lifetimes. We also discussed the key aspect of size dependence in this class of problems, and how NPM design may be optimized for sustained performance with upscaling in size up to the limit where the transport transitions from primarily wave based to complete diffusive transport.

Pillared phononic crystals, metamaterials, and metasurfaces have proven to provide an enormous platform for a wide range of novel physical phenomena and potentially high-impact applications in industry and everyday life. A non-exhaustive list of some challenges and open topics for the future include:

1. A pillar can be regarded as a resonator exhibiting compressional, bending, and torsional modes with different orders. By combining the classic plate theory and the plane-wave expansion method, simplified mathematical models considering out-of-plane displacement (antisymmetric Lamb mode) and a pillar's compressional mode were developed [145, 147, 289]. However, there is still an opportunity for the development of rigorous mathematical treatments–using techniques such as the homogenization method and the multiple scattering method–considering in-plane displacements and the pillar's full modes.

2. Most studies of pillared phononic crystals and metamaterials consider pillars arranged on a periodic lattice. On the other hand, random systems have rich physical properties in their own right and also a potentially wide spectrum of applications. The random induced properties on band gaps, localizations, acoustic transmission, mode conversion, phase transition, nanoscale thermal transport, among others, provide a rich potential for new advancements in applied physics or related disciplines. This track can take shape in the form of disordered pillared phononic crystals or completely random pillared metamaterials, since the key local resonance effects do not depend on periodicity.

3. Robust wave phenomena under topological protection in a pillared platform provides a range of yet to be explored avenues. In addition to the conventional elastic wave theory based on Newtonian equations, topological concepts provide new tools to describe band theory and to synthesize wave functionality based on novel properties. As long as introduced local perturbations are not overly strong to close nontrivial bandgaps, the generalized properties of wavefunctions sweeping a band described by topology are conserved against these local perturbations. In a pillared platform, there is great potential in achieving robust elastic wave states as a mechanical analogue of higher-order topological insulators, Anderson topological insulators, topological bound states in the continuum, topological phases in Moiré superlattices , among others. A wide range of application such as nanomechanical devices, on-chip phononic networks, and information process stand to benefit from this quantum mechanics-inspired track of research.

4. New functionalities and applications of a pillar line as an analog of a metasurface is another promising direction for further research. There is a growing interest in the field of metasurfaces where very thin (sub-wavelength) structures with a modulation of the transmission and

reflection (phase and amplitude) properties of the constitutive unit cells allow various functionalities for anomalous refraction and imaging. The rich resonant properties of an array of pillars opens the opportunity to design a metaline of pillars, in analogy to the metasurfaces, to steer elastic waves (Lamb waves, Rayleigh waves, transverse beam waves, etc.) with advanced functions, especially in non-Hermitian and parity-time symmetry systems. Promising diverse applications such as cloaking, energy absorbing, asymmetric transmission, realization of topological states or bound states in the continuum, wave isolation, focusing, wave deflection, energy harvesting, among others, can be achieved at different size scales and with the possibility of controlled interaction with other physical fields. The pillar platform is naturally of particular interest in view of the engineering applications of Lamb and surface acoustic waves.

5. Deep learning, which is an artificial intelligence method for the exploration of new horizons of recognition and processing of data, is growing significantly and penetrating multiple disciplines such as device design in optics [290], acoustics [291], plasmonics [292, 293] and metamaterials [294]. With the help of deep learning, pillared phononic sensors [295], for example, will be able to detect and predict objects fast and more efficiently. More opportunities for pillared phononic crystals, metamaterials, and metasurfaces are anticipated in this area.

6. The upscaling of nanophononic metamaterials, and their effective integration into practical thermoelectric device architectures are two key steps for the near future. This presents both a rich materials physics problem because of the inherent size effects of conductive thermal transport, and a challenging technological problem because of the need for both high efficiency and low cost for industrial competitiveness.

Acknowledgments

This work was supported by the National Natural Science Foundation of China (Grant No. 11902223), the Shanghai Pujiang Program (Grant No. 19PJ1410100), the program for Professor of Special Appointment (Eastern Scholar) at Shanghai Institutions of Higher Learning, the High-Level Foreign Expert Program of Tongji University, and a start-up funding from Tongji University. The work was also supported by the Advanced Research Projects Agency-Energy (ARPA-E) Grant Number DE-AR0001056. Y.Pennec, B.Bonello and B.Djafari-Rouhani would like to thank the support and hospitality of Professor Yabin Jin and Tongji University during their visit under the High-Level Foreign Expert Program.

References

[1] S.G. Johnson, J.D. Joannopoulos, Photonic crystals: the road from theory to practice, Springer Science & Business Media2001.
[2] P.A. Deymier, Acoustic metamaterials and phononic crystals, Springer Science & Business Media2013.
[3] V. Laude, Phononic crystals: artificial crystals for sonic, acoustic, and elastic waves, Walter de Gruyter GmbH & Co KG2015.

[4] A. Khelif, A. Adibi, Phononic Crystals: Fundamentals and Applications, Springer2015.
[5] J. Sánchez-Dehesa, A. Krokhin, Introduction to Acoustics of Phononic Crystals. Homogenization at Low Frequencies, in: A. Khelif, A. Adibi (Eds.) Phononic Crystals: Fundamentals and Applications, Springer New York, New York, NY, 2016, pp. 1-21.
[6] A.S. Phani, M.I. Hussein, Dynamics of Lattice Materials, John Wiley & Sons2017.
[7] K. Zou, T.-X. Ma, Y.-S. Wang, Investigation of complete bandgaps in a piezoelectric slab covered with periodically structured coatings, Ultrasonics, 65 (2016) 268-276.
[8] E. Yablonovitch, Inhibited Spontaneous Emission in Solid-State Physics and Electronics, Physical Review Letters, 58 (1987) 2059-2062.
[9] J. Sajeev, Strong localization of photons in certain disordered dielectric superlattices, Physical Review Letters, 58 (1987) 2486.
[10] M. Sigalas, E.N. Economou, Band structure of elastic waves in two dimensional systems, Solid State Communications, 86 (1993) 141-143.
[11] M.M. Sigalas, E.N. Economou, Elastic and acoustic wave band structure, Journal of Sound and Vibration, 158 (1992) 377-382.
[12] M.S. Kushwaha, P. Halevi, L. Dobrzynski, B. Djafari-Rouhani, Acoustic band structure of periodic elastic composites, Physical Review Letters, 71 (1993) 2022-2025.
[13] Y. Pennec, B. Djafari-Rouhani, Fundamental Properties of Phononic Crystal, in: A. Khelif, A. Adibi (Eds.) Phononic Crystals: Fundamentals and Applications, Springer New York, New York, NY, 2016, pp. 23-50.
[14] G. Taras, M. Martin, U. Chaitanya, T. Edwin, Sound ideas, Physics World, 18 (2005) 24.
[15] E. Alonso-Redondo, M. Schmitt, Z. Urbach, C.M. Hui, R. Sainidou, P. Rembert, K. Matyjaszewski, M.R. Bockstaller, G. Fytas, A new class of tunable hypersonic phononic crystals based on polymer-tethered colloids, Nat Commun, 6 (2015).
[16] Z. Liu, X. Zhang, Y. Mao, Y.Y. Zhu, Z. Yang, C.T. Chan, P. Sheng, Locally Resonant Sonic Materials, Science, 289 (2000) 1734.
[17] Y. Pennec, J.O. Vasseur, B. Djafari-Rouhani, L. Dobrzyński, P.A. Deymier, Two-dimensional phononic crystals: Examples and applications, Surface Science Reports, 65 (2010) 229-291.
[18] M.I. Hussein, M.J. Leamy, M. Ruzzene, Dynamics of phononic materials and structures: Historical origins, recent progress, and future outlook, Applied Mechanics Reviews, 66 (2014) 040802.
[19] Y. Pennec, B. Djafari-Rouhani, H. Larabi, J.O. Vasseur, A.C. Hladky-Hennion, Low-frequency gaps in a phononic crystal constituted of cylindrical dots deposited on a thin homogeneous plate, Physical Review B, 78 (2008) 104105.
[20] T.-T. Wu, Z.-G. Huang, T.-C. Tsai, T.-C. Wu, Evidence of complete band gap and resonances in a plate with periodic stubbed surface, Applied Physics Letters, 93 (2008) 111902.
[21] H. Khales, A. Hassein-Bey, A. Khelif, Evidence of ultrasonic band gap in aluminum phononic crystal beam, Journal of Vibration and Acoustics, 135 (2013) 041007.
[22] M. Rupin, P. Roux, G. Lerosey, F. Lemoult, Symmetry issues in the hybridization of multi-mode waves with resonators: an example with Lamb waves metamaterial, Scientific reports, 5 (2015).
[23] M. Rupin, F. Lemoult, G. Lerosey, P. Roux, Experimental demonstration of ordered and disordered multiresonant metamaterials for lamb waves, Physical review letters, 112 (2014) 234301.
[24] Y. Achaoui, A. Khelif, S. Benchabane, L. Robert, V. Laude, Experimental observation of locally-resonant and Bragg band gaps for surface guided waves in a phononic crystal of pillars, Physical Review B, 83 (2011) 104201.
[25] J.-C. Hsu, Low-Frequency Forbidden Bands in Phononic Crystal Plates with Helmholtz Resonators, Japanese Journal of Applied Physics, 50 (2011) 07HB01.
[26] Y. Li, L. Zhu, T. Chen, Plate-type elastic metamaterials for low-frequency broadband elastic wave attenuation, Ultrasonics, 73 (2017) 34-42.
[27] H.-b. Zhang, J.-j. Chen, X. Han, Lamb wave band gaps in a homogenous plate with periodic tapered surface, Journal of Applied Physics, 112 (2012) 054503.
[28] J.-j. Chen, H.-b. Zhang, X. Han, Local resonance broadband gap in a homogeneous plate with periodic truncated cones, Japanese Journal of Applied Physics, 52 (2013) 034301.
[29] M. Oudich, Y. Li, B.M. Assouar, Z. Hou, A sonic band gap based on the locally resonant phononic plates with stubs, New Journal of Physics, 12 (2010) 083049.

[30] A. Hu, X. Zhang, F. Wu, Y. Yao, Enlargement of the locally resonant Lamb wave band gap of the phononic crystal plate at the deep sub-wavelength scale, Materials Research Express, 1 (2014) 045801.
[31] Y. Li, T. Chen, X. Wang, Y. Xi, Q. Liang, Enlargement of locally resonant sonic band gap by using composite plate-type acoustic metamaterial, Physics Letters A, 379 (2015) 412-416.
[32] H.-J. Zhao, H.-W. Guo, M.-X. Gao, R.-Q. Liu, Z.-Q. Deng, Vibration band gaps in double-vibrator pillared phononic crystal plate, Journal of Applied Physics, 119 (2016) 014903.
[33] S. Li, T. Chen, X. Wang, Y. Li, W. Chen, Expansion of lower-frequency locally resonant band gaps using a double-sided stubbed composite phononic crystals plate with composite stubs, Physics Letters A, 380 (2016) 2167-2172.
[34] L. Li, A. Cai, Control of the low-frequency vibrations of elastic metamaterial shafts with discretized arc-rubber layers, Japanese Journal of Applied Physics, 55 (2016) 067301.
[35] C. Sugino, S. Leadenham, M. Ruzzene, A. Erturk, On the mechanism of bandgap formation in locally resonant finite elastic metamaterials, Journal of Applied Physics, 120 (2016) 134501.
[36] N.M. Frandsen, O.R. Bilal, J.S. Jensen, M.I. Hussein, Inertial amplification of continuous structures: Large band gaps from small masses, Journal of Applied Physics, 119 (2016) 124902.
[37] K. Lu, J.H. Wu, L. Jing, N. Gao, D. Guan, The two-degree-of-freedom local resonance elastic metamaterial plate with broadband low-frequency bandgaps, Journal of Physics D: Applied Physics, 50 (2017) 095104.
[38] Z.-G. Huang, Silicon-based filters, resonators and acoustic channels with phononic crystal structures, Journal of Physics D: Applied Physics, 44 (2011) 245406.
[39] X.-P. Wang, P. Jiang, T.-N. Chen, J. Zhu, Tuning characteristic of band gap and waveguide in a multi-stub locally resonant phononic crystal plate, AIP Advances, 5 (2015) 107141.
[40] C. Zhou, Y. Sai, J. Chen, Tunable Lamb wave band gaps in two-dimensional magnetoelastic phononic crystal slabs by an applied external magnetostatic field, Ultrasonics, 71 (2016) 69-74.
[41] P. Jiang, Low-frequency band gap and defect state characteristics in a multi-stub phononic crystal plate with slit structure, Journal of Applied Physics, 121 (2017) 015106.
[42] J. Ma, Z. Hou, B.M. Assouar, Opening a large full phononic band gap in thin elastic plate with resonant units, Journal of Applied Physics, 115 (2014) 093508.
[43] S. Zhang, J. Hui Wu, Z. Hu, Low-frequency locally resonant band-gaps in phononic crystal plates with periodic spiral resonators, Journal of Applied Physics, 113 (2013) 163511.
[44] C. Ming, J. Chen, X. Han, H. Zhang, Lamb wave band gaps in a homogenous plate with periodic Gaussian surfaces, Physica Scripta, 88 (2013) 035601.
[45] Y. El Hassouani, C. Li, Y. Pennec, E. El Boudouti, H. Larabi, A. Akjouj, O.B. Matar, V. Laude, N. Papanikolaou, A. Martinez, Dual phononic and photonic band gaps in a periodic array of pillars deposited on a thin plate, Physical Review B, 82 (2010) 155405.
[46] R. Pourabolghasem, A. Khelif, S. Mohammadi, A.A. Eftekhar, A. Adibi, Physics of band-gap formation and its evolution in the pillar-based phononic crystal structures, Journal of Applied Physics, 116 (2014) 013514.
[47] E. Miranda Jr, E. Nobrega, A. Ferreira, J. Dos Santos, Flexural wave band gaps in a multi-resonator elastic metamaterial plate using Kirchhoff-Love theory, Mechanical Systems and Signal Processing, 116 (2019) 480-504.
[48] J.-C. Hsu, Local resonances-induced low-frequency band gaps in two-dimensional phononic crystal slabs with periodic stepped resonators, Journal of Physics D: Applied Physics, 44 (2011) 055401.
[49] A. Khelif, Y. Achaoui, B. Aoubiza, Surface acoustic waves in pillars-based two-dimensional phononic structures with different lattice symmetries, Journal of applied physics, 112 (2012) 033511.
[50] M.B. Assouar, J.-H. Sun, F.-S. Lin, J.-C. Hsu, Hybrid phononic crystal plates for lowering and widening acoustic band gaps, Ultrasonics, 54 (2014) 2159-2164.
[51] Z. Zhang, X. Han, G. Ji, The bandgap controlling by geometrical symmetry design in hybrid phononic crystal, International Journal of Modern Physics B, DOI (2017) 1850034.
[52] Y. Achaoui, V. Laude, S. Benchabane, A. Khelif, Local resonances in phononic crystals and in random arrangements of pillars on a surface, Journal of Applied Physics, 114 (2013) 104503.
[53] P. Celli, S. Gonella, Manipulating waves with LEGO® bricks: A versatile experimental platform for metamaterial architectures, Applied Physics Letters, 107 (2015) 081901.

[54] B. Assouar, M. Oudich, Enlargement of a locally resonant sonic band gap by using double-sides stubbed phononic plates, Applied Physics Letters, 100 (2012) 123506.
[55] P. Wang, T.-N. Chen, K.-P. Yu, X.-P. Wang, Lamb wave band gaps in a double-sided phononic plate, Journal of Applied Physics, 113 (2013) 053509.
[56] H.-J. Zhao, H.-W. Guo, B.-Y. Li, Z.-Q. Deng, R.-Q. Liu, Flexural vibration band gaps in a double-side phononic crystal plate, Journal of Applied Physics, 118 (2015) 044906.
[57] A. Song, X. Wang, T. Chen, P. Jiang, K. Bao, Low-frequency bandgaps of two-dimensional phononic crystal plate composed of asymmetric double-sided cylinder stubs, International Journal of Modern Physics B, 30 (2016) 1650029.
[58] S. Li, Y. Xi, T. Chen, X. Wang, Modulating lamb wave band gaps using an elastic metamaterial plate, Acoustical Physics, 63 (2017) 508-516.
[59] Y. Jin, N. Fernez, Y. Pennec, B. Bonello, R.P. Moiseyenko, S. Hémon, Y. Pan, B. Djafari-Rouhani, Tunable waveguide and cavity in a phononic crystal plate by controlling whispering-gallery modes in hollow pillars, Physical Review B, 93 (2016) 054109.
[60] Y. Jin, Y. Pennec, Y. Pan, B. Djafari-Rouhani, Phononic crystal plate with hollow pillars actively controlled by fluid filling, Crystals, 6 (2016) 64.
[61] Y. Jin, Y. Pennec, Y. Pan, B. Djafari-Rouhani, Phononic crystal plate with hollow pillars connected by thin bars, Journal of Physics D: Applied Physics, 50 (2017) 035301.
[62] Y. Li, T. Chen, X. Wang, K. Yu, W. Chen, Propagation of Lamb waves in one-dimensional radial phononic crystal plates with periodic corrugations, Journal of Applied Physics, 115 (2014) 054907.
[63] F. Shu, Y. Liu, J. Wu, Y. Wu, Band gap in tubular pillar phononic crystal plate, Ultrasonics, 71 (2016) 172-176.
[64] T.-T. Wang, Y.-F. Wang, Y.-S. Wang, V. Laude, Tunable fluid-filled phononic metastrip, Applied Physics Letters, 111 (2017) 041906.
[65] Y.-F. Wang, T.-T. Wang, Y.-S. Wang, V. Laude, Reconfigurable Phononic-Crystal Circuits Formed by Coupled Acoustoelastic Resonators, Physical Review Applied, 8 (2017) 014006.
[66] O.R. Bilal, M.I. Hussein, Trampoline metamaterial: Local resonance enhancement by springboards, Applied Physics Letters, 103 (2013) 111901.
[67] C. Ma, J. Guo, Y. Liu, Extending and lowing band gaps in one-dimensional phononic crystal strip with pillars and holes, Journal of Physics and Chemistry of Solids, 87 (2015) 95-103.
[68] E. Coffy, T. Lavergne, M. Addouche, S. Euphrasie, P. Vairac, A. Khelif, Ultra-wide acoustic band gaps in pillar-based phononic crystal strips, Journal of Applied Physics, 118 (2015) 214902.
[69] O.R. Bilal, A. Foehr, C. Daraio, Observation of trampoline phenomena in 3D-printed metamaterial plates, Extreme Mechanics Letters, 15 (2017) 103-107.
[70] E. Coffy, S. Euphrasie, M. Addouche, P. Vairac, A. Khelif, Evidence of a broadband gap in a phononic crystal strip, Ultrasonics, 78 (2017) 51-56.
[71] Y. Jin, B. Bonello, Y. Pan, Acoustic metamaterials with piezoelectric resonant structures, Journal of Physics D: Applied Physics, 47 (2014) 245301.
[72] A. Bergamini, T. Delpero, L.D. Simoni, L.D. Lillo, M. Ruzzene, P. Ermanni, Phononic crystal with adaptive connectivity, Advanced Materials, 26 (2014) 1343-1347.
[73] A.E. Bergamini, M. Zündel, E.A. Flores Parra, T. Delpero, M. Ruzzene, P. Ermanni, Hybrid dispersive media with controllable wave propagation: A new take on smart materials, Journal of Applied Physics, 118 (2015) 154310.
[74] F. Casadei, T. Delpero, A. Bergamini, P. Ermanni, M. Ruzzene, Piezoelectric resonator arrays for tunable acoustic waveguides and metamaterials, Journal of Applied Physics, 112 (2012) 064902.
[75] W. Zhou, Y. Wu, L. Zuo, Vibration and wave propagation attenuation for metamaterials by periodic piezoelectric arrays with high-order resonant circuit shunts, Smart Materials and Structures, 24 (2015) 065021.
[76] S. Chen, Y. Fan, Q. Fu, H. Wu, Y. Jin, J. Zheng, F. Zhang, A review of tunable acoustic metamaterials, Applied Sciences, 8 (2018) 1480.
[77] A. Khelif, Y. Achaoui, S. Benchabane, V. Laude, B. Aoubiza, Locally resonant surface acoustic wave band gaps in a two-dimensional phononic crystal of pillars on a surface, Physical Review B, 81 (2010) 214303.
[78] A. Khelif, Y. Achaoui, B. Aoubiza, In-plane confinement and waveguiding of surface acoustic waves through line defects in pillars-based phononic crystal, AIP advances, 1 (2011) 041404.

[79] M. Oudich, B. Assouar, Surface acoustic wave band gaps in a diamond-based two-dimensional locally resonant phononic crystal for high frequency applications, Journal of Applied Physics, 111 (2012) 014504.
[80] Y. Li, Z. Hou, Surface acoustic waves in a two-dimensional phononic crystal slab with locally resonant units, Solid State Communications, 173 (2013) 19-23.
[81] Y. Guo, M. Schubert, T. Dekorsy, Finite element analysis of surface modes in phononic crystal waveguides, Journal of Applied Physics, 119 (2016) 124302.
[82] D. Zhang, J. Zhao, B. Bonello, F. Zhang, W. Yuan, Y. Pan, Z. Zhong, Investigation of surface acoustic wave propagation in composite pillar based phononic crystals within both local resonance and Bragg scattering mechanism regimes, Journal of Physics D: Applied Physics, 50 (2017) 435602.
[83] B. Ash, S. Worsfold, P. Vukusic, G. Nash, A highly attenuating and frequency tailorable annular hole phononic crystal for surface acoustic waves, Nature Communications, 8 (2017) 174.
[84] B. Djafari Rouhani, Y. Pennec, E. El Boudouti, J. Vasseur, Y. El Hassouani, C. Li, A. Akjouj, D. Bria, Band gap engineering in simultaneous phononic and photonic crystal slabs, Applied Physics A: Materials Science & Processing, 103 (2011) 735-739.
[85] V. Laude, A. Belkhir, A.F. Alabiad, M. Addouche, S. Benchabane, A. Khelif, F.I. Baida, Extraordinary nonlinear transmission modulation in a doubly resonant acousto-optical structure, Optica, 4 (2017) 1245-1250.
[86] M. Oudich, B. Djafari-Rouhani, Y. Pennec, M.B. Assouar, B. Bonello, Negative effective mass density of acoustic metamaterial plate decorated with low frequency resonant pillars, Journal of Applied Physics, 116 (2014) 184504.
[87] E.G. Williams, P. Roux, M. Rupin, W. Kuperman, Theory of multiresonant metamaterials for a 0 lamb waves, Physical Review B, 91 (2015) 104307.
[88] B. Assouar, M. Oudich, X. Zhou, Acoustic metamaterials for sound mitigation, Comptes Rendus Physique, 17 (2016) 524-532.
[89] Z.Y. Yan, J.H. Wu, Ultra-low-frequency broadband of a new-type acoustic metamaterial beams with stiffness array, Journal of Physics D: Applied Physics, 50 (2017) 355104.
[90] Y. Jin, B. Bonello, R.P. Moiseyenko, Y. Pennec, O. Boyko, B. Djafari-Rouhani, Pillar-type acoustic metasurface, Physical Review B, 96 (2017) 104311.
[91] Y. Jin, E.H.E. Boudouti, Y. Pennec, B. Djafari-Rouhani, Tunable Fano resonances of Lamb modes in a pillared metasurface, Journal of Physics D: Applied Physics, 50 (2017) 425304.
[92] S. Anguiano, A. Bruchhausen, B. Jusserand, I. Favero, F. Lamberti, L. Lanco, I. Sagnes, A. Lemaître, N. Lanzillotti-Kimura, P. Senellart, Micropillar resonators for optomechanics in the extremely high 19–95-GHz frequency range, Physical review letters, 118 (2017) 263901.
[93] M. Oudich, B. Djafari-Rouhani, B. Bonello, Y. Pennec, F. Sarry, Phononic Crystal Made of Multilayered Ridges on a Substrate for Rayleigh Waves Manipulation, Crystals, 7 (2017) 372.
[94] M. Oudich, B. Djafari-Rouhani, B. Bonello, Y. Pennec, S. Hemaidia, F. Sarry, D. Beyssen, Rayleigh Waves in Phononic Crystal Made of Multilayered Pillars: Confined Modes, Fano Resonances, and Acoustically Induced Transparency, Physical Review Applied, 9 (2018) 034013.
[95] M.S. Kushwaha, A. Akjouj, B. Djafari-Rouhani, L. Dobrzynski, J.O. Vasseur, Acoustic spectral gaps and discrete transmisson in slender tubes, Solid State Communications, 106 (1998) 659-663.
[96] H. Al-Wahsh, A. Akjouj, B. Djafari-Rouhani, J.O. Vasseur, L. Dobrzynski, P.A. Deymier, Large magnonic band gaps and defect modes in one-dimensional comblike structures, Physical Review B, 59 (1999) 8709-8719.
[97] B. Djafari-Rouhani, J.O. Vasseur, A. Akjouj, L. Dobrzynski, M.S. Kushwaha, P.A. Deymier, J. Zemmouri, Giant stop bands and defect modes in one-dimensional waveguide with dangling side branches, Progress in Surface Science, 59 (1998) 255-264.
[98] E.H.E. Boudouti, T. Mrabti, H. Al-Wahsh, B. Djafari-Rouhani, A. Akjouj, L. Dobrzynski, Transmission gaps and Fano resonances in an acoustic waveguide: analytical model, Journal of Physics: Condensed Matter, 20 (2008) 255212.
[99] Y. Jin, Y. Pennec, B. Djafari-Rouhani, Acoustic analogue of electromagnetically induced transparency and Autler–Townes splitting in pillared metasurfaces, Journal of Physics D: Applied Physics, 51 (2018) 494004.
[100] S. Hein, W. Koch, L. Nannen, Trapped modes and Fano resonances in two-dimensional acoustical duct–cavity systems, Journal of Fluid Mechanics, 692 (2012) 257-287.

[101] L. Dobrzynski, B. Djafari-Rouhani, A. Akjouj, J.O. Vasseur, J. Zemmouri, Resonant tunnelling of acoustic waves between two slender tubes, EPL (Europhysics Letters), 46 (1999) 467.
[102] J. Ash, W.M. Robertson, Acoustic band gap measurements in waveguides with periodic resonant structures, Zeitschrift für Kristallographie-Crystalline Materials, 220 (2005) 824-828.
[103] K.J.B. Lee, M.K. Jung, S.H. Lee, Highly tunable acoustic metamaterials based on a resonant tubular array, Physical Review B, 86 (2012) 184302.
[104] Y.-F. Wang, V. Laude, Y.-S. Wang, Coupling of evanescent and propagating guided modes in locally resonant phononic crystals, Journal of Physics D: Applied Physics, 47 (2014) 475502.
[105] A.-C. Hladky-Hennion, J. Vasseur, B. Djafari-Rouhani, M. de Billy, Sonic band gaps in one-dimensional phononic crystals with a symmetric stub, Physical Review B, 77 (2008) 104304.
[106] A.-C. Hladky-Hennion, C. Granger, J. Vasseur, M. de Billy, Propagation of elastic waves in one-dimensional periodic stubbed waveguides, Physical Review B, 82 (2010) 104307.
[107] Y. Yao, Z. Hou, F. Wu, X. Fu, The band structure and propagation property of lamb waves in stubbed waveguides, Wave Motion, 47 (2010) 343-349.
[108] Y. Yao, Z. Hou, F. Wu, X. Zhang, Low-frequency band gaps in one-dimensional thin phononic crystal plate with periodic stubbed surface, Physica B: Condensed Matter, 406 (2011) 2249-2253.
[109] X.F. Wang, M.S. Kushwaha, P. Vasilopoulos, Tunability of acoustic spectral gaps and transmission in periodically stubbed waveguides, Physical Review B, 65 (2001) 035107.
[110] W. Li, K. Chen, Phonon heat transport through periodically stubbed waveguides, Physics Letters A, 357 (2006) 378-383.
[111] Z.-X. Xie, J.-Z. Liu, X. Yu, H.-B. Wang, Y.-X. Deng, K.-M. Li, Y. Zhang, Tunability of acoustic phonon transmission and thermal conductance in three dimensional quasi-periodically stubbed waveguides, Journal of Applied Physics, 117 (2015) 114308.
[112] B. Djafari-Rouhani, Y. Pennec, H. Larabi, Band Structure and Phonon Transport in a Phononic Crystal Made of a Periodic Array of Dots on a Membrane, Springer Netherlands, Dordrecht, 2010, pp. 127-138.
[113] M. Addouche, M.A. Al-Lethawe, A. Choujaa, A. Khelif, Superlensing effect for surface acoustic waves in a pillar-based phononic crystal with negative refractive index, Applied Physics Letters, 105 (2014) 023501.
[114] M.A. Al-Lethawe, M. Addouche, A. Khelif, S. Guenneau, All-angle negative refraction for surface acoustic waves in pillar-based two-dimensional phononic structures, New Journal of Physics, 14 (2012) 123030.
[115] M. Rupin, S. Catheline, P. Roux, Super-resolution experiments on lamb waves using a single emitter, Applied Physics Letters, 106 (2015) 024103.
[116] Y. Pennec, B. Djafari-Rouhani, H. Larabi, A. Akjouj, J. Gillet, J. Vasseur, G. Thabet, Phonon transport and waveguiding in a phononic crystal made up of cylindrical dots on a thin homogeneous plate, Physical Review B, 80 (2009) 144302.
[117] T.-C. Wu, T.-T. Wu, J.-C. Hsu, Waveguiding and frequency selection of Lamb waves in a plate with a periodic stubbed surface, Physical Review B, 79 (2009) 104306.
[118] M. Oudich, M.B. Assouar, Z. Hou, Propagation of acoustic waves and waveguiding in a two-dimensional locally resonant phononic crystal plate, Applied Physics Letters, 97 (2010) 193503.
[119] J.-C. Hsu, T.-T. Wu, H.-S. Hsu, Measurement of frequency gaps and waveguiding in phononic plates with periodic stepped cylinders using pulsed laser generated ultrasound, Journal of Applied Physics, 113 (2013) 083511.
[120] M. Addouche, M.A. Al-Lethawe, A. Elayouch, A. Khelif, Subwavelength waveguiding of surface phonons in pillars-based phononic crystal, AIP Advances, 4 (2014) 124303.
[121] A. Shelke, S. Banerjee, T. Zhenhua, L. Yu, Spiral Lamb Waveguide for Spatial Filtration of Frequencies in a Confined Space, Experimental Mechanics, 55 (2015) 1199-1209.
[122] P. Jiang, X.-P. Wang, T.-N. Chen, J. Zhu, Band gap and defect state engineering in a multi-stub phononic crystal plate, Journal of Applied Physics, 117 (2015) 154301.
[123] J. Yin, S. Zhang, H. Zhang, B. Chen, Band structure and transmission characteristics of complex phononic crystals by multi-level substructure scheme, International Journal of Modern Physics B, 29 (2015) 1550013.

[124] R. Dehghannasiri, R. Pourabolghasem, A.A. Eftekhar, A. Adibi, Integrated phononic crystal resonators based on adiabatically-terminated phononic crystal waveguides, AIP Advances, 6 (2016) 121603.
[125] D. Feng, W. Jiang, D. Xu, B. Xiong, Y. Wang, Micro-silicon phononic crystal with locally resonant theory, Applied Physics Letters, 110 (2017) 171902.
[126] R. Pourabolghasem, R. Dehghannasiri, A.A. Eftekhar, A. Adibi, Waveguiding Effect in the Gigahertz Frequency Range in Pillar-based Phononic-Crystal Slabs, Physical Review Applied, 9 (2018) 014013.
[127] W.T. Yuan, J.F. Zhao, B. Bonello, B. Djafari-Rouhani, X.Q. Zhang, Y.D. Pan, Z. Zhong, Compact Waveguide and Guided Beam Pattern Based on the Whispering-Gallery Mode of a Hollow Pillar in a Phononic Crystal Plate, Physical Review Applied, 10 (2018).
[128] M. Oudich, M. Senesi, M.B. Assouar, M. Ruzenne, J.-H. Sun, B. Vincent, Z. Hou, T.-T. Wu, Experimental evidence of locally resonant sonic band gap in two-dimensional phononic stubbed plates, Physical Review B, 84 (2011) 165136.
[129] B. Assouar, M. Senesi, M. Oudich, M. Ruzzene, Z. Hou, Broadband plate-type acoustic metamaterial for low-frequency sound attenuation, Applied Physics Letters, 101 (2012) 173505.
[130] M. Oudich, X. Zhou, M. Badreddine Assouar, General analytical approach for sound transmission loss analysis through a thick metamaterial plate, Journal of Applied Physics, 116 (2014) 193509.
[131] R. Pourabolghasem, S. Mohammadi, A.A. Eftekhar, A. Khelif, A. Adibi, Experimental evidence of high-frequency complete elastic bandgap in pillar-based phononic slabs, Applied Physics Letters, 105 (2014) 231908.
[132] A. Colombi, P. Roux, S. Guenneau, P. Gueguen, R.V. Craster, Forests as a natural seismic metamaterial: Rayleigh wave bandgaps induced by local resonances, Scientific reports, 6 (2016).
[133] D. Colquitt, A. Colombi, R. Craster, P. Roux, S. Guenneau, Seismic metasurfaces: Sub-wavelength resonators and Rayleigh wave interaction, Journal of the Mechanics and Physics of Solids, 99 (2017) 379-393.
[134] A. Colombi, R.V. Craster, D. Colquitt, Y. Achaoui, S. Guenneau, P. Roux, M. Rupin, Elastic Wave Control Beyond Band-Gaps: Shaping the Flow of Waves in Plates and Half-Spaces with Subwavelength Resonant Rods, Frontiers in Mechanical Engineering, 3 (2017) 10.
[135] J. Zhao, R. Marchal, B. Bonello, O. Boyko, Efficient focalization of antisymmetric Lamb waves in gradient-index phononic crystal plates, Applied Physics Letters, 101 (2012) 261905.
[136] Y. Jin, D. Torrent, Y. Pennec, Y. Pan, B. Djafari-Rouhani, Simultaneous control of the S 0 and A 0 Lamb modes by graded phononic crystal plates, Journal of Applied Physics, 117 (2015) 244904.
[137] Y. Jin, D. Torrent, Y. Pennec, Y. Pan, B. Djafari-Rouhani, Gradient index devices for the full control of elastic waves in plates, Scientific reports, 6 (2016).
[138] Y. Jin, D. Torrent, Y. Pennec, G. Lévêque, Y. Pan, B. Djafari-Rouhani, Multimodal and omnidirectional beam splitters for Lamb modes in elastic plates, AIP Advances, 6 (2016) 121602.
[139] Y. Jin, D. Torrent, B. Djafari-Rouhani, Invisible omnidirectional lens for flexural waves in thin elastic plates, Journal of Physics D: Applied Physics, 50 (2017) 225301.
[140] Y. Jin, B. Djafari-Rouhani, D. Torrent, Gradient index phononic crystals and metamaterials, Nanophotonics, DOI (2019).
[141] J. Zhao, B. Bonello, O. Boyko, Focusing of the lowest-order antisymmetric Lamb mode behind a gradient-index acoustic metalens with local resonators, Physical Review B, 93 (2016) 174306.
[142] A. Colombi, Resonant metalenses for flexural waves in plates, The Journal of the Acoustical Society of America, 140 (2016) EL423-EL428.
[143] A. Colombi, D. Colquitt, P. Roux, S. Guenneau, R.V. Craster, A seismic metamaterial: The resonant metawedge, Scientific reports, 6 (2016).
[144] Y. Guo, M. Hettich, T. Dekorsy, Guiding of elastic waves in a two-dimensional graded phononic crystal plate, New Journal of Physics, 19 (2017) 013029.
[145] D. Torrent, D. Mayou, J. Sánchez-Dehesa, Elastic analog of graphene: Dirac cones and edge states for flexural waves in thin plates, Physical Review B, 87 (2013) 115143.
[146] R.K. Pal, M. Ruzzene, Edge waves in plates with resonators: an elastic analogue of the quantum valley Hall effect, New Journal of Physics, 19 (2017) 025001.

[147] R. Chaunsali, C.-W. Chen, J. Yang, Subwavelength and directional control of flexural waves in zone-folding induced topological plates, Physical Review B, 97 (2018) 054307.
[148] S.-Y. Yu, X.-C. Sun, X. Ni, Q. Wang, X.-J. Yan, C. He, X.-P. Liu, L. Feng, M.-H. Lu, Y.-F. Chen, Surface phononic graphene, Nature materials, 15 (2016) 1243-1247.
[149] J. Vila, R.K. Pal, M. Ruzzene, Observation of topological valley modes in an elastic hexagonal lattice, Physical Review B, 96 (2017) 134307.
[150] J.-J. Chen, S.-Y. Huo, Z.-G. Geng, H.-B. Huang, X.-F. Zhu, Topological valley transport of plate-mode waves in a homogenous thin plate with periodic stubbed surface, AIP Advances, 7 (2017) 115215.
[151] Y. Jin, D. Torrent, B. Djafari-Rouhani, Robustness of conventional and topologically protected edge states in phononic crystal plates, Physical Review B, 98 (2018) 054307.
[152] Y. Li, B. Liang, Z.-m. Gu, X.-y. Zou, J.-c. Cheng, Reflected wavefront manipulation based on ultrathin planar acoustic metasurfaces, Scientific Reports, 3 (2013) 2546.
[153] K. Tang, C. Qiu, M. Ke, J. Lu, Y. Ye, Z. Liu, Anomalous refraction of airborne sound through ultrathin metasurfaces, Scientific Reports, 4 (2014) 6517.
[154] Y. Xie, W. Wang, H. Chen, A. Konneker, B.-I. Popa, S.A. Cummer, Wavefront modulation and subwavelength diffractive acoustics with an acoustic metasurface, Nature Communications, 5 (2014) 5553.
[155] B. Liang, J.-c. Cheng, C.-W. Qiu, Wavefront manipulation by acoustic metasurfaces: from physics and applications, Nanophotonics, 2018, pp. 1191.
[156] Y. Jin, R. Kumar, O. Poncelet, O. Mondain-Monval, T. Brunet, Flat acoustics with soft gradient-index metasurfaces, Nature Communications, 10 (2019) 143.
[157] Y. Jin, X. Fang, Y. Li, D. Torrent, Engineered diffraction gratings for acoustic cloaking, Physical Review Applied, 11 (2019) 011004.
[158] B. Assouar, B. Liang, Y. Wu, Y. Li, J.-C. Cheng, Y. Jing, Acoustic metasurfaces, Nature Reviews Materials, 3 (2018) 460-472.
[159] N. Yu, P. Genevet, M.A. Kats, F. Aieta, J.-P. Tetienne, F. Capasso, Z. Gaburro, Light Propagation with Phase Discontinuities: Generalized Laws of Reflection and Refraction, Science, 334 (2011) 333-337.
[160] Y. Cheng, Y. Jin, Y. Zhou, T. Hao, Y. Li, Distinction of Acoustically Induced Transparency and Autler-Townes Splitting by Helmholtz Resonators, Physical Review Applied, 12 (2019) 044025.
[161] B. Graczykowski, S. Mielcarek, A. Trzaskowska, J. Sarkar, P. Hakonen, B. Mroz, Tuning of a hypersonic surface phononic band gap using a nanoscale two-dimensional lattice of pillars, Physical Review B, 86 (2012) 085426.
[162] S. Mielcarek, A. Trzaskowska, B. Graczykowski, J. Sarkar, Hypersonic surface waves in 2D titanium nanostructure on silicon, physica status solidi (RRL)-Rapid Research Letters, 6 (2012) 175-177.
[163] A. Trzaskowska, S. Mielcarek, J. Sarkar, Band gap in hypersonic surface phononic lattice of nickel pillars, Journal of Applied Physics, 114 (2013) 134304.
[164] B. Graczykowski, M. Sledzinska, F. Alzina, J. Gomis-Bresco, J. Reparaz, M. Wagner, C.S. Torres, Phonon dispersion in hypersonic two-dimensional phononic crystal membranes, Physical Review B, 91 (2015) 075414.
[165] D. Yudistira, A. Boes, B. Graczykowski, F. Alzina, L. Yeo, C.S. Torres, A. Mitchell, Nanoscale pillar hypersonic surface phononic crystals, Physical Review B, 94 (2016) 094304.
[166] B.L. Davis, M.I. Hussein, Nanophononic metamaterial: Thermal conductivity reduction by local resonance, Physical review letters, 112 (2014) 055505.
[167] M.I. Hussein, B.L. Davis, Nanophononic metamaterials, Google Patents, 2016.
[168] H. Honarvar, M.I. Hussein, Spectral energy analysis of locally resonant nanophononic metamaterials by molecular simulations, Physical Review B, 93 (2016) 081412.
[169] H. Honarvar, L. Yang, M.I. Hussein, Thermal transport size effects in silicon membranes featuring nanopillars as local resonators, Applied Physics Letters, 108 (2016) 263101.
[170] H. Honarvar, M.I. Hussein, Two orders of magnitude reduction in silicon membrane thermal conductivity by resonance hybridizations, Physical Review B, 97 (2018) 195413.
[171] M.I. Hussein, H. Honarvar, Resonant thermal transport in nanophononic metamaterials, Handbook of Materials Modeling: Applications: Current and Emerging Materials, DOI (2018) 1-21.

[172] R. Anufriev, R. Yanagisawa, M. Nomura, Aluminium nanopillars reduce thermal conductivity of silicon nanobeams, Nanoscale, 9 (2017) 15083-15088.
[173] L. Rayleigh, CXII. The problem of the whispering gallery, The London, Edinburgh, and Dublin Philosophical Magazine and Journal of Science, 20 (1910) 1001-1004.
[174] J. Gomis-Bresco, D. Navarro-Urrios, M. Oudich, S. El-Jallal, A. Griol, D. Puerto, E. Chavez, Y. Pennec, B. Djafari-Rouhani, F. Alzina, A one-dimensional optomechanical crystal with a complete phononic band gap, Nature communications, 5 (2014) 4452.
[175] S.G. Johnson, S. Fan, P.R. Villeneuve, J.D. Joannopoulos, L. Kolodziejski, Guided modes in photonic crystal slabs, Physical Review B, 60 (1999) 5751.
[176] A. Mrabti, G. Lévêque, A. Akjouj, Y. Pennec, B. Djafari-Rouhani, R. Nicolas, T. Maurer, P.-M. Adam, Elastoplasmonic interaction in metal-insulator-metal localized surface plasmon systems, Physical Review B, 94 (2016) 075405.
[177] M.I. Hussein, K. Hamza, G.M. Hulbert, R.A. Scott, K. Saitou, Multiobjective evolutionary optimization of periodic layered materials for desired wave dispersion characteristics, Structural and Multidisciplinary Optimization, 31 (2006) 60-75.
[178] O. Sigmund, J. Søndergaard Jensen, Systematic design of phononic band–gap materials and structures by topology optimization, Philosophical Transactions of the Royal Society of London. Series A: Mathematical, Physical and Engineering Sciences, 361 (2003) 1001-1019.
[179] O.R. Bilal, M.I. Hussein, Ultrawide phononic band gap for combined in-plane and out-of-plane waves, Physical Review E, 84 (2011) 065701.
[180] A. Sukhovich, L. Jing, J.H. Page, Negative refraction and focusing of ultrasound in two-dimensional phononic crystals, Physical Review B, 77 (2008) 014301.
[181] Z. He, Y. Heng, S. Peng, Y. Ding, M. Ke, Z. Liu, Acoustic collimating beams by negative refraction in two-dimensional phononic crystal, Journal of Applied Physics

, 105 (2009) 116105.
[182] Z. He, X. Li, J. Mei, Z. Liu, Improving imaging resolution of a phononic crystal lens by employing acoustic surface waves, Journal of Applied Physics, 106 (2009) 026105.
[183] M. Ke, Z. Liu, C. Qiu, W. Wang, J. Shi, W. Wen, P. Sheng, Negative-refraction imaging with two-dimensional phononic crystals, Physical Review B, 72 (2005) 064306.
[184] J. Pierre, O. Boyko, L. Belliard, J. Vasseur, B. Bonello, Negative refraction of zero order flexural Lamb waves through a two-dimensional phononic crystal, Applied Physics Letters, 97 (2010) 121919.
[185] I.A. Veres, T. Berer, O. Matsuda, P. Burgholzer, Focusing and subwavelength imaging of surface acoustic waves in a solid-air phononic crystal, Journal of Applied Physics, 112 (2012) 053504.
[186] J. Christensen, F.J.G. de Abajo, Anisotropic metamaterials for full control of acoustic waves, Physical review letters, 108 (2012) 124301.
[187] á. Notomi, Theory of light propagation in strongly modulated photonic crystals: Refractionlike behavior in the vicinity of the photonic band gap, Physical Review B, 62 (2000) 10696.
[188] S.-C.S. Lin, T.J. Huang, J.-H. Sun, T.-T. Wu, Gradient-index phononic crystals, Physical Review B, 79 (2009) 094302.
[189] T.-T. Wu, Y.-T. Chen, J.-H. Sun, S.-C.S. Lin, T.J. Huang, Focusing of the lowest antisymmetric Lamb wave in a gradient-index phononic crystal plate, Applied Physics Letters, 98 (2011) 171911.
[190] S.-C.S. Lin, B.R. Tittmann, T.J. Huang, Design of acoustic beam aperture modifier using gradient-index phononic crystals, Journal of applied physics, 111 (2012) 123510.
[191] A. Climente, D. Torrent, J. Sánchez-Dehesa, Sound focusing by gradient index sonic lenses, Applied Physics Letters, 97 (2010) 104103.
[192] T.P. Martin, M. Nicholas, G.J. Orris, L.-W. Cai, D. Torrent, J. Sánchez-Dehesa, Sonic gradient index lens for aqueous applications, Applied Physics Letters, 97 (2010) 113503.
[193] L. Zigoneanu, B.-I. Popa, S.A. Cummer, Design and measurements of a broadband two-dimensional acoustic lens, Physical Review B, 84 (2011) 024305.
[194] Y. Li, B. Liang, X. Tao, X.-f. Zhu, X.-y. Zou, J.-c. Cheng, Acoustic focusing by coiling up space, Applied Physics Letters, 101 (2012) 233508.
[195] T. Chang, G. Dupont, S. Enoch, S. Guenneau, Enhanced control of light and sound trajectories with three-dimensional gradient index lenses, New Journal of Physics, 14 (2012) 035011.

[196] K. Deng, Y. Ding, Z. He, H. Zhao, J. Shi, Z. Liu, Graded negative index lens with designable focal length by phononic crystal, Journal of Physics D: Applied Physics, 42 (2009) 185505.
[197] S. Peng, Z. He, H. Jia, A. Zhang, C. Qiu, M. Ke, Z. Liu, Acoustic far-field focusing effect for two-dimensional graded negative refractive-index sonic crystals, Applied Physics Letters, 96 (2010) 263502.
[198] X. Yan, R. Zhu, G. Huang, F.-G. Yuan, Focusing guided waves using surface bonded elastic metamaterials, Applied Physics Letters, 103 (2013) 121901.
[199] Y. Ye, M. Ke, Y. Li, T. Wang, Z. Liu, Focusing of spoof surface-acoustic-waves by a gradient-index structure, Journal of Applied Physics, 114 (2013) 154504.
[200] B.-g. Yuan, Y. Tian, Y. Cheng, X.-j. Liu, An acoustic Maxwell's fish-eye lens based on gradient-index metamaterials, Chinese Physics B, 25 (2016) 104301.
[201] H. Kurt, D.S. Citrin, Graded index photonic crystals, Optics express, 15 (2007) 1240-1253.
[202] H. Gao, B. Zhang, S.G. Johnson, G. Barbastathis, Design of thin–film photonic metamaterial Lüneburg lens using analytical approach, Optics express, 20 (2012) 1617-1628.
[203] K.-V. Do, X. Le Roux, D. Marris-Morini, L. Vivien, E. Cassan, Experimental demonstration of light bending at optical frequencies using a non-homogenizable graded photonic crystal, Optics Express, 20 (2012) 4776-4783.
[204] A. Climente, D. Torrent, J. Sánchez-Dehesa, Gradient index lenses for flexural waves based on thickness variations, Applied Physics Letters, 105 (2014) 064101.
[205] C. Ma, M.A. Escobar, Z. Liu, Extraordinary light focusing and Fourier transform properties of gradient-index metalenses, Physical Review B, 84 (2011) 195142.
[206] D. Torrent, Y. Pennec, B. Djafari-Rouhani, Effective medium theory for elastic metamaterials in thin elastic plates, Physical Review B, 90 (2014) 104110.
[207] D. Lu, Z. Liu, Hyperlenses and metalenses for far-field super-resolution imaging, Nature communications, 3 (2012) 1205.
[208] J. Li, L. Fok, X. Yin, G. Bartal, X. Zhang, Experimental demonstration of an acoustic magnifying hyperlens, Nature materials, 8 (2009) 931.
[209] J. Zhu, J. Christensen, J. Jung, L. Martin-Moreno, X. Yin, L. Fok, X. Zhang, F. Garcia-Vidal, A holey-structured metamaterial for acoustic deep-subwavelength imaging, Nature physics, 7 (2011) 52.
[210] F. Lemoult, N. Kaina, M. Fink, G. Lerosey, Wave propagation control at the deep subwavelength scale in metamaterials, Nature Physics, 9 (2013) 55.
[211] S. Yao, X. Zhou, G. Hu, Investigation of the negative-mass behaviors occurring below a cut-off frequency, New Journal of Physics, 12 (2010) 103025.
[212] R. Zhu, X. Liu, G. Huang, H.-H. Huang, C. Sun, Microstructural design and experimental validation of elastic metamaterial plates with anisotropic mass density, Physical Review B, 86 (2012) 144307.
[213] E. Centeno, D. Cassagne, J.-P. Albert, Mirage and superbending effect in two-dimensional graded photonic crystals, Physical Review B, 73 (2006) 235119.
[214] E. Cassan, K.-V. Do, C. Caer, D. Marris-Morini, L. Vivien, Short-wavelength light propagation in graded photonic crystals, Journal of Lightwave Technology, 29 (2011) 1937-1943.
[215] P. Halevi, A. Krokhin, J. Arriaga, Photonic crystal optics and homogenization of 2D periodic composites, Physical review letters, 82 (1999) 719.
[216] J. Zhao, B. Bonello, R. Marchal, O. Boyko, Beam path and focusing of flexural Lamb waves within phononic crystal-based acoustic lenses, New Journal of Physics, 16 (2014) 063031.
[217] C. Luo, S.G. Johnson, J. Joannopoulos, J. Pendry, Subwavelength imaging in photonic crystals, Physical Review B, 68 (2003) 045115.
[218] W. Wang, B. Bonello, B. Djafari-Rouhani, Y. Pennec, J. Zhao, Double-Negative Pillared Elastic Metamaterial, Physical Review Applied, 10 (2018) 064011.
[219] Y. Jin, Design of acoustic artificial structured materials: piezoelectric superlattice, gradient index lens, pillar based phononic crystal plate, Lille 1, 2017.
[220] D. Torrent, Acoustic anomalous reflectors based on diffraction grating engineering, Physical Review B, 98 (2018) 060101.
[221] P. Packo, A.N. Norris, D. Torrent, Inverse Grating Problem: Efficient Design of Anomalous Flexural Wave Reflectors and Refractors, Physical Review Applied, 11 (2019) 014023.

[222] Y. Xiao, J. Wen, X. Wen, Flexural wave band gaps in locally resonant thin plates with periodically attached spring–mass resonators, Journal of Physics D: Applied Physics, 45 (2012) 195401.
[223] X. Zhang, M. Xiao, Y. Cheng, M.-H. Lu, J. Christensen, Topological sound, Communications Physics, 1 (2018) 97.
[224] G. Ma, M. Xiao, C. Chan, Topological phases in acoustic and mechanical systems, Nature Reviews Physics, DOI (2019) 1.
[225] W. Wang, Y. Jin, W. Wang, B. Bonello, B. Djafari-Rouhani, R. Fleury, Robust Fano resonance in a topological mechanical beam, Physical Review B, 101 (2020) 024101.
[226] R. Chaunsali, C.-W. Chen, J. Yang, Experimental demonstration of topological waveguiding in elastic plates with local resonators, New Journal of Physics, 20 (2018) 113036.
[227] S.H. Mousavi, A.B. Khanikaev, Z. Wang, Topologically protected elastic waves in phononic metamaterials, Nature communications, 6 (2015) 8682.
[228] M. Miniaci, R. Pal, B. Morvan, M. Ruzzene, Experimental observation of topologically protected helical edge modes in patterned elastic plates, Physical Review X, 8 (2018) 031074.
[229] C.-W. Chen, N. Lera, R. Chaunsali, D. Torrent, J.V. Alvarez, J. Yang, P. San-Jose, J. Christensen, Mechanical analogue of a Majorana bound state, arXiv preprint arXiv:1905.03510, DOI (2019).
[230] C.W. Chen, N. Lera, R. Chaunsali, D. Torrent, J.V. Alvarez, J. Yang, P. San-Jose, J. Christensen, Mechanical analogue of a Majorana bound state, Advanced Materials, 31 (2019) 1904386.
[231] W. Wang, B. Bonello, B. Djafari-Rouhani, Y. Pennec, Topological valley, pseudospin, and pseudospin-valley protected edge states in symmetric pillared phononic crystals, Physical Review B, 100 (2019) 140101.
[232] W. Wang, B. Bonello, B. Djafari-Rouhani, Y. Pennec, Polarization-dependent and valley-protected Lamb waves in asymmetric pillared phononic crystals, Journal of Physics D: Applied Physics, 52 (2019) 505302.
[233] H. Fan, B. Xia, L. Tong, S. Zheng, D. Yu, Elastic Higher-Order Topological Insulator with Topologically Protected Corner States, Physical review letters, 122 (2019) 204301.
[234] D.G. Cahill, P.V. Braun, G. Chen, D.R. Clarke, S. Fan, K.E. Goodson, P. Keblinski, W.P. King, G.D. Mahan, A. Majumdar, H.J. Maris, S.R. Phillpot, E. Pop, L. Shi, Nanoscale thermal transport. II. 2003–2012, Applied Physics Reviews, 1 (2014) 011305.
[235] A.N. Cleland, D.R. Schmidt, C.S. Yung, Thermal conductance of nanostructured phononic crystals, Physical Review B, 64 (2001) 172301.
[236] A.J.H. McGaughey, M.I. Hussein, E.S. Landry, M. Kaviany, G.M. Hulbert, Phonon band structure and thermal transport correlation in a layered diatomic crystal, Physical Review B, 74 (2006) 104304.
[237] J. Tang, H.-T. Wang, D.H. Lee, M. Fardy, Z. Huo, T.P. Russell, P. Yang, Holey Silicon as an Efficient Thermoelectric Material, Nano Letters, 10 (2010) 4279-4283.
[238] J.-K. Yu, S. Mitrovic, D. Tham, J. Varghese, J.R. Heath, Reduction of thermal conductivity in phononic nanomesh structures, Nature Nanotechnology, 5 (2010) 718.
[239] Y. He, D. Donadio, J.-H. Lee, J.C. Grossman, G. Galli, Thermal Transport in Nanoporous Silicon: Interplay between Disorder at Mesoscopic and Atomic Scales, ACS Nano, 5 (2011) 1839-1844.
[240] S. Alaie, D.F. Goettler, M. Su, Z.C. Leseman, C.M. Reinke, I. El-Kady, Thermal transport in phononic crystals and the observation of coherent phonon scattering at room temperature, Nature Communications, 6 (2015) 7228.
[241] J.-N. Gillet, Y. Chalopin, S. Volz, Atomic-Scale Three-Dimensional Phononic Crystals With a Very Low Thermal Conductivity to Design Crystalline Thermoelectric Devices, Journal of Heat Transfer, 131 (2009) 043206-043206-043210.
[242] B.L. Davis, M.I. Hussein, Thermal characterization of nanoscale phononic crystals using supercell lattice dynamics, AIP Advances, 1 (2011) 041701.
[243] L. Yang, N. Yang, B. Li, Extreme Low Thermal Conductivity in Nanoscale 3D Si Phononic Crystal with Spherical Pores, Nano Letters, 14 (2014) 1734-1738.
[244] N.W. Ashcroft, N.D. Mermin, Solid State Physics, Holt, Rinehart and Winston1976.

[245] G.P. Srivastava, The Physics of Phonons, Taylor & Francis1990.
[246] A. Jain, Y.-J. Yu, A.J.H. McGaughey, Phonon transport in periodic silicon nanoporous films with feature sizes greater than 100 nm, Physical Review B, 87 (2013) 195301.
[247] M.R. Wagner, B. Graczykowski, J.S. Reparaz, A. El Sachat, M. Sledzinska, F. Alzina, C.M. Sotomayor Torres, Two-Dimensional Phononic Crystals: Disorder Matters, Nano Letters, 16 (2016) 5661-5668.
[248] C.J. Vineis, A. Shakouri, A. Majumdar, M.G. Kanatzidis, Nanostructured Thermoelectrics: Big Efficiency Gains from Small Features, Advanced Materials, 22 (2010) 3970-3980.
[249] G. Chen, M.S. Dresselhaus, G. Dresselhaus, J.P. Fleurial, T. Caillat, Recent developments in thermoelectric materials International Materials Reviews, 48 (2003) 45-66.
[250] D.M. Rowe, Thermoelectrics Handbook: Macro to Nano, CRC Press2018.
[251] M.I. Hussein, C.N. Tsai, H. Honarvar, Thermal Conductivity Reduction in a Nanophononic Metamaterial versus a Nanophononic Crystal: A Review and Comparative Analysis, Advanced Functional Materials, DOI (2019) 1906718.
[252] J.B. Pendry, A.J. Holden, D.J. Robbins, W.J. Stewart, Magnetism from conductors and enhanced nonlinear phenomena, IEEE Transactions on Microwave Theory and Techniques, 47 (1999) 2075-2084.
[253] D.R. Smith, W.J. Padilla, D.C. Vier, S.C. Nemat-Nasser, S. Schultz, Composite Medium with Simultaneously Negative Permeability and Permittivity, Physical Review Letters, 84 (2000) 4184-4187.
[254] Z. Liu, C.T. Chan, P. Sheng, Three-component elastic wave band-gap material, Physical Review B, 65 (2002) 165116.
[255] A.I. Boukai, Y. Bunimovich, J. Tahir-Kheli, J.-K. Yu, W.A. Goddard Iii, J.R. Heath, Silicon nanowires as efficient thermoelectric materials, Nature, 451 (2008) 168.
[256] S. Neogi, J.S. Reparaz, L.F.C. Pereira, B. Graczykowski, M.R. Wagner, M. Sledzinska, A. Shchepetov, M. Prunnila, J. Ahopelto, C.M. Sotomayor-Torres, D. Donadio, Tuning Thermal Transport in Ultrathin Silicon Membranes by Surface Nanoscale Engineering, ACS Nano, 9 (2015) 3820-3828.
[257] M.S. Dresselhaus, G. Chen, M.Y. Tang, R.G. Yang, H. Lee, D.Z. Wang, Z.F. Ren, J.-P. Fleurial, P. Gogna, New Directions for Low-Dimensional Thermoelectric Materials, Advanced Materials, 19 (2007) 1043-1053.
[258] Z. Wei, J. Yang, K. Bi, Y. Chen, Phonon transport properties in pillared silicon film, Journal of Applied Physics, 118 (2015) 155103.
[259] S. Xiong, K. Sääskilahti, Y.A. Kosevich, H. Han, D. Donadio, S. Volz, Blocking phonon transport by structural resonances in alloy-based nanophononic metamaterials leads to ultralow thermal conductivity, Physical review letters, 117 (2016) 025503.
[260] D. Ma, A. Arora, S. Deng, G. Xie, J. Shiomi, N. Yang, Quantifying phonon particle and wave transport in silicon nanophononic metamaterial with cross junction, Materials Today Physics, 8 (2019) 56-61.
[261] D. Ma, H. Ding, H. Meng, L. Feng, Y. Wu, J. Shiomi, N. Yang, Nano-cross-junction effect on phonon transport in silicon nanowire cages, Physical Review B, 94 (2016) 165434.
[262] T. Zhu, K. Swaminathan-Gopalan, K.J. Cruse, K. Stephani, E. Ertekin, Vibrational Energy Transport in Hybrid Ordered/Disordered Nanocomposites: Hybridization and Avoided Crossings of Localized and Delocalized Modes, Advanced Functional Materials, 28 (2018) 1706268.
[263] M.I. Hussein, Phononic metamaterials comprising atomically disordered resonators, Google Patents, 2017.
[264] Y.-Y. Liu, Y.-J. Zeng, P.-Z. Jia, X.-H. Cao, X.-w. Jiang, K.-Q. Chen, An efficient mechanism for enhancing the thermoelectricity of nanoribbons by blocking phonon transport in 2D materials, Journal of Physics: Condensed Matter, 30 (2018) 275701.
[265] A. Giri, P.E. Hopkins, Giant reduction and tunability of the thermal conductivity of carbon nanotubes through low-frequency resonant modes, Physical Review B, 98 (2018) 045421.
[266] D. Ma, X. Wan, N. Yang, Unexpected thermal conductivity enhancement in pillared graphene nanoribbon with isotopic resonance, Physical Review B, 98 (2018) 245420.

[267] A. Giri, P.E. Hopkins, Resonant phonon modes in fullerene functionalized graphene lead to large tunability of thermal conductivity without impacting the mechanical properties, Journal of Applied Physics, 125 (2019) 205102.
[268] A. Iskandar, A. Gwiazda, Y. Huang, M. Kazan, A. Bruyant, M. Tabbal, G. Lerondel, Modification of the phonon spectrum of bulk Si through surface nanostructuring, Journal of Applied Physics, 120 (2016) 095106.
[269] Y.-Y. Liu, W.-X. Zhou, L.-M. Tang, K.-Q. Chen, An important mechanism for thermal rectification in graded nanowires, Applied Physics Letters, 105 (2014) 203111.
[270] Y.-Y. Liu, W.-X. Zhou, K.-Q. Chen, Conjunction of standing wave and resonance in asymmetric nanowires: a mechanism for thermal rectification and remote energy accumulation, Scientific Reports, 5 (2015) 17525.
[271] X. Yang, D. Yu, B. Cao, A.C. To, Ultrahigh Thermal Rectification in Pillared Graphene Structure with Carbon Nanotube–Graphene Intramolecular Junctions, ACS Applied Materials & Interfaces, 9 (2017) 29-35.
[272] X.-K. Chen, J. Liu, Z.-X. Xie, Y. Zhang, Y.-X. Deng, K.-Q. Chen, A local resonance mechanism for thermal rectification in pristine/branched graphene nanoribbon junctions, Applied Physics Letters, 113 (2018) 121906.
[273] B. Li, K.T. Tan, J. Christensen, Tailoring the thermal conductivity in nanophononic metamaterials, Physical Review B, 95 (2017) 144305.
[274] M. Nomura, Phonon and heat transport control using pillar-based phononic crystals AU - Anufriev, Roman, Science and Technology of Advanced Materials, 19 (2018) 863-870.
[275] B. Li, K.T. Tan, J. Christensen, Heat conduction tuning by hyperbranched nanophononic metamaterials, Journal of Applied Physics, 123 (2018) 205105.
[276] F.H. Stillinger, T.A. Weber, Computer simulation of local order in condensed phases of silicon, Physical Review B, 31 (1985) 5262-5271.
[277] I. Hussein Mahmoud, Reduced Bloch mode expansion for periodic media band structure calculations, Proceedings of the Royal Society A: Mathematical, Physical and Engineering Sciences, 465 (2009) 2825-2848.
[278] L.R. Rabiner, B. Gold, Theory and application of digital signal processing, Englewood Cliffs, NJ, Prentice-Hall, Inc., 1975. 777 p., DOI (1975).
[279] J.A. Thomas, J.E. Turney, R.M. Iutzi, C.H. Amon, A.J.H. McGaughey, Predicting phonon dispersion relations and lifetimes from the spectral energy density, Physical Review B, 81 (2010) 081411.
[280] A. McGaughey, J.M. Larkin, Predicting phonon properties from equilibrium molecular dynamics simulations, Ann. Rev. Heat Transfer, 17 (2014) 49-87.
[281] T. Wang, G. Madsen, A. Hartmaier, Atomistic study of the influence of lattice defects on the thermal conductivity of silicon, Modelling and Simulation in Materials Science and Engineering, 22 (2014) 035011.
[282] J. Larkin, J. Turney, A. Massicotte, C. Amon, A. McGaughey, Comparison and evaluation of spectral energy methods for predicting phonon properties, Journal of Computational and Theoretical Nanoscience, 11 (2014) 249-256.
[283] T. Feng, B. Qiu, X. Ruan, Anharmonicity and necessity of phonon eigenvectors in the phonon normal mode analysis, Journal of Applied Physics, 117 (2015) 195102.
[284] E. Helfand, Transport Coefficients from Dissipation in a Canonical Ensemble, Physical Review, 119 (1960) 1-9.
[285] R. Zwanzig, Time-correlation functions and transport coefficients in statistical mechanics, Annual Review of Physical Chemistry, 16 (1965) 67-102.
[286] A.J. Ladd, B. Moran, W.G. Hoover, Lattice thermal conductivity: A comparison of molecular dynamics and anharmonic lattice dynamics, Physical Review B, 34 (1986) 5058.
[287] S. Plimpton, Fast parallel algorithms for short-range molecular dynamics, Journal of computational physics, 117 (1995) 1-19.
[288] K. Esfarjani, G. Chen, H.T. Stokes, Heat transport in silicon from first-principles calculations, Physical Review B, 84 (2011) 085204.

[289] X. Yong, W. Jihong, W. Xisen, Flexural wave band gaps in locally resonant thin plates with periodically attached spring–mass resonators, Journal of Physics D: Applied Physics, 45 (2012) 195401.
[290] X. Lin, Y. Rivenson, N.T. Yardimci, M. Veli, Y. Luo, M. Jarrahi, A. Ozcan, All-optical machine learning using diffractive deep neural networks, Science, 361 (2018) 1004-1008.
[291] J.H. Han, K.M. Bae, S.K. Hong, H. Park, J.-H. Kwak, H.S. Wang, D.J. Joe, J.H. Park, Y.H. Jung, S. Hur, C.D. Yoo, K.J. Lee, Machine learning-based self-powered acoustic sensor for speaker recognition, Nano Energy, 53 (2018) 658-665.
[292] Z.S. Ballard, D. Shir, A. Bhardwaj, S. Bazargan, S. Sathianathan, A. Ozcan, Computational Sensing Using Low-Cost and Mobile Plasmonic Readers Designed by Machine Learning, ACS Nano, 11 (2017) 2266-2274.
[293] I. Malkiel, M. Mrejen, A. Nagler, U. Arieli, L. Wolf, H. Suchowski, Plasmonic nanostructure design and characterization via Deep Learning, Light: Science & Applications, 7 (2018) 60.
[294] W. Ma, F. Cheng, Y. Liu, Deep-Learning-Enabled On-Demand Design of Chiral Metamaterials, ACS Nano, 12 (2018) 6326-6334.
[295] Y. Pennec, Y. Jin, B. Djafari-Rouhani, Phononic and photonic crystal for sensing application, Advances in Applied Mechanics, 52 (2019) 105-145.